2020

IMPACTS OF SHOALING OCEAN SURFACE WAVES ON WIND STRESS AND STORM SURGE

Xuanyu Chen
University of Rhode Island, xychen@uri.edu

IMPACTS OF SHOALING OCEAN SURFACE WAVES ON WIND STRESS AND STORM SURGE

BY

XUANYU CHEN

A DISSERTATION SUBMITTED IN PARTIAL FULFILLMENT OF THE REQUIREMENTS FOR THE DEGREE OF

DOCTOR OF PHILOSOPHY

IN

OCEANOGRAPHY

UNIVERSITY OF RHODE ISLAND

2020

DOCTOR OF PHILOSOPHY DISSERTATION

OF

XUANYU CHEN

APPROVED:

Dissertation Committee:

Major Professor Isaac Ginis

Major Professor Tetsu Hara

David S. Ullman

M. Reza Hashemi

Brenton DeBoef
DEAN OF THE GRADUATE SCHOOL

UNIVERSITY OF RHODE ISLAND

2020

ABSTRACT

Ocean surface waves have been known to affect the wind stress, or air-sea momentum flux, in the open ocean under tropical cyclones. As a tropical cyclone (TC) makes landfall, the surface waves shoal as they enter the shallower coastal waters ($< 30\sim50$ m). The impacts of these shoaling surface waves on the wind stress have not yet been thoroughly investigated, but they have been postulated to be important for storm surge prediction. In this study, the WAVEWATCH III (WW3) model is used to simulate the depth modifications on the surface wave fields and the wind stress. Two wave-spectrum based wind stress estimation modules in the WW3 model are used to quantify the impact of wave shoaling on wind stress and drag coefficient under steady uniform wind and tropical cyclone conditions. The consequence of using the shoaling wave modified wind stress for modeling storm surge is investigated using the Advanced Circulation (ADCIRC) model.

For the shoaling wave simulations, an accurate wave field generated by tropical cyclones in the open ocean needs to be established first. The sensitivity of tropical cyclone wave simulations in the open ocean to different spatial resolutions ($1/3^\circ$, $1/6^\circ$, $1/12^\circ$ and $1/24^\circ$) is evaluated using two wave models, WW3 and Simulating WAves Nearshore. Results from both models show that the coarsest resolution ($1/3^\circ$) introduces significant errors in both the significant wave height (Hs) and the mean wavelength. Moreover, results reveal that sensitivity to spatial resolution strongly depends on storm characteristics. Waves simulated under the small and fast moving TC show the largest sensitivity to the coarse spatial resolutions. With the $1/3^\circ$ resolution, maximum Hs can be underestimated by as much as 6% in WW3 and 16% in SWAN compared to those with the $1/24^\circ$ resolution.

The impacts of shoaling ocean surface waves on the wind stress and drag coefficient (C_d) in coastal waters are investigated with the WW3 under steady, uniform onshore wind and tropical cyclones. Our results show that under uniform onshore winds, as

water depth decreases, the drag coefficient increases gradually to a peak value and then rapidly reduces compared to the deep-water value. The maximum C_d occurs roughly where depth-induced wave breaking starts. The magnitude of C_d enhancement is more significant on a steeper slope and can reach 40%, which is mainly due to the steepening of waves and reduction of the wave phase speed during the shoaling. Our results suggest significantly larger variability of C_d at a given wind speed in finite depth waters than in deep water, which is also found during idealized landfalling TCs. Specifically, C_d is enhanced in the right TC quadrants (due to shoaling fetch-dependent waves) and in the left TC quadrants (due to shoaling opposing-wind swells) compared to its deep-water value. However, C_d is reduced in the front/rear quadrants due to weaker wind seas. The misalignment between wind stress and wind speed directions is also enhanced in shallow water. In general, the shoaling wave effects on the wind stress and C_d are much stronger on steeper bottom slopes and in faster-moving storms.

At last, the shoaling wave modified wind stress is applied to a two-dimensional steady-state model and the ADCIRC model to investigate its impacts on storm surge. In the steady onshore wind conditions, the shoaling wave modified (or sea-state dependent (SSD)) wind stress can increase the sea surface elevation by as much as 15% on a steep bottom slope compared to the result using the bulk wind stress as a function of wind speed. In TC conditions, the maximum impact of the SSD wind stress occurs to the left of the storm track near the radius of maximum wind around the time of TC landfall. The set-down of the sea level is significantly enhanced due to increased offshore wind stress. However, the SSD wind stress impact on the peak surge to the right of the storm track is negligible. Hence, our analysis suggests that the SSD wind stress has the biggest impact in uniform onshore wind conditions (such as under large, slow moving extratropical cyclones) than in TC conditions. Our results also suggest that the water level prediction at the shoreline is sensitive to the wind stress in the surf zone, which is not resolved explicitly in our model.

ACKNOWLEDGEMENTS

I am deeply indebted to the persistent time investment, guidance, and encouragement from my major advisor Dr. Isaac Ginis and co-advisor Dr. Tetsu Hara throughout my doctoral study. They challenged me to think critically and to conduct reliable research through diligent work. I thank my committee member, Dr. David Ullman, for his help in setting up and running the storm surge model and understanding the storm surge process. Additionally, I want to thank him for his reassurance that research is never a straight path. I also thank my committee member, Dr. M. Reza Hashemi, for answering my questions and for providing information relevant to my study.

This dissertation could not have been accomplished without the solid foundation laid by Dr. Brandon G. Reichl (NOAA Geophysical Fluid Dynamics Laboratory). Correspondence and discussions with Dr. Alexander Babanin (University of Melbourne) and Dr. Qingxiang Liu (University of Melbourne) have also been conducive.

Completion of my doctoral study is also impossible without the empowering and emotional support from a variety of people inside and outside the Graduate School of Oceanography. Here, I want to express my gratitude specifically to Dr. Penny Rothstein and Dr. Rebecca Robinson. They have served as my lights during the darkest moment in the journey.

At last, I acknowledge funding from the Department of Homeland Security and the GSO Alumni awards that made a lot of opportunities possible.

DEDICATION

This dissertation is dedicated to my grandparents and parents for their unwavering faith in the value of education, their striving for improvement, and the sacrifices they have made for me.

PREFACE

This dissertation is written in manuscript format and consists of four scientific journal articles. The first manuscript was published in *Journal of Marine Science and Engineering*. The second and third manuscripts were published in *Journal of Geophysical Research: Oceans*. The fourth manuscript is prepared for submission to *Journal of Coastal Research*.

TABLE OF CONTENTS

LIST OF TABLES

LIST OF FIGURES

MANUSCRIPT 1

Sensitivity of Offshore Tropical Cyclone Wave Simulations to Spatial Resolution in Wave Models

Xuanyu Chen[1*], Isaac Ginis[1], and Tetsu Hara[1]

Published in Journal of Marine Science and Engineering, October 2018

[1]Graduate School of Oceanography, University of Rhode Island, Narragansett, Rhode Island

[*]Corresponding author email: xychen@my.uri.edu

Abstract

This study investigated and quantified the sensitivity of tropical cyclone (TC) wave simulations in the open ocean to different spatial resolutions ($1/3^\circ$, $1/6^\circ$, $1/12^\circ$ and $1/24^\circ$) using two wave models, WAVEWATCH III (WW3) and Simulating WAves Nearshore (SWAN). Six idealized TCs of different radii of maximum winds (25 km and 50 km), and of different translation speeds (3 m/s, 6 m/s and 9 m/s) were prescribed to force these two wave models. Results from both models show that the coarsest resolution ($1/3^\circ$) introduces significant errors in both the significant wave height (SWH) and the mean wavelength. Moreover, results reveal that sensitivity to spatial resolution strongly depends on storm characteristics. Waves simulated under the small (25 km) and fast moving (9 m/s) TC show the largest sensitivity to the coarse spatial resolutions. With the $1/3^\circ$ resolution, maximum SWH can be underestimated by as much as 6% in WW3 and 16% in SWAN compared to those with the $1/24^\circ$ resolution. These findings from the idealized TC simulations are further confirmed by wave simulations under a historical storm. Our analysis also demonstrates that spatial smoothing of the input wind field with coarse grids is not the only reason for the errors in wave simulations.

1.1 Introduction

Surface gravity waves under extreme conditions such as tropical cyclones (TCs) have been of practical and scientific interest for over a half century, since the pioneering paper by *Barber and Ursell* (1948). For engineers and weather forecasters, it is essential to accurately predict the height of extreme waves for safety of seafaring navigation, design and protection of marine structures and public safety. For scientists, these extreme TC waves are important because they may impact the coupled ocean–atmosphere system by modifying the air–sea fluxes and near surface turbulent processes.

Recent studies have shown that including surface wave effects in storm surge modeling is important because waves exchange momentum with ocean currents via the radiation stress (*Longuet-Higgins and Stewart*, 1964; *Dietrich et al.*, 2011; *Sun et al.*, 2013; *Feng et al.*, 2016). For example, a coupled storm surge-wave model system was developed by *Dietrich et al.* (2011), in which the radiation stress is computed by the SWAN model and is passed to the ADvanced CIRCulation (ADCIRC) model. In addition, recent studies suggest that wind stress (or drag coefficient), which forces the storm surge model, may be strongly dependent on sea-states, and that accurate estimation of wind stress requires incorporating wave spectra from third generation wave models (*Donelan et al.*, 2012; *Reichl et al.*, 2014).

In the state-of-the-art coupled storm surge-wave models (ADCIRC-SWAN (*Bunya et al.*, 2010; *Dietrich et al.*, 2010, 2011) and FVCOM-SWAVE (*Sun et al.*, 2013)), both wave and storm surge simulations are performed on a common unstructured grid, where the spatial resolution is high in the nearshore region but it rapidly decreases toward the open ocean for computation efficiency. For example, in the ADCIRC-SWAN operational storm surge modeling system (*Fleming et al.*, 2008; *Dresback et al.*, 2013), simulations are conducted using a resolution coarser than 33 km in the open ocean (Figure 1.1). While such a resolution is likely sufficient for storm surge prediction, it is unclear whether it is sufficient for accurate wave simulations under complex TC wind fields.

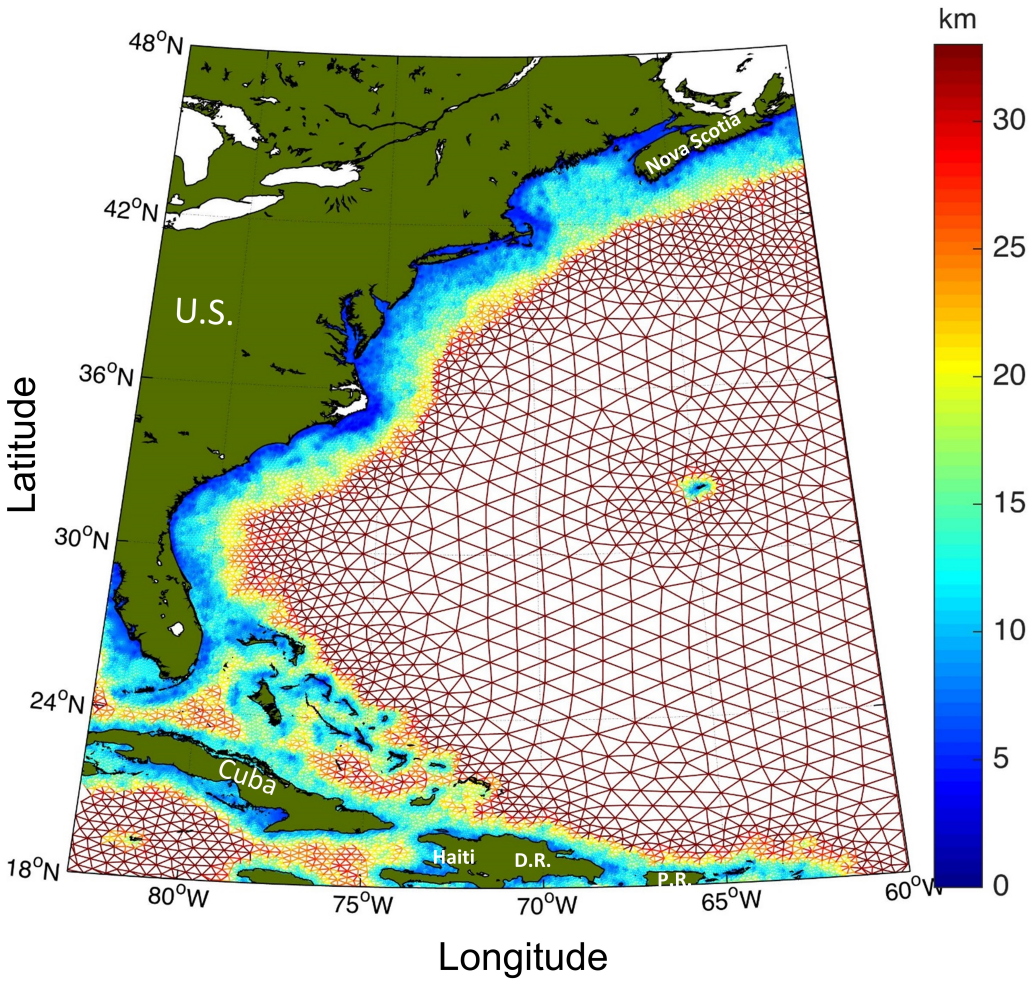

Figure 1.1: Spatial resolution of an unstructured grid in western North Atlantic region used in ADCIRC Surge Guidance System (ASGS).

There have been few studies directly addressing the wave model performance with different spatial resolutions. *Kerr et al.* (2013) investigated the coupled ADCIRC-SWAN model sensitivity to the mesh resolution, topographical details and other factors during Hurricane Ike (2008). By comparing the SWAN wave simulations generated with two meshes of different resolutions against observational data, they concluded that, in the open Gulf, a moderate resolution (10-30 km) wave model can produce accurate wave characteristics. However, this conclusion was based on only one case study of a relatively large-size hurricane.

Xu et al. (2017) modeled tropical cyclone waves under three typhoons in South China

Sea using WW3 and compared simulated wave characteristics to buoy observations. They discussed sensitivity to spatial resolution in a three nested-mesh configuration ($1/4^\circ$, $1/8^\circ$ and $1/12^\circ$) and reported that the grid resolution was not critical if the resolution of wind forcing remained coarse. However, they did not perform quantitative evaluation of the model sensitivity to spatial resolution.

Currently, wave simulations in open ocean are carried out with a wide range of spatial resolutions for different applications. The European Centre for Medium-Range Weather Forecasts (ECMWF) operates the High RESolution WAve Model (HRES-WAM) on a $1/8^\circ$ resolution grid (*Haiden et al.* (2016)). The NOAA Hurricane Wave Model uses a $1/10^\circ$ resolution (personal communication with Dr. Jessica Meixner). However, some operational and research wave models use coarser resolutions. For example, the NOAA operational global wave forecasts using the WW3 model, are carried out with $1/2^\circ$–$1/6^\circ$ resolutions in most regions (Figure 1 in *Chawla et al.* (2013)). In a recent global climate study of TC-generated extreme waves based on CMIP5 multi-model ensemble (*Shimura et al.* (2017)), the WW3 model is used with a resolution of 60 km. *Tolman and Alves* (2005) developed a continuously moving grid version of the WW3 model to resolve TC wave conditions at high spatial resolution. This version of WW3 is designed only for offshore TC waves and has not been widely used in academic research and practical applications.

There is no doubt that higher spatial resolution produces more accurate TC wave simulations. However, for computational efficiency, TC wave modeling is still often performed on relatively coarse grid systems. To choose an optimal spatial resolution based on an acceptable error threshold for a given application, it is desirable to conduct a thorough quantitative evaluation of the wave model errors associated with various spatial resolutions in offshore TC wave simulations. Such information is valuable not only for coupled storm surge-wave modeling but also for other applications, such as global weather and climate models coupled with surface wave models.

In this study, we quantified for the first time the sensitivity of offshore TC wave

simulations to spatial resolution by conducting systematic experiments under six idealized TCs with different characteristics, including storm size and translation speed. All experiments were performed separately with two widely used wave models, WW3 and SWAN. To complement the idealized experiments, a historical hurricane case was used to examine the effect of spatial resolution on wave simulations.

In this study, we did not attempt to validate the TC wave simulations against observations. This is because wave model results under TCs strongly depend on the parameterizations of the forcing terms (the wind forcing and the whitecap dissipation, in particular) in the wave models, as demonstrated by *Liu et al.* (2017). Here, we focus on investigating model sensitivity to different spatial resolutions, with one fixed (standard) setting of forcing parameterizations in each wave model.

1.2 Methods

1.2.1 Wave Models

Two widely used third-generation wave models, WAVEWATCH III (version 5.16) (*The WAVEWATCH III® Development Group*, 2016) and SWAN (version 41.01) (*The SWAN team*, ver41.10), were utilized for this study. Both models solve the wave action equations, but WW3 solves for a directional wavenumber spectrum with an explicit numerical scheme, while SWAN solves for a directional frequency spectrum with an implicit numerical scheme Originally, WW3 was developed for simulating waves in the open ocean, while SWAN was optimized for simulating waves in coastal waters with more advanced shallow water physics. However, shallow water physics similar to that in SWAN has been introduced into WW3 since its version 4.18.

In both models, frequency is discretized into 40 bins, ranging from 0.0285 to 1.1726 Hz with a logarithmic increment factor of 1.1, while direction is discretized into 24 equally-spaced bins, following *Fan et al.* (2009) and *Reichl et al.* (2014). In WW3, the wind input term together with the whitecapping dissipation term developed by *Ardhuin et al.* (2010) (referred to as ST4 hereafter) is used. In ST4, the steepness-induced wave breaking

(whitecapping) parameterization is saturation-based and includes the effect of cumulative breaking, independent of any prescribed spectral shape. The wind input parameterization in ST4 takes the positive part of parameterization in *Janssen* (2004). The wind input at high frequency and high winds is reduced, resulting in reduction of the drag coefficient at high winds. The nonlinear interaction term is computed with the standard discrete interaction approximation (DIA). In SWAN, the wind input term and the whitecapping dissipation term are based on *Komen et al.* (1984) formulation, improved by *Rogers et al.* (2003) (referred to as ST1 hereafter). The dissipation parameterization in ST1 is based on the pulse-based model of *Hasselmann* (1974), which is fundamentally different from that used in ST4 of WW3. For the computation of wind input term, the drag coefficient formula from *Wu* (1982) is used and it is capped at 0.0020 (*Huang et al.*, 2013; *Akbar et al.*, 2017). The DIA method is used to approximate the nonlinear interaction term. Details about settings of parameters associated with each source term are listed in Table 1.1. The setup of both models are commonly used (*Dietrich et al.*, 2011, 2010; *Liu et al.*, 2017; *Huang et al.*, 2013).

1.2.2 Specification of Winds in Idealized Hurricanes

1.2.2.a Idealized TC Wind Fields

The idealized TC wind fields are specified based on the parametric wind model of *Holland* (1980). The tangential wind speed V is computed as a gradient wind outside the radius of maximum wind (R_{max}) and as a cyclostrophic winds inside R_{max},

$$V(r) = \begin{cases} \left(\frac{AB(P_n - P_c)}{\rho r^B} e^{-A/r^B} \right)^{1/2} & 0 \le r \le R_{max} \\ \left(\frac{AB(P_n - P_c)}{\rho r^B} e^{-A/r^B} + \frac{r^2 f^2}{4} \right)^{1/2} - \frac{rf}{2} & r > R_{max} \end{cases} \tag{1.1}$$

with,

$$B = \frac{\rho e V_{max}^2}{P_n - P_c} \tag{1.2}$$

$$A = R_{max}^B.$$

Here, r is radial distance from the storm center. The basic TC parameters involved are maximum wind speed (V_{max}), radius of maximum wind (R_{max}), central pressure (P_c, in pascal), environmental pressure (P_n, in pascal) and two constant coefficients A and B, as well as air density ρ (assumed constant at 1.15 kg/m^3) and the Coriolis parameter f. For the idealized TC winds, the value of B is set to 2.0.

For idealized TCs, we prescribed three translation speeds (3 m/s, 6 m/s and 9 m/s) and two radii of maximum wind (25 km and 50 km). The maximum wind speed for all six idealized TCs is set to 50 m/s. In Table 1.2, these idealized storm parameters are compared with the storm parameters of a historical storm, known as the 1938 New England Hurricane (referred to as Hurricane 1938 hereafter), from 18 September to 22 September (landfall).

Table 1.1: Numerical and physical settings used in WW3 and SWAN.

Model Settings		**WW3**	**SWAN**
Numerics	Time Step*	4 fractional time steps	1 global time step
	Propagation Scheme	Third-order Ultimate Quickest (UQ) scheme	First Order, backward space, backward time (BSBT) scheme
Physics	$S_{in} + S_{wc}$	ST4 (Ardhuin et al.)	ST1 (Komen)
		$z_{0_{max}} = 1.002$, $\beta_{max} = 1.43$	$C_{d_{max}} = 0.002$
	S_{nl}	DIA (as default)	

* details on specific time step value are listed in Table 1.3.

Table 1.2: Characteristics of idealized storms and Hurricane 1938 between 18 September and 22 September.

TC Parameters	**Idealized Storms**	**Hurricane 1938**
Radius of Maximum Wind (R_{max})	25 km (small), 50 km (large)	21∼72 km (32.5 km on average)
Translation Speed (U_T)	3 m/s (slow) 6 m/s (medium), 9 m/s (fast)	5.6∼21.6 m/s (12 m/s on average)
Maximum Winds (V_{max})	50 m/s	31∼72 m/s (62 m/s on average)

The final wind fields were then constructed by adding the inflow angles and the effects of translation speed following *Moon et al.* (2003). The inflow angles create cross-isobar (ageostrophic) wind component and the translation speed imposes asymmetry to

the axisymmetric tropical cyclone vortex.

1.2.2.b Specification of Winds in the Historic Hurricane

In addition to the idealized hurricanes, we also simulated the historic 1938 New England Hurricane. It is the most powerful hurricane in the recorded history that affected the Southern New England, causing property losses estimated at $400 million at that time (*Pierce*, 1939). The storm made landfall in Long Island on 21 September 1939 as a Category 3 hurricane (storm characteristics are listed in Table 1.2). Before making landfall, its forward speed experienced dramatic increase and reached 70 mph ($\sim$ 30 m/s) (*Pierce*, 1939; *Landsea et al.*, 2014). Because its northward translation direction happened to align with the wind direction to the east of the storm, the fast forward speed increased the right-quadrant wind speeds far more than in a typical hurricane.

The parametric hurricane wind is generated using parameters reported in the best track files obtained from the NOAA National Hurricane Center (NHC) North Atlantic Hurricane database (HURDAT2) (*Landsea et al.*, 2014). This is a re-analyzed best track database covering years from 1851 to 2016. The track files for historical storms only include the storm center position, maximum wind speed and central pressure. For Hurricane 1938, the central pressure information is unavailable for most of the storm period.

We have utilized the six available records of central pressure and have estimated the missing central pressure information by relating pressure deficit ($P_n - P_c$) to the maximum wind speed squared (V_{max}^2) through linear best fit according to Equation (1.2). Two assumptions were made. First, environmental pressure was assumed to be 1010 hPa. Second, we assumed a linear relation between the maximum wind speed squared and pressure deficit. This assumption seems reasonable for maximum wind speed between 60 and 140 knots (Figure 6b in *Knaff and Zehr* (2007)). The maximum pressure drop estimated is 104 hPa with the corresponding maximum wind speed of 71.4 m/s. Since *Knaff and Zehr* (2007) proposed to use storm-relative maximum wind for wind-pressure relationship, we also estimated the pressure deficit using the storm-relative maximum wind speed

and confirmed that the pressure drop estimated in these two ways are similar (not shown). R_{max} was then calculated using the empirical formula suggested in *Vickery et al.* (2000),

$$\ln R_{max} = 2.636 - 0.00005086\Delta p^2 + 0.0394899\psi \tag{1.3}$$

where Δp is the central pressure deficit (in hectopascal) and ψ is latitude of storm center (in degree). This formulation was derived from historical data for hurricane wind simulations in the Atlantic Basin, especially for storms located north of 30 °N. As in the idealized experiments, the final wind fields were constructed by adding the inflow angles and the translation speeds. The characteristics of Hurricane 1938 during its life span is shown in Figure 1.2.

1.2.3 Experimental Design

We conducted experiments with four different spatial resolutions 1/3°, 1/6°, 1/12° and 1/24° for six idealized hurricanes (listed in Table 1.2) moving in four different directions, as shown in Figure 1.3. The purpose of simulating different storm translation directions is to investigate whether the results are affected by the direction of storm movement relative to the grid point locations. The computational domain size is set to 30° long in longitudinal direction and 26° wide in latitudinal direction. In all idealized experiments, the initial storm center was positioned 2° from the right and 8° from the bottom edge of the computational domain. This setting ensures enough domain space for simulation of the 9 m/s translating TC and avoids potential spurious effects caused by staying too close to the domain boundary. The water depth is horizontally uniform and set to 4000 m. The input wind field was constructed at the highest $\frac{1}{24}^\circ$ resolution grid. In the low resolution grids, the wind vectors were identical to the highest resolution grid at the common grid points. No spatial interpolation of the wind field was done between different grid resolutions. The input wind was updated every 15 min in the model. A higher wind input frequency of 5 min was tested and the differences in the results were found to be insignificant. Depending on the translation speed of TCs, both wave models were integrated for 72 h (3 m/s) or 78 h (6 and 9 m/s) to ensure the wave field reaches

quasi-steady state.

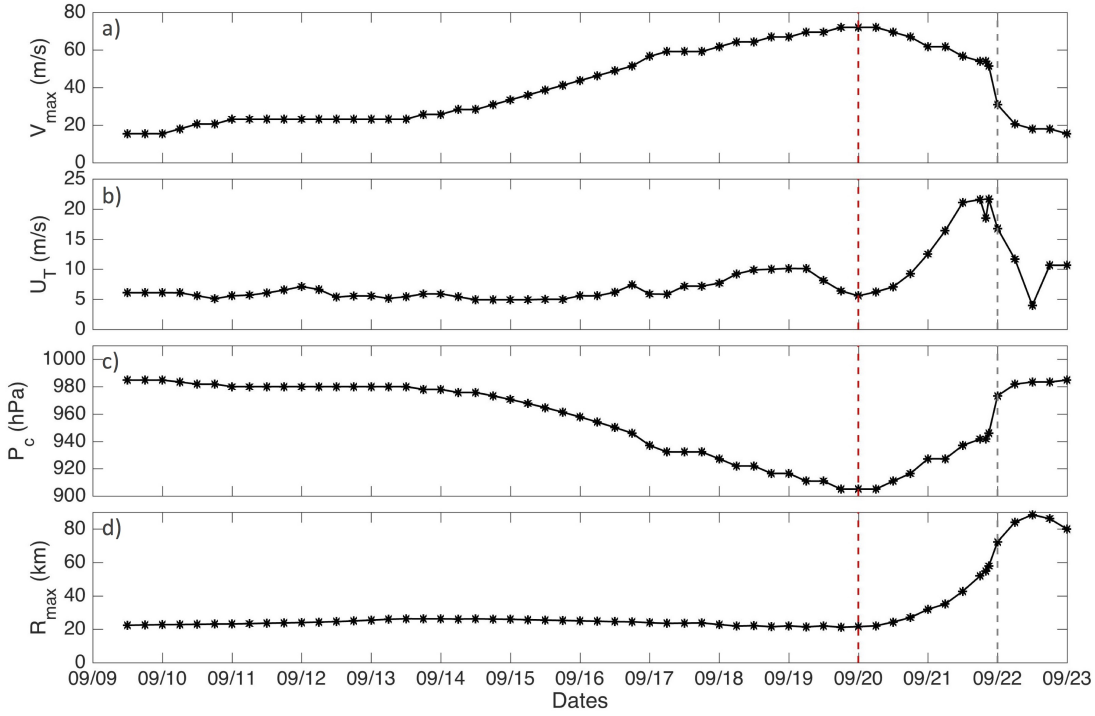

Figure 1.2: Characteristics of the 1938 New England Hurricane from 9 September 1938 to 23 September 1938. Panel a) to d) shows maximum wind speed (V_{max}), translation speed (U_T), central pressure (P_c) and radius of maximum wind (R_{max}), respectively. The latter two quantities are estimated. Red dashed line indicates the time when the hurricane is most intense (indicated by a minimum in central pressure); gray dashed line indicates the time of landfall in Rhode Island.

To solve the multi-timescale wave balance equation, WW3 applies a fractional step method that utilizes four different time steps: the global time step ($\Delta t_{g_{max}}$), time steps for spatial propagation ($\Delta t_{xy_{max}}$) and directional propagation ($\Delta t_{\theta_{max}}$), and a time step for the source term integration ($\Delta t_{src_{min}}$) (*The WAVEWATCH III® Development Group*, 2016). Note that the spatial and directional propagation time steps are constrained by the Courant–Friedrichs–Lewy (CFL) condition. SWAN implements a different technique using an action density limiter to restrict the rate of change of the energy spectrum at each time step (*The SWAN team*, ver41.10). Therefore, only one global time step is used. The specific settings of the time steps in both models are listed in Table 1.3.

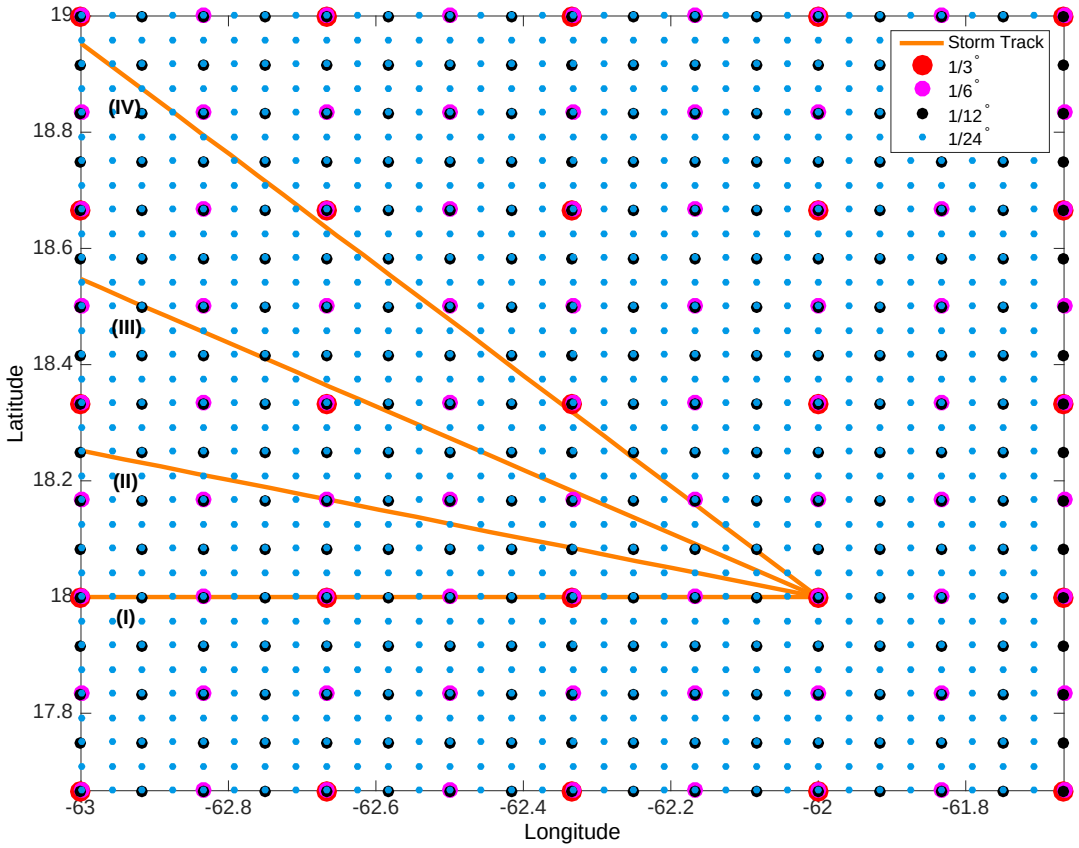

Figure 1.3: Configuration of model grids of different resolutions and storm tracks are shown in the southeast part of the computational domain. The storm tracks in four different directions are shown in orange. Size and color of the grid points denote the resolution. Red, magenta, black and cyan represent grid points in 1/3°, 1/6°, 1/12° and 1/24° resolutions, respectively. The angle of tracks are 180°, 165°, 150°, and 135° (0° at positive x-axis).

Table 1.3: Spatial resolutions and corresponding numerical time steps set in two models.

Spatial Resolution	WW3				SWAN
	$\Delta t_{g_{max}}$	$\Delta t_{xy_{max}}$	$\Delta t_{\theta_{max}}$	$\Delta t_{src_{min}}$	Δt
1/3°	300s	237s	118s	30s	300s
1/6°					
1/12°					
1/24°		118s	59s		

The wave simulations for Hurricane 1938 were performed with 1/3° and 1/12° grid resolutions in a computational domain covering 85 °W to 55 °W and 10 °N to 45 °N. The model bathymetry was specified using the ETOPO1 1 arc-minute global Relief Model

developed by the U.S. National Geophysical Data Center (NGDC) and spatially interpolated onto the given grid resolutions in Table 1.3.

1.3 Results

1.3.1 Idealized Tropical Cyclone Wave Simulations

Results of the idealized TC experiments with both WW3 and SWAN models are presented in terms of five different quantities in a time-averaged quasi-steady wave field, namely, the maximum significant wave height (SWH), the spatial distribution of SWH, the (half-annulus) averaged wave energy, the spatial distribution of mean wavelength, and the time series of SWH at virtual buoys.

The time-averaged quasi-steady wave field was obtained by averaging hourly-output TC wave fields in a storm-following reference frame, over the last 24 h in quasi-steady state. Before time averaging, every instantaneous model output from a coarser resolution case was interpolated onto the $1/24^{\circ}$ resolution grid points, which were used as the common grid points for comparing the results. The aforementioned five quantities were then obtained from this time-averaged wave field to remove potential numerical fluctuations due to a coarse resolution. Obtaining the SWH time series from this averaged wave field deserves some explanation. Because space and time are equivalent for the quasi-steady state wave field, a SWH time series is essentially a transect taken from the time averaged wave field in x direction at certain distance from the TC center. In the following analyses, we used the $1/24^{\circ}$ resolution results as our benchmark results (i.e., the most accurate results), and used the terms "overestimation" and "underestimation" to describe the model results with coarser resolutions in comparison to the benchmark cases.

1.3.1.a Comparison of Maximum Significant Wave Heights

Figure 1.4 shows the maximum SWH from all simulations, with two different wave models, with six different idealized storms, with four different resolutions, and with four different storm propagation directions. As expected, larger and faster moving storms generate

larger waves and hence higher values of maximum SWH. Varying spatial resolution in wave models as well as storm track direction affects the maximum SWH simulations. In general, for a fixed translation direction, as the storm moves faster, the $1/3^{\circ}$ resolution tends to underestimate the maximum SWH. The largest errors of the maximum SWH reaches 1 m (about 6 %) in WW3 and 2 m (about 16 %) in SWAN with the $1/3^{\circ}$ resolution. For a fixed resolution, the maximum SWH displays variability introduced by TC translation direction. In both models, this variability is reduced and the SWH results converge as the spatial resolution becomes finer. However, this convergence is slower in SWAN than that in WW3. Figure 1.4 also informs that, in both models, the variability caused by TC translation direction is comparable to the errors due to model resolution. Only with the $1/3^{\circ}$ grid resolution and under the storm with a small R_{max} (large wind gradient) and a large translation speed (fast moving), the variation of SWH due to TC direction becomes significant. This is again more evident in SWAN.

In summary, model errors in maximum SWH (see Table 1.4) can be significant with coarser resolutions under a small and fast moving storm ($R_{max} = 25$ km, $U_T = 9$ m/s), using SWAN in particular. The sensitivity of maximum SWH to spatial resolution is model dependent and there are no systematic trends that are common in both models. This model dependency may be partly caused by the differences in their source terms. We have conducted the same experiments with WW3 but changed the source terms from ST4 to ST2 (*Tolman and Chalikov* (1996)), and found different sensitivity to the spatial resolution (not shown).

1.3.1.b Comparison of Spatial Distribution of Significant Wave Heights

In terms of practical interest, it is also important to compare spatial distribution of SWH in hurricanes simulated at different spatial resolutions, which is not represented by the previous comparison of maximum SWH. For simplicity, only the results generated by horizontally-moving storms are presented hereafter.

In Figures 1.5 and 1.6, the SWH fields simulated with the $1/3^{\circ}$ and $1/24^{\circ}$ grids

are compared in a domain of $4R_{max}$ by $4R_{max}$ around the storm center. The difference between the two is shown in the right column.

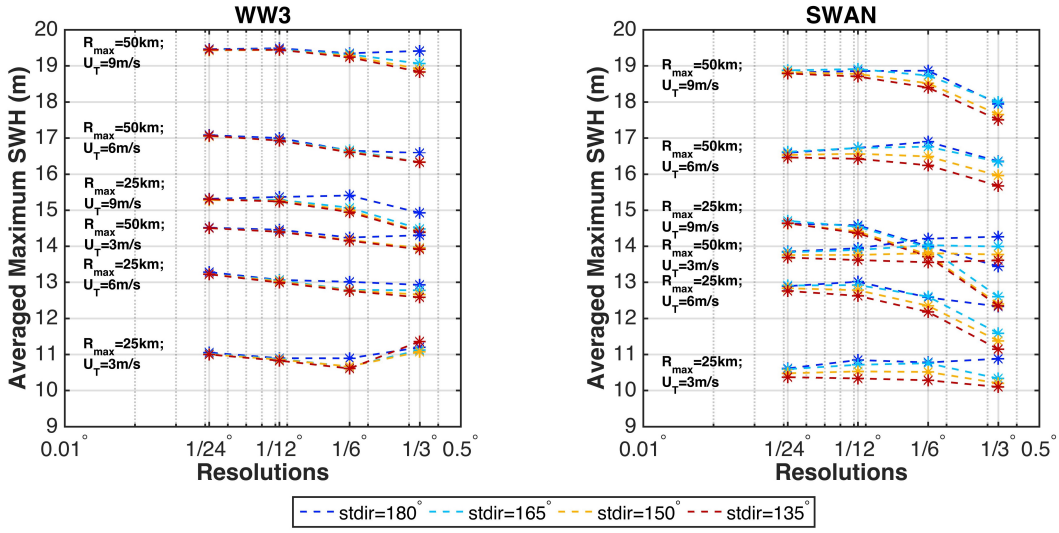

Figure 1.4: Maximum SWH in time-averaged quasi-steady state wave fields simulated with six different idealized storms, with four different spatial resolutions, and with four different storm propagation directions: (**a**) WW3 results; and (**b**) SWAN results. Dashed lines of different colors represent different directions, with track (I) in blue, track (II) in cyan, track (III) in yellow and track (IV) in red. Asterisk marker denotes the actual data point.

Table 1.4: Largest absolute errors in maximum SWH with different resolutions relative to results with the highest resolution (1/24°).

R_{max} (km)	U_T (m/s)	1/3°		1/6°		1/12°	
		WW3	SWAN	WW3	SWAN	WW3	SWAN
25	3	3.3%	2.6%	3.5%	1.6%	1.6%	2.2%
	6	4.8%	12.6%	3.5%	4.6%	1.7%	1.1%
	9	6.0%	15.7%	2.3%	6.3%	0.4%	1.9%
50	3	4.1%	3.0%	2.4%	2.6%	0.7%	0.7%
	6	4.3%	4.8%	2.7%	1.8%	0.8%	0.8%
	9	3.2%	6.8%	1.1%	2.1%	0.1%	0.4%

In WW3 (Figure 1.5), the coarse resolution results with slow moving (3 m/s) storms significantly overestimate the small SWH near the storm center inside R_{max} but the errors are relatively small outside R_{max}. For fast moving storms (9 m/s), this overestimation near the storm center is reduced, but SWH in front of the storm near R_{max} is underesti-

mated (as much as 17%), and SWH further in front and further behind are overestimated (as much as 50%) with the coarse resolution. The overall errors in SWH appear to be the largest for smaller and faster moving storms with coarser model resolutions.

In SWAN (Figure 1.6), the overall error patterns are qualitatively similar to those in WW3. However, the underestimation of SWH with the coarser resolution in front of the storm is more significant (23%) and affects a larger area in the fast moving storms. The overestimation of SWH (27%) further in front of the storm (within $4R_{max}$) tends to be smaller in comparison to WW3.

In summary, in both models, the spatial distribution of SWH appears to be most sensitive to the model spatial resolution for small (R_{max}=25 km) and fast moving (U_T=9 m/s) hurricanes, with the error magnitude exceeding 2.5 m in some locations.

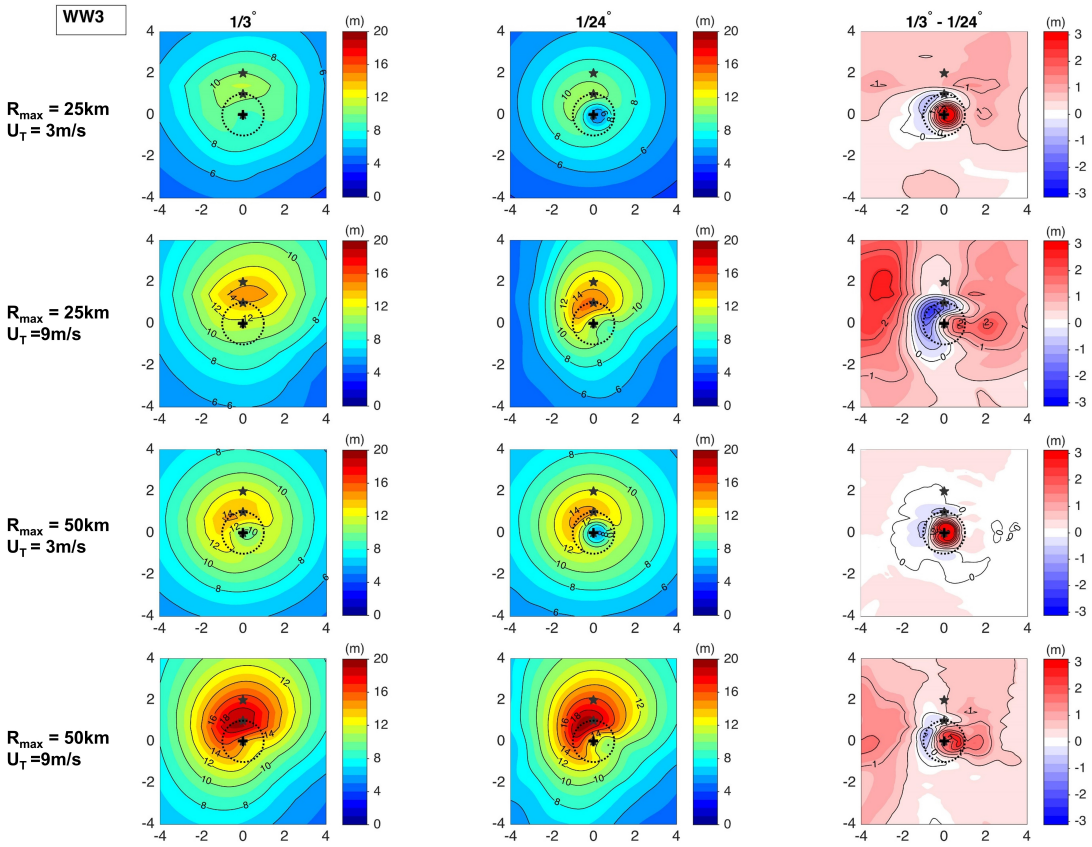

Figure 1.5: Spatial distribution of SWH in time-averaged quasi-steady state wave fields from WW3. The results computed: at $1/3^{\circ}$ resolution (**left**); and at $1/24^{\circ}$ resolution (**right**). The black contours have an increment of 3 m. The differences between the left and center columns, and the black contours are drawn every 0.5 m (**right**). Distances are normalized by R_{max}. The black dotted circle denotes R_{max}. Filled black stars on each panel denote the location of virtual buoys discussed in Section 1.3.1.e) .

1.3.1.c Comparison of Half-Annulus Averaged Wave Energy

Our analysis in the previous section suggests that the errors in SWH due to the coarse model resolution vary with the distance from the storm center, as well as whether the location is in front or behind the storm center. Here, we explore the model errors further by comparing the averaged wave energy in front and behind the storm center. By definition, the square of SWH is proportional to the total wave energy per unit surface area, integrated over the entire directional spectrum in the model. Here, we compare

the half-annulus averaged wave energy in the front and rear halves of the storm (relative to the storm center). Specifically, we draw a series of circles, with their radii ranging from 0 to $5R_{max}$ with an increment of $0.2R_{max}$, and define a series of annuli between the two successive circles. We further divide each annulus into front half and rear half, and compute the average wave energy in each half-annulus region.

Figures 1.7 and 1.8 show the half-annulus averaged wave energy computed in this manner in all the simulations with WW3 and SWAN, respectively. The averaged wave energy is always higher in the front half (negative normalized distance) than in the rear half (positive normalized distance) of the storm. This asymmetry is more significant in large and fast moving storms. The wave energy peaks near R_{max} are not well resolved with the $1/3^{\circ}$ resolution in both models, especially for the small storms. The coarse resolution simulations overestimate the wave energy near the storm center in most cases (except the small fast moving storm with SWAN). The overestimation of wave energy in the far field with the $1/3^{\circ}$ resolution (in WW3 only) is also noticeable. In small storms, the cumulative wave energy within a $5R_{max}$ circular area is about 20% higher in the $1/3^{\circ}$ simulation than in the $1/24^{\circ}$ simulation. Spatially, there are no systematic biases in the wave energy errors due to the coarse resolutions, which suggests these errors cannot be mitigated empirically. Moreover, the model sensitivity to the grid resolution in the front of the storm is very different from that behind the storm. These results suggest that projecting the high resolution TC wind field on the coarse resolution grid, which would smooth the wind field and reduce wind input both near the front peak and near the rear peak, is not the only reason for the errors in the wave simulations. The result from an additional sensitivity experiment, where a spatially smoothed wind field at $1/3^{\circ}$ grid resolution is used to force WW3 at the highest spatial resolution, further confirms this argument (see Appendix A).

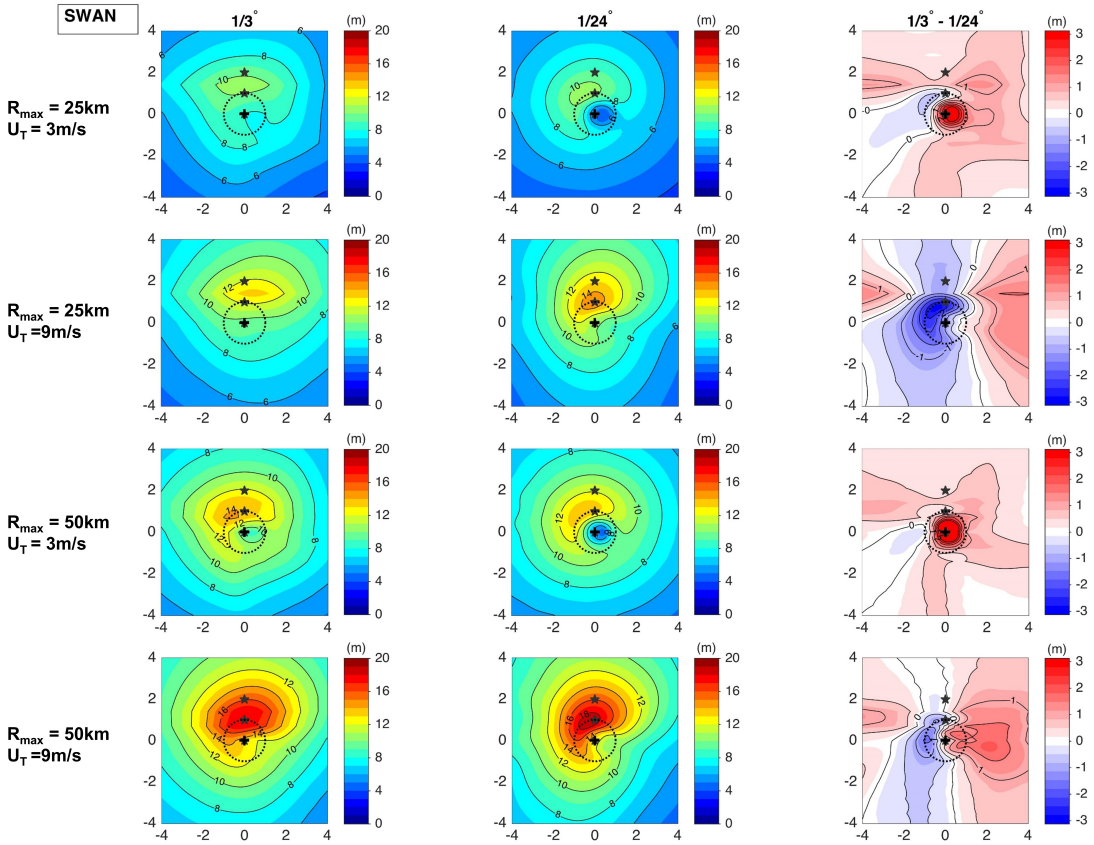

Figure 1.6: Spatial distribution of SWH in time-averaged quasi-steady state wave fields from SWAN. The results computed: at $1/3^{\circ}$ resolution (**left**); and at $1/24^{\circ}$ resolution (**right**). The figure format is the same as in Figure 1.5

1.3.1.d Comparison of Spatial Distribution of Mean Wavelength

We next investigated how the simulated mean wavelength (MWL) is affected by the different model resolutions. Unfortunately, there is no common definition of the mean wavelength shared by WW3 and SWAN. In WW3, MWL is defined as the wavelength weighted averaged by spectral density. In SWAN, MWL is defined as the wavelength associated with the mean wavenumber (MWN), which is the wavenumber weighted averaged by spectral density. These different definitions partially explain the different spatial patterns of MWL seen in Figures 1.9 and 1.10.

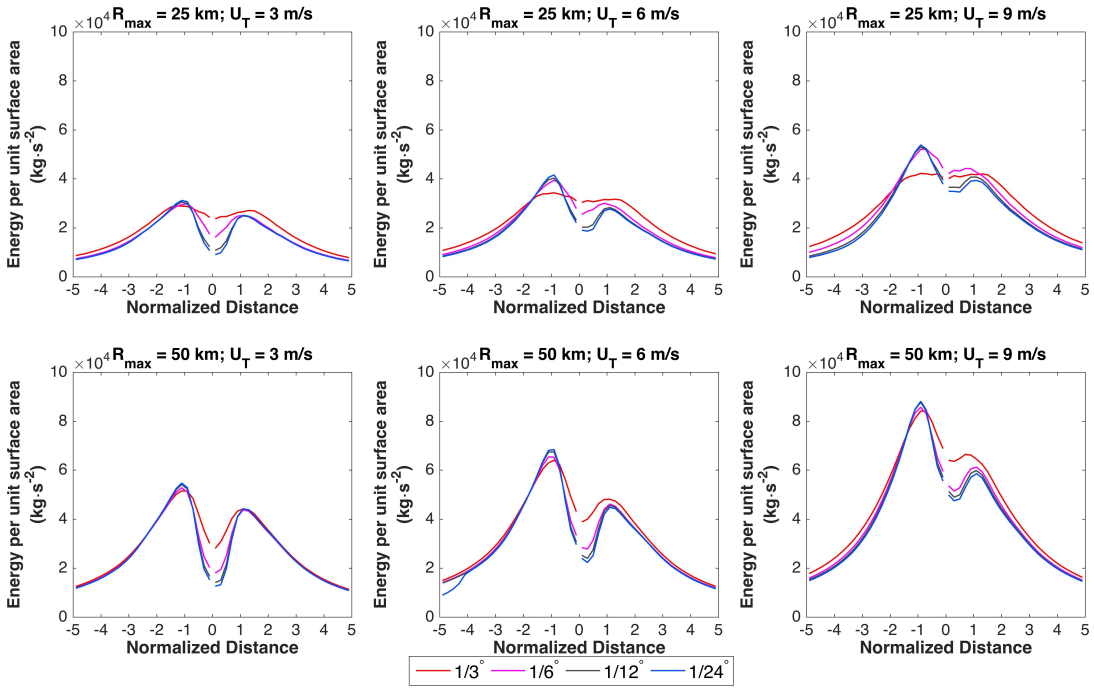

Figure 1.7: Average wave energy within a half-annulus area (front and rear) at different radii from the storm center under the six idealized storms from WW3. Red, magenta, black and blue lines denote results from the coarsest to the highest resolution.

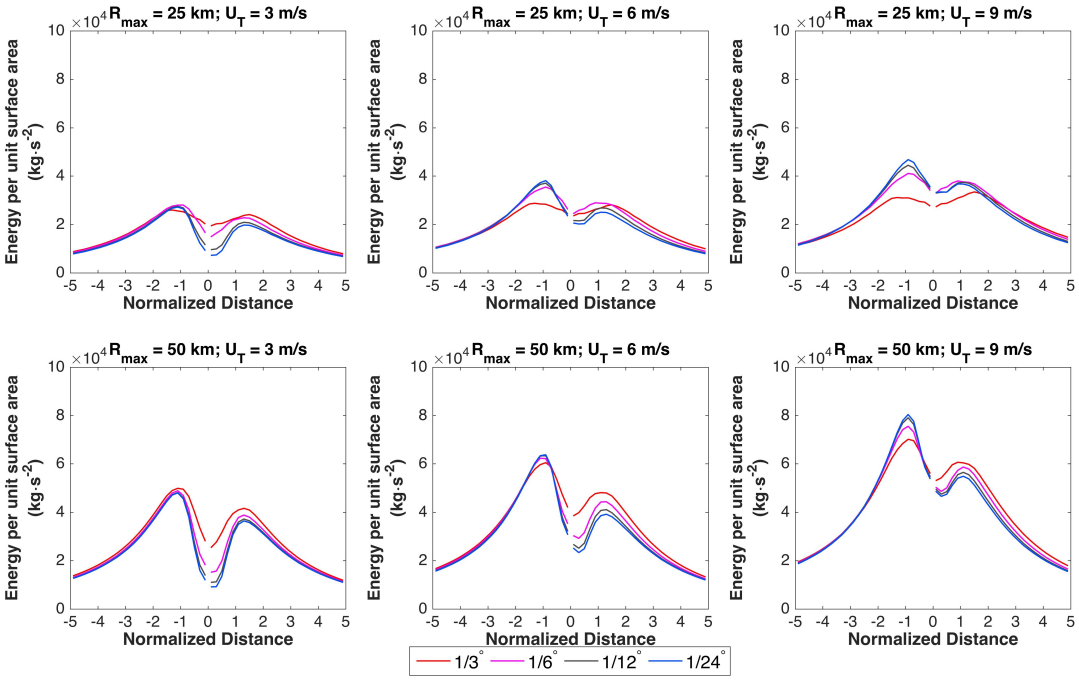

Figure 1.8: Average wave energy within a half-annulus area (front and rear) at different radii from the storm center under the six idealized storms from SWAN. Red, magenta, black and blue lines denote results from the coarsest to the highest resolution.

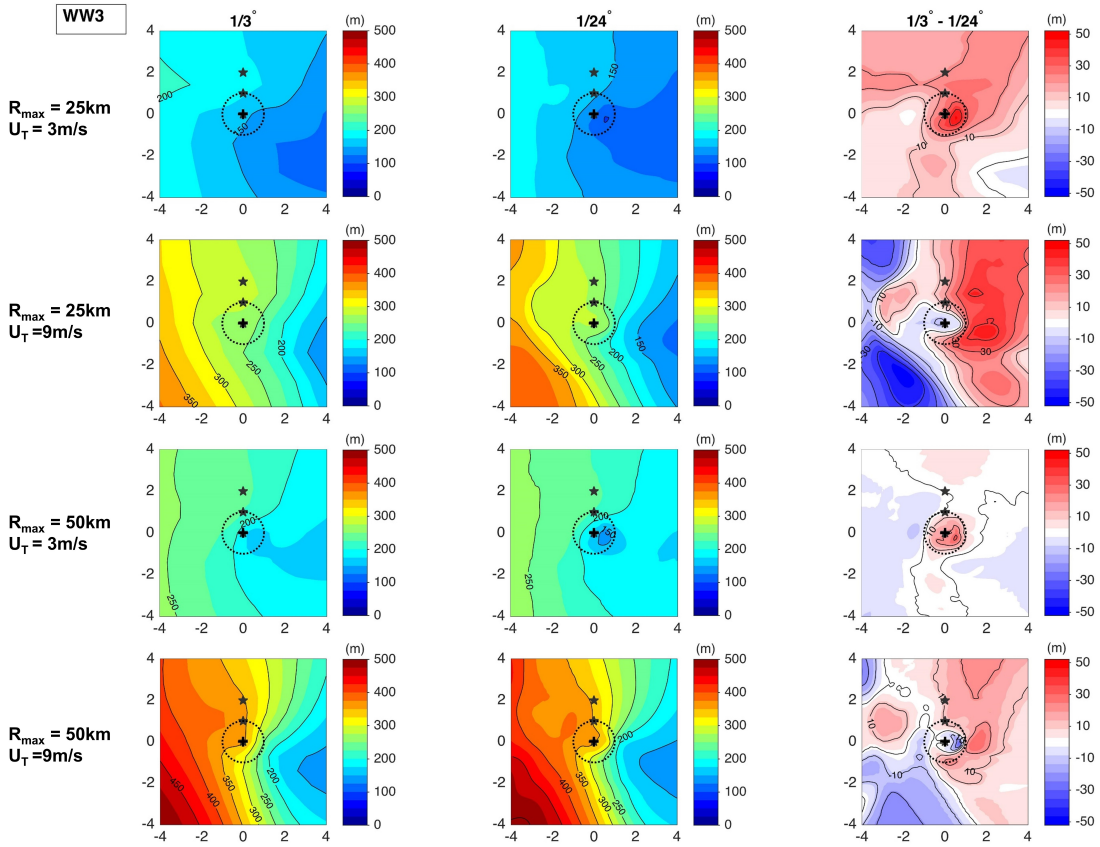

Figure 1.9: Spatial distribution of mean wavelength (wavelength weighted averaged by spectral density) in time-averaged quasi-steady state wave fields from WW3. The figure format is the same as Figure 1.5.

Figure 1.9 shows that MWL in WW3 monotonically increases in the direction of storm propagation, in general. This is because only longer swells can propagate ahead of the storm. The MWL errors in the $1/3^{\circ}$ resolution are as large as 50 m in the small and fast moving storm. The overall effect of a coarse grid is underestimation of the wavelength of swells ahead of the storm and overestimation of the wavelength of wind seas within the storm.

In SWAN, the presence of long swells ahead of storms have a smaller contribution to its MWL by definition, because MWN is not dominated by long swells. Therefore, the characteristic wavelength ahead of the storm in Figure 1.10 is significantly shorter than the one in Figure 1.9. Nevertheless, the errors due to the coarse resolution are as large as 50 m in some cases/locations for this characteristic wavelength.

1.3.1.e Comparison of SWH at Virtual Buoys

To further assess impacts of different model spatial resolutions, we compared the SWH time series at select locations, hereafter "virtual buoys". We deployed three virtual buoys at the storm center, at the R_{max} and $2R_{max}$ to the right of the storm center (locations shown in Figures 1.5 and 1.6). Figure 1.11 shows the SWH time series under the small and fast moving storm at these three buoys in both WW3 and SWAN.

The results from both wave models show similar impacts of the coarse resolutions, especially $1/3^{\circ}$. Firstly, the duration of SWH exceeding a certain magnitude, e.g., 4 m, is extended with the coarse resolutions, because SWH further away from the storm are overestimated. Secondly, the arrival time of the highest SWH is delayed by up to 0.5$\sim$1 h at all three buoys. Thirdly, the maximum SWH is significantly underestimated at the two buoys closer to the storm center. These virtual buoy records are consistent with the previously discussed SWH spatial maps for different resolutions. They confirm that the $1/3^{\circ}$ resolution simulations are not capable of accurately simulating the structure of the TC wave field.

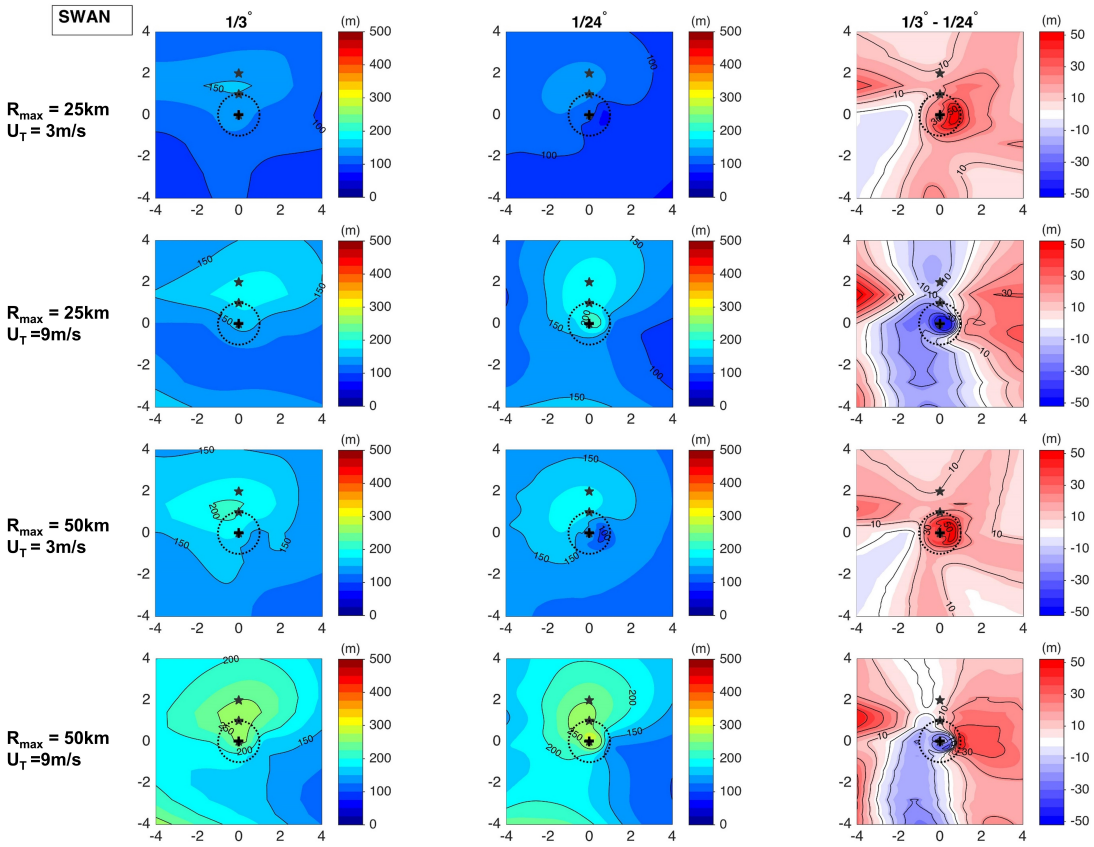

Figure 1.10: Spatial distribution of wavelength corresponding to mean wavenumber (wavenumber weighted averaged by spectral density) in time-averaged quasi-steady state wave fields from SWAN. The figure format is the same as Figure 1.5.

1.3.2 Wave Simulations under the 1938 New England Hurricane

To examine if our findings from the above idealized experiments are applicable to real TCs, wave simulations with different spatial resolutions are performed for the 1938 New England Hurricane. This hurricane is chosen because its Rmax remained relatively small for a long period of time offshore and it had an unusually fast translation speed (see Figure 1.2).

Figure 1.12 shows the swaths of maximum SWH with two different resolutions, 1/3° (left column) and 1/12° (center column), using WW3 (top row) and SWAN (bottom row). These swaths are constructed by finding the maximum value of the SWH time series during the storm passage at each grid point.

The largest waves are generated near the Cape Hatteras around 35°N. From the swath difference shown in the right columns, we notice that the maximum waves are underestimated in the 1/3° simulation by up to 1 m (5.3%) in WW3 and up to 1.5 m (8.3%) in SWAN. The degree of underestimation in the peak waves with the coarse resolution is consistent with what we have found in the idealized experiments. To summarize, this real case simulation further confirms that using the 1/3° spatial resolution can lead to significant errors in wave predictions under a small and fast moving TC.

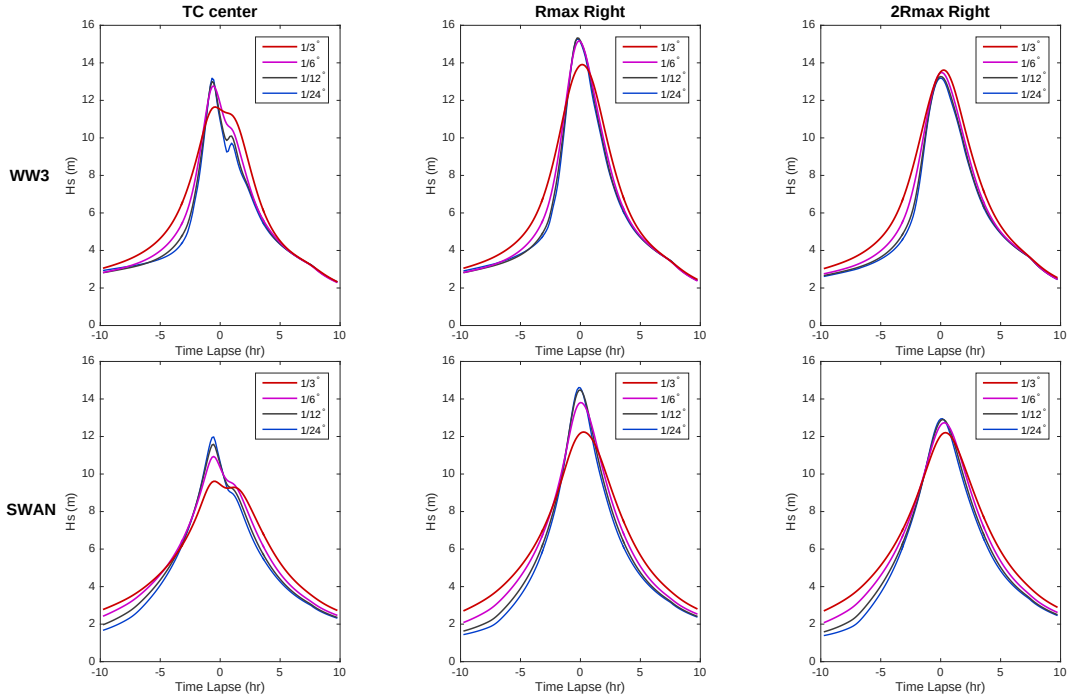

Figure 1.11: Time series of SWH at three virtual buoys (locations shown in Figures 1.5 and 1.6) under the small (RMW = 25 km) and fast moving (U_T = 9 m/s) storm: from WW3 (**top row**); and from SWAN (**bottom row**). SWH time series recorded at : storm center (**left column**); R_{max} to the right of storm center (**center column**); and $2R_{max}$ to the right of storm center (**right column**). Red, magenta, black and blue lines denote results from the coarsest to the finest resolution.

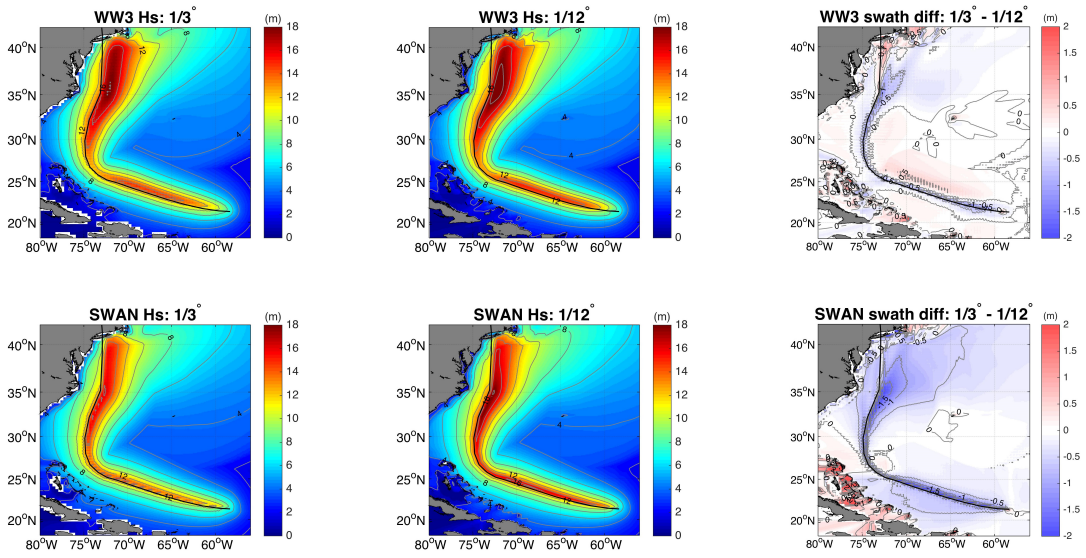

Figure 1.12: Comparison of swath of maximum SWH: in a 1/3° simulation (**left column**); and in a 1/12° simulation (**center column**); and their difference (**right column**), under Hurricane 1938. (**top row**) WW3 results; and (**bottom row**) SWAN results. Hurricane track is denoted by the black solid line. Contour increment for swath is 3 m. Contour increment for swath difference is 0.5 m.

1.4 Conclusions and Discussion

We conducted the first modeling study quantifying the sensitivity of TC wave simulations to spatial resolutions in open ocean. Based on the results from a series of idealized experiments with two widely used wave models, WW3 and SWAN, main conclusions can be summarized as follows.

1. Wave model sensitivity to spatial resolution depends on storm characteristics. Waves generated under a small and fast moving storm (R_{max}=25 km, U_T=9 m/s in this study) appear to be most sensitive to a coarse resolution.

2. Under a small and fast moving storm, using the 1/3° spatial resolution can lead to underestimation of the maximum SWH by 6% in WW3(ST4) and 16% in SWAN(ST1). The local SWH in front of the storm near R_{max} can be underestimated by as much as 17% in WW3 and 23% in SWAN.

3. In all six idealized storms, the coarsest resolution of $1/3^{\circ}$ causes the largest errors in both SWH and MWL. In general, the sensitivity to model spatial resolution is larger in SWAN(ST1) than that in WW3(ST4).

4. The errors due to spatial resolution are comparable to those due to different physics parameterizations in wave models, which are on the order of 5%∼10% (*Liu et al.*, 2017).

Based on our experimental results, the following recommendations can be made on the spatial resolution threshold required for different applications. For predictions of the maximum SWH with ∼5% accuracy, a resolution higher than $1/3^{\circ}$ is recommended for WW3(ST4), and a resolution higher than $1/6^{\circ}$ is recommended for SWAN(ST1). However, to predict spatial patterns of TC waves within ∼5% error, the spatial resolution has to be higher than $1/6^{\circ}$ in both models (Table A.1 in Appendix).

In the current NOAA WW3 operational hurricane wave model ($1/10^{\circ}$ resolution), the model error due to spatial resolution is estimated to be less than 5%. In the ADCIRC-SWAN real-time guidance system *Fleming et al.* (2008), the mesh resolution over the open ocean needs to be refined to at least $1/6^{\circ}$ to make the SWAN wave predictions reasonably accurate. Meanwhile, WW3(ST4) may be a better candidate for storm surge-wave coupling, since it is less sensitive to spatial resolution than SWAN(ST1).

Underestimating the peak of extreme waves under storms is a known limitation of the current third generation wave models (*Cavaleri*, 2009; *The WISE Group*, 2007). Potential reasons have been discussed in *Cavaleri* (2009) but the exact source of errors remains unknown. Although our study cannot provide an answer to this question, our results demonstrate that spatial smoothing of the wind field is not the only reason for the errors in wave simulations with coarse resolution grids (see Figure A.1 in Appendix A).

To investigate further the sensitivity of TC wave simulations to other numerical settings in WW3 and SWAN, we performed the following additional tests: (1) higher temporal resolution of input wind (increased from 15 min to wave model time step); (2) higher directional resolution of the wave spectrum (increased from 24 bins to 36 bins);

(3) higher model temporal resolution in SWAN (increased from 300 s to 120 s); and (4) reduction of splitting errors in WW3 due to four different time steps (set the four time steps to 30 s). In all of these experiments, changes in the maximum SWH predictions did not exceed 1%.

In conclusion, our study clearly demonstrates that a coarse spatial resolution such as $1/3^{\circ}$ is not suitable for simulating TC waves, particularly in smaller and faster moving storms. The results of this study raise questions regarding the accuracy of TC wave simulations with unstructured grids in the coupled ADCIRC-SWAN or similar systems that use coarse spatial resolutions in the open ocean region and its impacts on storm surge predictions. In the coupled storm surge-wave system, one important quantity used to account for wave impacts on storm surge is the radiation stress, which is essentially the spatial gradient of the wave field. Although this quantity is more significant in the shallow water region, where the spatial resolution is typically high, the coarse resolution errors in the offshore region may still impact the results if the incoming waves are significantly underestimated. More careful studies with different unstructured grid systems, including the coastal regions, are needed to fully examine the accuracy of the wave simulations and their impacts on storm surge.

REFERENCES

Akbar, M., S. Kanjanda, and A. Musinguzi (2017), Effect of Bottom Friction, Wind Drag Coefficient, and Meteorological Forcing in Hindcast of Hurricane Rita Storm Surge Using SWAN + ADCIRC Model, *Journal of Marine Science and Engineering*, *5*(4), 38, doi:10.3390/jmse5030038.

Ardhuin, F., et al. (2010), Semiempirical dissipation source functions for ocean waves. Part I: Definition, calibration, and validation, *Journal of Physical Oceanography*, *40*(9), 1917–1941, doi:10.1175/2010JPO4324.1.

Barber, N., and F. Ursell (1948), The generation and propagation of ocean waves and swell. i. wave periods and velocities, *Philosophical Transactions of the Royal Society of London A: Mathematical, Physical and Engineering Sciences*, *240*(824), 527–560, doi:10.1098/rsta.1948.0005.

Bunya, S., et al. (2010), A High-Resolution Coupled Riverine Flow, Tide, Wind, Wind Wave, and Storm Surge Model for Southern Louisiana and Mississippi. Part I: Model Development and Validation, *Monthly Weather Review*, *138*(2), 345–377, doi:10.1175/2009MWR2906.1.

Cavaleri, L. (2009), Wave modeling–missing the peaks, *Journal of Physical Oceanography*, *39*(11), 2757–2778, doi:10.1175/2009JPO4067.1.

Chawla, A., H. L. Tolman, V. Gerald, D. Spindler, T. Spindler, J.-H. G. M. Alves, D. Cao, J. L. Hanson, and E.-M. Devaliere (2013), A multigrid wave forecasting model: A new paradigm in operational wave forecasting, *Weather and Forecasting*, *28*(4), 1057–1078, doi:10.1175/WAF-D-12-00007.1.

Dietrich, J. C., et al. (2010), A high-resolution coupled riverine flow, tide, wind, wind wave, and storm surge model for southern louisiana and mississippi. part ii: Synop-

tic description and analysis of hurricanes katrina and rita, *Monthly Weather Review*, *138*(2), 378–404, doi:10.1175/2009MWR2907.1.

Dietrich, J. C., et al. (2011), Modeling hurricane waves and storm surge using integrally-coupled, scalable computations, *Coastal Engineering*, *58*(1), 45–65, doi:10.1016/j.coastaleng.2010.08.001.

Donelan, M. A., M. Curcic, S. S. Chen, and A. K. Magnusson (2012), Modeling waves and wind stress, *Journal of Geophysical Research: Oceans*, *117*(7), doi:10.1029/2011JC007787.

Dresback, K. M., et al. (2013), Skill assessment of a real-time forecast system utilizing a coupled hydrologic and coastal hydrodynamic model during hurricane irene (2011), *Continental Shelf Research*, *71*(Supplement C), 78 – 94, doi:https://doi.org/10.1016/j.csr.2013.10.007.

Fan, Y., I. Ginis, T. Hara, C. W. Wright, and E. J. Walsh (2009), Numerical Simulations and Observations of Surface Wave Fields under an Extreme Tropical Cyclone, *Journal of Physical Oceanography*, *39*(9), 2097–2116, doi:10.1175/2009JPO4224.1.

Feng, X., B. Yin, and D. Yang (2016), Development of an unstructured-grid wave-current coupled model and its application, *Ocean Modelling*, *104*, 213 – 225, doi:https://doi.org/10.1016/j.ocemod.2016.06.007.

Fleming, J. G., C. W. Fulcher, R. A. Luettich, B. D. Estrade, G. D. Allen, and H. S. Winer (2008), A real time storm surge forecasting system using adcirc, in *Estuarine and Coastal Modeling (2007)*, pp. 893–912, doi:10.1061/40990(324)48.

Haiden, T., M. Janousek, J. Bidlot, L. Ferranti, F. Prates, F. Vitart, P. Bauer, and D. Richardson (2016), *Evaluation of ECMWF forecasts, including the 2016 resolution upgrade*.

Hasselmann, K. (1974), On the spectral dissipation of ocean waves due to white capping, *Boundary-Layer Meteorology*, *6*(1), 107–127, doi:10.1007/BF00232479.

Holland, G. J. (1980), An analytic model of the wind and pressure profiles in hurricanes., *Monthly Weather Review*, *108*(8), 1212–1218, doi:10.1175/1520-0493(1980)108<1212:AAMOTW>2.0.CO;2.

Huang, Y., R. H. Weisberg, L. Zheng, and M. Zijlema (2013), Gulf of Mexico hurricane wave simulations using SWAN: Bulk formula-based drag coefficient sensitivity for Hurricane Ike, *Journal of Geophysical Research: Oceans*, *118*(8), 3916–3938, doi:10.1002/jgrc.20283.

Janssen, P. (2004), *The Interaction of Ocean Waves and Wind*, Cambridge University Press, doi:10.1017/CBO9780511525018.

Kerr, P. C., et al. (2013), U.S. IOOS coastal and ocean modeling testbed: Evaluation of tide, wave, and hurricane surge response sensitivities to mesh resolution and friction in the Gulf of Mexico, *Journal of Geophysical Research: Oceans*, *118*(9), 4633–4661, doi:10.1002/jgrc.20305.

Knaff, J. A., and R. M. Zehr (2007), Reexamination of tropical cyclone wind-pressure relationships, *Weather and Forecasting*, *22*(1), 71–88, doi:10.1175/WAF965.1.

Komen, G. J., S. Hasselmann, and K. Hasselmann (1984), On the existence of a fully developed wind-sea spectrum, *Journal of Physical Oceanography*, *14*(8), 1271–1285, doi:10.1175/1520-0485(1984)014<1271:OTEOAF>2.0.CO;2.

Landsea, C. W., A. Hagen, W. Bredemeyer, C. Carrasco, D. A. Glenn, A. Santiago, D. Strahan-Sakoskie, and M. Dickinson (2014), A reanalysis of the 1931-43 atlantic hurricane database, *Journal of Climate*, *27*(16), 6093–6118, doi:10.1175/JCLI-D-13-00503.1.

Liu, Q., A. Babanin, Y. Fan, S. Zieger, C. Guan, and I. J. Moon (2017), Numerical simulations of ocean surface waves under hurricane conditions: Assessment of existing model performance, *Ocean Modelling*, *118*, 73–93, doi:10.1016/j.ocemod.2017.08.005.

Longuet-Higgins, M., and R. Stewart (1964), Radiation stresses in water waves; a physical discussion, with applications, *Deep Sea Research and Oceanographic Abstracts*, *11*(4), 529 – 562, doi:https://doi.org/10.1016/0011-7471(64)90001-4.

Moon, I.-J., I. Ginis, T. Hara, H. L. Tolman, C. W. Wright, and E. J. Walsh (2003), Numerical simulation of sea surface directional wave spectra under hurricane wind forcing, *Journal of Physical Oceanography*, *33*(8), 1680–1706, doi:10.1175/2410.1.

Pierce, C. H. (1939), The meterological history of the new england hurricane of sept. 21, 1938, *Monthly Weather Review*, *67*(8), 237–285, doi:10.1175/1520-0493(1939)67<237:TMHOTN>2.0.CO;2.

Reichl, B. G., T. Hara, and I. Ginis (2014), Sea state dependence of the wind stress over the ocean under hurricane winds, *Journal of Geophysical Research: Oceans*, *119*(1), 30–51, doi:10.1002/2013JC009289.

Rogers, W. E., P. A. Hwang, and D. W. Wang (2003), Investigation of wave growth and decay in the swan model: Three regional-scale applications, *Journal of Physical Oceanography*, *33*(2), 366–389, doi:10.1175/1520-0485(2003)033<0366:IOWGAD>2.0.CO;2.

Shimura, T., N. Mori, and M. A. Hemer (2017), Projection of tropical cyclone-generated extreme wave climate based on CMIP5 multi-model ensemble in the Western North Pacific, *Climate Dynamics*, *49*(4), 1449–1462, doi:10.1007/s00382-016-3390-2.

Sun, Y., C. Chen, R. C. Beardsley, Q. Xu, J. Qi, and H. Lin (2013), Impact of current-wave interaction on storm surge simulation: A case study for hurricane bob, *Journal of Geophysical Research: Oceans*, *118*(5), 2685–2701.

The SWAN team (ver41.10), SWAN Scientific and Technical Documentation (Cycle III version 41.10A), *Tech. note*, Delft University of Technology, 140 pp.

The WAVEWATCH III ® Development Group (2016), User manual and sys-

tem documentation of WAVEWATCH III ® version 5.16, *Tech. Note 329*, NOAA/NWS/NCEP/MMAB, College Park, MD, USA, 326 pp. + Appendices.

The WISE Group (2007), Wave modelling - The state of the art, *Progress in Oceanography*, *75*(4), 603–674, doi:10.1016/J.POCEAN.2007.05.005.

Tolman, H. L., and J.-H. G. Alves (2005), Numerical modeling of wind waves generated by tropical cyclones using moving grids, *Ocean Modelling*, *9*(4), 305–323, doi:10.1016/j.ocemod.2004.09.003.

Tolman, H. L., and D. Chalikov (1996), Source terms in a third-generation wind wave model, *Journal of Physical Oceanography*, *26*(11), 2497–2518, doi:10.1175/1520-0485(1996)026<2497:STIATG>2.0.CO;2.

Vickery, P. J., P. F. Skerlj, and L. A. Twisdale (2000), Simulation of Hurricane Risk in the U.S. Using Empirical Track Model, *Journal of Structural Engineering*, *126*(10), 1222–1237, doi:10.1061/(ASCE)0733-9445(2000)126:10(1222).

Wu, J. (1982), Wind-stress coefficients over sea surface from breeze to hurricane, *Journal of Geophysical Research: Oceans*, *87*(C12), 9704–9706, doi:10.1029/JC087iC12p09704.

Xu, Y., et al. (2017), Observations and Modeling of Typhoon Waves in the South China Sea, *Journal of Physical Oceanography*, *47*(6), 1307–1324, doi:10.1175/JPO-D-16-0174.1.

MANUSCRIPT 2

Impact of Shoaling Ocean Surface Waves on Wind Stress and Drag Coefficient in Coastal Waters: Part I Uniform Wind

Xuanyu Chen[1*], Tetsu Hara[1], and Isaac Ginis[1]

Published in Journal of Geophysical Research: Oceans, June 2020

[1]Graduate School of Oceanography, University of Rhode Island, Narragansett, Rhode Island

[*]Corresponding author email: xychen@my.uri.edu

Abstract

This study investigates the impact of shoaling wind waves on the drag coefficient in coastal waters. The shoaling wave spectrum is simulated using the WAVEWATCH III (WW3) model with shallow water physics. The high frequency part (spectral tail), which is unresolved in the wave model, is empirically parameterized as a function of wind speed. The full wave spectrum is then used to estimate the sea-state dependent wind stress and drag coefficient. Shoaling wind waves are simulated on a sloped bottom under the idealized steady uniform wind. Experimental wind speed spans from 10 m/s to 65 m/s, and the bottom slope is varied from 1:100 to 1:2000. Our results show that as water depth decreases, the drag coefficient increases gradually to a peak value and then rapidly reduces compared to the deep-water value. The maximum C_d value occurs roughly where depth-induced wave breaking starts. The magnitude of C_d enhancement is more significant on a steeper slope and can reach 40%. This C_d enhancement is mainly due to steepening of waves and reduction of the wave phase speed during the shoaling. Our results also suggest significantly larger variability of C_d at a given wind speed in finite depth waters than in deep water.

2.1 Introduction

Wind stress at the air-sea interface is a fundamental parameter for atmospheric, wave and ocean models. It is commonly parameterized using the drag coefficient (C_d) or the roughness length (z_0). In most applications, C_d is a function of the neutral 10-meter wind speed (U_{10}) corrected for stability. Over the past four decades, observations over the ocean provided a plethora of C_d–U_{10} relationships, which vary from one study to another (e.g., Fig. 2.1, solid lines). The large variability of the C_d–U_{10} relation can be a result of the sea-state dependence of wind stress.

It has been proposed that ocean surface gravity waves can modify the wind stress through a wave-induced stress component (or form drag) (e.g., *Janssen*, 1989; *Donelan et al.*, 1993). Decades of field observations (e.g., *Smith et al.*, 1992; *Donelan et al.*, 1997; *Janssen*, 1997; *Oost et al.*, 2002; *Edson et al.*, 2013, etc.) have supported this idea. Two common approaches of roughness length parameterization exist to account for the influence of sea states; namely the wave-age dependent z_0 and the wave-steepness dependent z_0 (*Drennan et al.*, 2005). However, such a simple parameterization of the wind stress is not sufficient because the variation of the wave-induced momentum flux is controlled by a full wave spectrum instead of a single parameter. Hence, explicit modeling of the wind stress based on a wave spectrum is likely more accurate. Over the years, different methods have been developed to model sea-state dependent wind stress in deep water (e.g., *Makin and Kudryavtsev*, 1999, 2002; *Moon et al.*, 2004; *Donelan et al.*, 2012; *Reichl et al.*, 2014).

In most applications, C_d is assumed to be the same in open ocean (deep water) and coastal waters (finite to shallow depth). However, if the wind stress is dependent on sea state, C_d is likely different in shallow water compared to that in deep water, because the wave spectrum is significantly modified by decreasing depth (shoaling). The shoaling wave effects on C_d are normally confined in a relatively narrow coastal region and may not be significant for mesoscale (coarse resolution) model applications. However, they are likely important for high resolution models, such as, storm surge forecasts, wind forecasts

in shallow waters for offshore wind turbines (e.g., *Banta et al.*, 2018), as well as integrated coastal models for waves, currents, and sediment/tracer transports (*Ortiz-Suslow et al.*, 2015). Furthermore, in high wind (tropical cyclone) conditions the shoaling effect can be significant as far as 100km from the coast, as shown later. Previous observations taken at water depths less than 30 m (but outside the surf zone) have shown that the mean (bulk) C_d is typically larger than the C_d parameterizations developed for deep water, as summarized in Fig. 2.1 (e.g., *Geernaert et al.*, 1986; *Smith et al.*, 1992; *Drennan et al.*, 1999; *Oost et al.*, 2002; *Toffoli et al.*, 2012). Recent observations in the surf zone have reported an increased C_d by as much as 100% compared to a deep-water reference C_d at low wind speeds (5–11 m/s) (*Shabani et al.*, 2014; *MacMahan*, 2017). Moreover, a recent numerical study with the Weather Research and Forecasting (WRF) model by *Jiménez and Dudhia* (2018) suggests that an increased roughness length is required in coastal shallow water (30m) to achieve good agreement between modeled and observed winds.

The larger C_d values reported in coastal ocean have often been attributed to shoaling wave effects. The proposed mechanisms can be summarized as follows: 1) reduced wave phase speed (of dominant waves) and hence younger seas (*Johnson and Kofoed-Hansen*, 2000; *Shabani et al.*, 2014); 2) steepening of the dominant waves due to the reduction of wave phase speed and increase of wave amplitude (*Donelan et al.*, 2012); 3) increased wave breaking during shoaling (*Vickers and Mahrt*, 1997; *Makin and Kudryavtsev*, 2002); 4) changing wave shapes during shoaling (*Shabani et al.*, 2014).

Although Fig. 2.1 suggests overall enhancement of C_d in shallow waters, it is difficult to quantify the shoaling effects (increase of C_d from deep water to shallow water as waves shoal) from these results. This is because the observations of deep water C_d vary significantly, likely because of different sea states. If the shallow water results are compared to the *Large and Pond* (1981) parameterization, the shoaling effect is large. However, if they are compared to the COARE3.5 parameterization (*Edson et al.*, 2013), the shoaling effect is quite modest. In fact, based on the HEXMAX data (*Smith et al.*, 1992) *Oost* (1998) originally suggested that shoaling waves increase C_d. However,

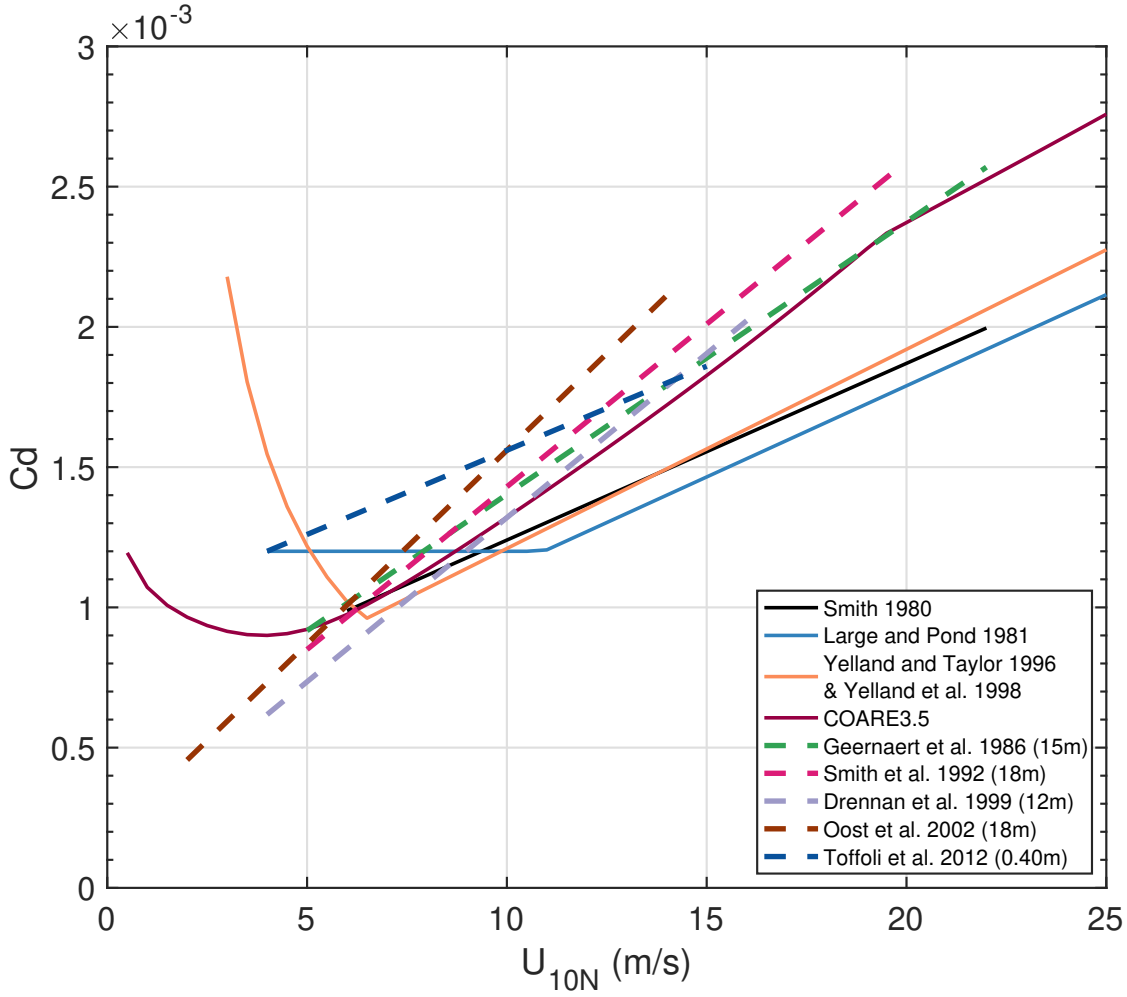

Figure 2.1: C_d–U_{10} relationships from the literature in both open ocean and coastal water or lake. Solid lines: open ocean (deep water) condition; dashed lines: coastal and lake waters with depth less than 30 m.

through rigorous reanalysis, *Oost et al.* (2002) rescinded their previous conclusion and proposed instead that the higher C_d in the HEXMAX data are mainly due to different wave development stages (sea states) between the HEXMAX condition and the referenced open ocean condition. Furthermore, C_d in coastal waters can be affected by processes other than shoaling waves. For example, nonstationary submesoscale motions and the shallow stable internal boundary layer in the atmosphere developed near the coast can also affect the wind stress (*Vickers and Mahrt*, 1999; *Mahrt et al.*, 2016).

To our knowledge, *Anctil and Donelan* (1996) (AD96 hereafter) is the only field study that provided a clear evidence of C_d variation as a result of wave shoaling, since they simultaneously observed C_d at neighboring four towers at different depths, including one in deep water. They observed enhancement of C_d up to 55% due to shoaling relative to C_d at the deep water tower. They also reported that the measured C_d in shallow water was larger by up to 80% relative to the C_d of mature seas in deep water with a Charnock coefficient of 0.011.

Because of these uncertainties, conclusions have not been drawn regarding how much C_d is enhanced by shoaling waves in coastal waters. In addition, the different hypotheses proposed regarding the C_d enhancement due to shoaling waves have not been thoroughly tested. Therefore, numerical studies are needed to isolate the shoaling wave effects from other potential impacts, to quantify the change of C_d relative to a deep water C_d and to examine different causes of C_d variation due to wave shoaling.

This two-part investigation is designed to address the above questions, by simulating shoaling wave spectra using the WAVEWATCH III model and estimating the sea-state dependent wind stress based on the wave spectra, using two different wind stress modeling methods (*Donelan et al.*, 2012; *Reichl et al.*, 2014). In part I, we focus on shoaling wind seas under uniform steady onshore winds. It is a numerical equivalent of the AD96 study, where the cross-shore variation of C_d is estimated from measurements. In Part II, we focus on C_d variation affected by complex shoaling wave fields under landfalling tropical cyclones.

2.2 Method

Reichl et al. (2014) (RHG14 hereafter) investigated the sea-state dependent wind stress in deep water under steady uniform winds and hurricane winds, using two different wind stress models. Here, we extend their study in finite to shallow waters using the same approach.

2.2.1 Shoaling Wave Spectra

2.2.1.a Simulation of Shoaling Wave Spectra with WAVEWATCH III

The WAVEWATCH III (WW3) model (v5.16) predicts wave spectra by solving wave-action equation (*The WAVEWATCH III® Development Group*, 2016). The wind input term (S_{in}) and the white-capping term (S_{dis}) are computed with the *Ardhuin et al.* (2010) physics parameterization (ST4 hereafter). Four-wave interaction (S_{nl}) is computed with the standard discrete interaction approximation. In shallow water, bottom friction (S_{btm}), depth-induced breaking (S_{db}) and triad interaction (S_{tr}) are activated. The wave action equation is solved with these 6 source terms to generate wave spectra during shoaling. Wave simulations are conducted with 40 frequency bins starting at 0.0125 with a logarithmic increment factor of 1.1, and 36 equally spaced directional bins.

This study focuses on medium to high wind speeds above 10 m/s (including hurricane conditions in Part II). Therefore, wind input and white-capping terms are tuned following the ST4 setup in *Liu et al.* (2017), which showed good agreement between model results and observations in Hurricane Ivan. (We have confirmed that using the default WW3 ST4 setup does not significantly change the shoaling wave effects on C_d at wind speeds below gale-force winds.) The bottom dissipation S_{btm} is modelled with a simple linear JONSWAP bottom friction parameterization (*Hasselmann et al.*, 1973). The *Battjes and Janssen* (1978) parameterization is used for depth-induced breaking. Triad interaction is modelled with the Lumped Triad Approximation model (*Eldeberky*, 1996). These three shallow water source terms are used with their default setting.

2.2.1.b Modification of WW3 Shoaling Wave Spectra in High Wavenumber Range

As in RHG14, the wave spectra simulated by the WW3 are not used directly for wind stress calculation because the WW3 does not explicitly resolve high wavenumber/frequency range (the spectrum tail), which is important for the stress calculation. (Although the WW3 internally parameterizes the spectral tail, its level is often significantly higher than observational values.) Previous studies suggest that the directionally integrated wavenumber spectrum in the saturation range (spectral tail) is proportional to the fourth power of the wavenumber so that the saturation spectrum (curvature spectrum) B_{sat} becomes constant. Direct observations of B_{sat} have been scarce and its value is not well constrained, particularly in high wind speeds. Based on the observations by *Romero and Melville* (2010), RHG14 estimated that B_{sat} falls mostly between 0.002 and 0.012, and numerically surveyed the sea-state dependent C_d with three B_{sat} values of 0.002, 0.006, and 0.012. More recently, *Laxague et al.* (2018) showed that the saturation spectral tail level varied over a range of 0.001 to 0.02. This range is slightly wider but is generally consistent with the earlier estimates by RHG14. We therefore follow the same approach as in RHG14 and investigate the sea-state dependent C_d in finite depths with three B_{sat} values of 0.002, 0.006, and 0.012 (Section 3.1). In Section 3.2. and Part II, we will introduce an empirical parametrization of B_{sat}, as explained in Section 3.2.

Although waves in the saturation range do not directly feel the effect of shoaling (C_d at depth less than 2 m is not investigated in this study), the saturation level B_{sat} may still be indirectly modified by shoaling if its level is affected by processes in the dominant wave scale (e.g., through nonlinear wave interactions and through modification of wind forcing). Unfortunately, it is not feasible at present to model the shoaling effect on B_{sat} because of the lack of direct observations. We, therefore, assume that B_{sat} is not affected by shoaling in this study. This is one of the assumptions to be revisited in the future.

Following RHG14, once B_{sat} level is set, it is attached to the resolved part of the WW3 spectrum at three times peak input frequency (f_{pi}), which is estimated from the

equivalent peak frequency of the positive part of the input source term in WW3 (c.f. Eqn. (2.75) in the WW3 manual). Between $1.25f_{pi}$ and $3f_{pi}$, linear transition is applied to smoothly connect the WW3 resolved spectrum and the spectral tail.

2.2.2 Wind Stress Calculation

Once the complete wave spectrum is constructed (from the WW3 resolved spectrum and the parameterized tail), two existing wind stress modeling methods, URI method (*Reichl et al.*, 2014) and Miami method (*Donelan et al.*, 2012), are used to compute the sea-state dependent wind stress using the wave spectra. These two methods were used in *Reichl et al.* (2014) to investigate the sea-state dependent wind stress in deep water. Subsequently, both methods have been implemented into the WW3 model (in version v5.16) as diagnostic flux modules (FLD1/2) and are available for public use (*The WAVEWATCH III® Development Group*, 2016). Since the description of the models is lengthy and is fully presented in *Reichl et al.* (2014), only the model components that are affected by shoaling are presented here.

In both models, wind stress vector $\boldsymbol{\tau}$ is partitioned into two components; the viscous stress vector ($\boldsymbol{\tau}_v$) and the form stress vector ($\boldsymbol{\tau}_f$) at the air-sea interface,

$$\boldsymbol{\tau} = \boldsymbol{\tau}_v + \boldsymbol{\tau}_f. \tag{2.1}$$

The form stress vector is expressed as

$$\boldsymbol{\tau}_f = \int_{k_{min}}^{k_{max}} \int_{-\pi}^{\pi} \frac{\rho_w g \beta_g(k,\theta)\Psi(k,\theta)}{c} d\theta \mathbf{k} dk \tag{2.2}$$

$$c = \sqrt{\frac{g}{k}\tanh kD} = \frac{g}{\sigma}\tanh kD \tag{2.3}$$

where ρ_w is water density, g is gravity, β_g is the wave growth rate, Ψ is the directional wavenumber spectrum, θ is the wave direction, k is the wavenumber, $\mathbf{k}$ is the wavenumber vector, D is water depth, σ is the wave angular frequency, and c is the wave phase speed related to the wavenumber k through the dispersion relation (see Eq. (2.3)). Note that in Eq. (2) of *Reichl et al.* (2014), the factor g/c is replaced by σ (the wave angular frequency)

using the deep water dispersion relation ($\tanh kD = 1$). In shallow water that equation is not valid because the dispersion relation is modified by water depth.

The parameterization of the growth rate β is very different between the two methods. In the Miami method, it is parameterized based on the wind speed as

$$\beta_g(k,\theta) = A_1\sigma\frac{[u_{\lambda/2}\cos(\theta-\theta_w)-c]|u_{\lambda/2}\cos(\theta-\theta_w)-c|}{c^2}\frac{\rho_a}{\rho_w}, \tag{2.4}$$

where A_1 is the empirical coefficient, $u_{\lambda/2}$ is the wind speed at the height of half the wavelength, θ_w is the wind direction, and ρ_a is air density. In the URI method, the growth rate is parameterized based on the wind stress,

$$\beta_g(k,\theta) = c_\beta\sigma\frac{|\boldsymbol{\tau}_t(z=\delta/k)|}{\rho_w c^2}\cos^2(\theta-\theta_\tau), \tag{2.5}$$

where c_β is the empirical coefficient, $\boldsymbol{\tau}_t$ is the turbulent stress vector, δ/k is the inner layer height, and θ_τ is the direction of the turbulent stress.

In addition to this difference in the growth rate parameterizations, the two methods significantly differ in modeling the wave feedback to the mean wind profile. The URI method explicitly models the effect of waves on the mean wind shear (*Hara and Belcher*, 2004). As a result, the wind profile deviates from a logarithmic behavior and the wind direction can change with height. The Miami method, however, assumes a logarithmic wind profile and the wind direction does not vary with height. The wave effect on the wind profile appears only in the modified effective roughness length (*Donelan et al.*, 2012).

The effect of shoaling explicitly appears only in the calculation of the form stress, Eq. (2.2), in both methods. Namely, the impact of shoaling appears in the modification of the wave spectrum Ψ, in the modification of the wave growth rate β_g, as well as in the modification of the wave phase speed c in the denominator. Eqs. (2.2) to (2.5) suggest that the decrease of the phase speed c due to shoaling likely contributes to the increase of the drag coefficient. Using these equations, the impact of shoaling on the form stress and the drag coefficient is discussed in Section 3.3.

We have found that both sea-state dependent stress calculation methods become less reliable when the water depth becomes very shallow, likely because the dominant waves become too short to be accurately simulated in the wave model. Furthermore, attaching the spectral tail becomes difficult in such conditions. Therefore, the stress calculation is terminated at 2 m depth (at a deeper depth in some cases).

2.2.3 Experimental Design

Shoaling experiments of fetch-dependent wind waves are conducted on a sloped bottom under uniform and steady onshore wind. The wind speed spans from 10 m/s to 65 m/s with a 5 m/s increment. The bottom slope is set to 1:100, 1:200, 1:400, 1:1000, and 1:2000. These values are based on the range of bottom slope used in *Irish et al.* (2008) and *Li et al.* (2013). They are representative of realistic bottom slope conditions along the western north Atlantic coast (see Fig. 2.2). The cross-shore domain length, which is also the wind domain length, is set to either 200 km, 400 km or 600 km. This parameter can be interpreted as the storm size or the effective fetch of a moving storm.

Over the sloped bottom, the WW3 spatial resolution in the cross-shore direction is set in such a way that the depth variation between neighboring grids is equal to 2 m. (Our numerical convergence tests have confirmed that the wave fields and the C_d estimates are not materially affected if a higher spatial resolution is used.) The spatial resolution in the alongshore direction is the same as in the cross-shore direction. As a result, the spatial resolution with the steeper slopes is finer than that with the gentler slopes. To balance the requirement of a high spatial resolution and computational efficiency, 1-way nesting is used to connect the higher resolution shoaling region (depth less than 300 m) and the lower resolution deep water region for the cases with 1:100, 1:200, 1:400, and 1:1000 bottom slopes. All shoaling cases are integrated until the wave fields reach the steady state, approximately 3 to 6 hours, depending on the spatial resolution.

For every combination of a particular wind speed and a particular wind domain length, a control deep-water experiment is performed with a uniform depth of 4000 m.

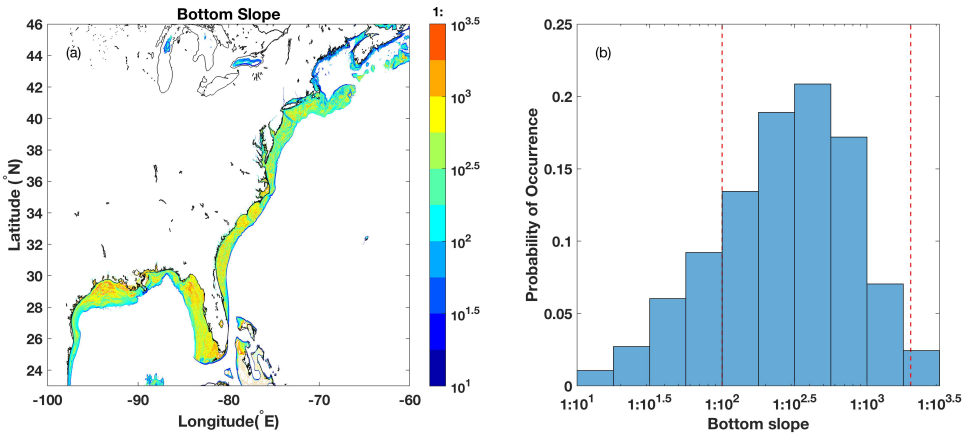

Figure 2.2: Estimates of bottom slope from ETOPO1 Global Relief Model along the western north Atlantic coast for water depth less than 100m. Left: spatial distribution of bottom slope in log scale; Right: probability distribution of bottom slope shown in the left panel. Two red dashed lines denote the range of our experimental slopes. Note that bottom slope is estimated in a 4 by 4 arc minutes grid box using central difference and less than 1:3000 values are excluded.

In the control experiments, fetch-dependent wave spectra and C_d in deep water conditions are obtained in order to isolate the shoaling effects in the sloped bottom experiments.

2.3 Results and Discussion

In this section, the results are presented along the cross-shore transect at the center of the model domain after the wave model integration has reached the steady state.

2.3.1 C_d Results with Different B_{sat} Values

As discussed earlier, the value of the saturation level B_{sat} is not well constrained, particularly at high wind speeds. Therefore, we first investigate the impact of shoaling waves on C_d with three different values of B_{sat} (0.002, 0.006 and 0.012) to cover its likely range, following the approach of RHG14.

2.3.1.a Cross-shore Variations of Wave field and C_d

Figs. 2.3 to 2.5 show cross-shore variations of the significant wave height (H_s), the mean wavelength (L_m) and the drag coefficient (C_d) simulated with three different onshore wind speeds (15, 35, and 65 m/s) and five different bottom slope values ranging from 1:100 to 1:2000. The wind is uniformly applied over the model domain with 200 km cross-shore length. Therefore, the fetch is 200 km at the shoreline and it decreases as the cross-shore distance from the shoreline increases.

Because the water depth is different at a given cross-shore distance depending on the bottom slope, the variations of H_s, L_m, C_d are plotted versus both the cross-shore distance (upper panels) and water depth (lower panels). The results with a larger wind domain length (WDL) of 400 km or 600 km are not shown since they are qualitatively similar.

In the upper panels of Figs. 2.3 to 2.5, the dashed lines show the fetch-dependence of H_s, L_m, and C_d of deep water waves for reference. As expected, both H_s and L_m increase as the fetch increases, particularly at high wind speeds. The value of C_d is less sensitive to the fetch; it slightly increases or decreases with fetch, depending on the B_{sat} value and the wind speed. Because H_s, L_m, and C_d are all fetch-dependent, we should interpret the relative differences between the shoaling impacted values and the deep water values as the true shoaling effect.

As waves enter finite-depth water, the values of H_s and L_m are both reduced relative to those in deep water due to enhanced wave dissipation in all cases (Figs. 3a, 3b, 4a, 4b, 5a, 5b). The values of C_d are also impacted by shoaling and they first increase and then decrease as the cross-shore distance decreases in all cases, regardless of the bottom slope, B_{sat} value, or wind speed (Figs. 3c, 3d, 4c, 4d, 5c, 5d). More pronounced variation of C_d with distance is seen with a steeper bottom slope. The effect of shoaling on C_d is consistent between the two wind stress calculation methods with the URI method showing slightly more variations of C_d than those with the Miami method.

If the results are plotted versus water depth (lower panels), it is clear that the

variations of the wave field (H_s and L_m) and C_d are mainly controlled by the water depth in all cases, although the magnitude of the variation depends on the bottom slope. In all cases, H_s and L_m appear to vary in two stages (Figs. 3e, 3f, 4e, 4f, 5e, 5f); they first decrease slowly (relative to the deep water values) up to a certain threshold depth, likely due to the enhanced bottom dissipation. Once the depth becomes less than the threshold, the dissipation due to depth-induced breaking becomes dominant and H_s and L_m rapidly (and almost linearly) decrease. This threshold depth increases as the wind speed increases.

These two dissipation regimes roughly correspond to the increasing and the decreasing trends of C_d with shoaling, respectively (Figs. 3g, 3h, 4g, 4h, 5g, 5h). The resulting maximum C_d occurs at approximately the same threshold water depth, regardless of the bottom slope, the B_{sat} level, or the method of the stress calculation.

2.3.1.b Shoaling Impact on C_d

To clarify the shoaling impact on C_d, the ratio of the shoaling-impacted C_d (denoted as $C_{d_{sh}}$) to the deep water C_d (denoted as $C_{d_{deep}}$) is presented in Fig. 2.6, with two different bottom slopes (1:100 and 1:2000), three different B_{sat} levels, three different wind speeds, and the two stress calculation methods. The wind domain length is 200 km in all cases as before.

Fig. 2.6 further confirms that:

1. Due to the shoaling wave effect, the drag coefficient C_d always increases (relative to the deep water value) up to a threshold depth, and then decreases once the bottom induced wave breaking becomes effective. This threshold depth increases as the wind speed increases.

2. The shoaling effect on C_d is significantly enhanced when the bottom slope is steeper.

3. The shoaling effect on C_d is more significant with a lower B_{sat} level, particularly at higher wind speeds.

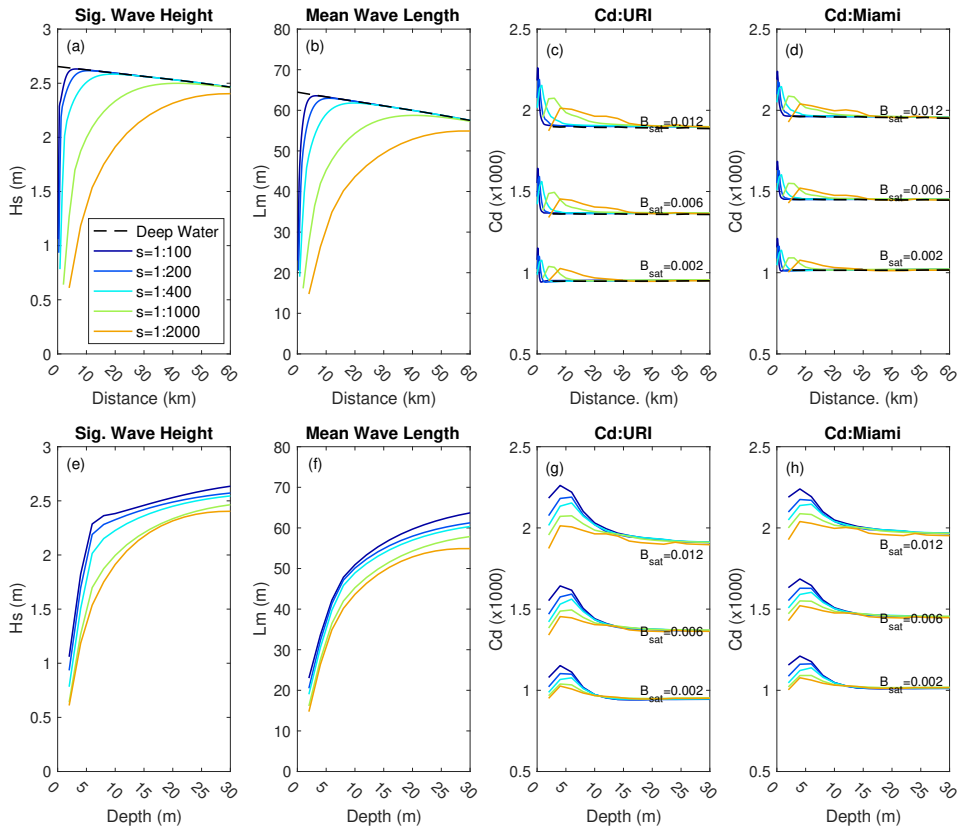

Figure 2.3: Significant wave height (H_s), mean wavelength (L_m) and drag coefficient (C_d) computed using the URI and Miami methods with three B_{sat} levels, simulated under 15 m/s uniform wind on five different bottom slopes. The results are plotted against distance from the shoreline (upper panels) and against water depth (lower panels). In the upper panels dashed line represents fetch-dependent results in the deep water. Lines of different colors represent different bottom slopes as shown in the legend. Cross-shore domain length (fetch at the shoreline) is 200km.

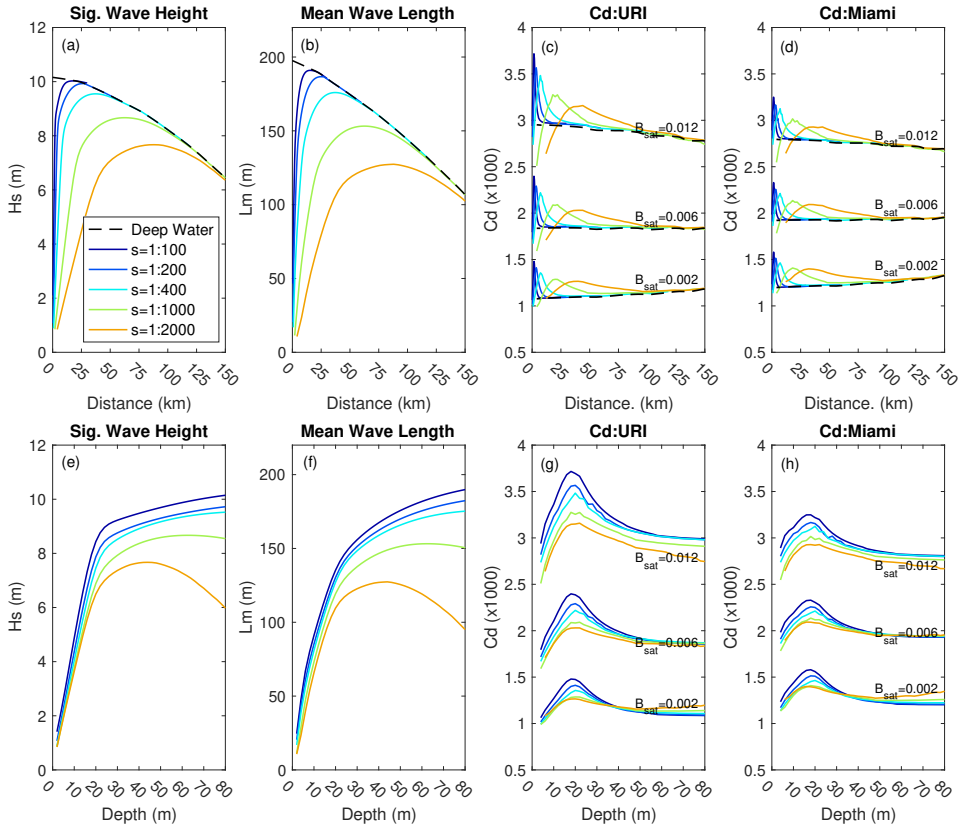

Figure 2.4: Same as Fig. 2.3 but under 35 m/s uniform wind.

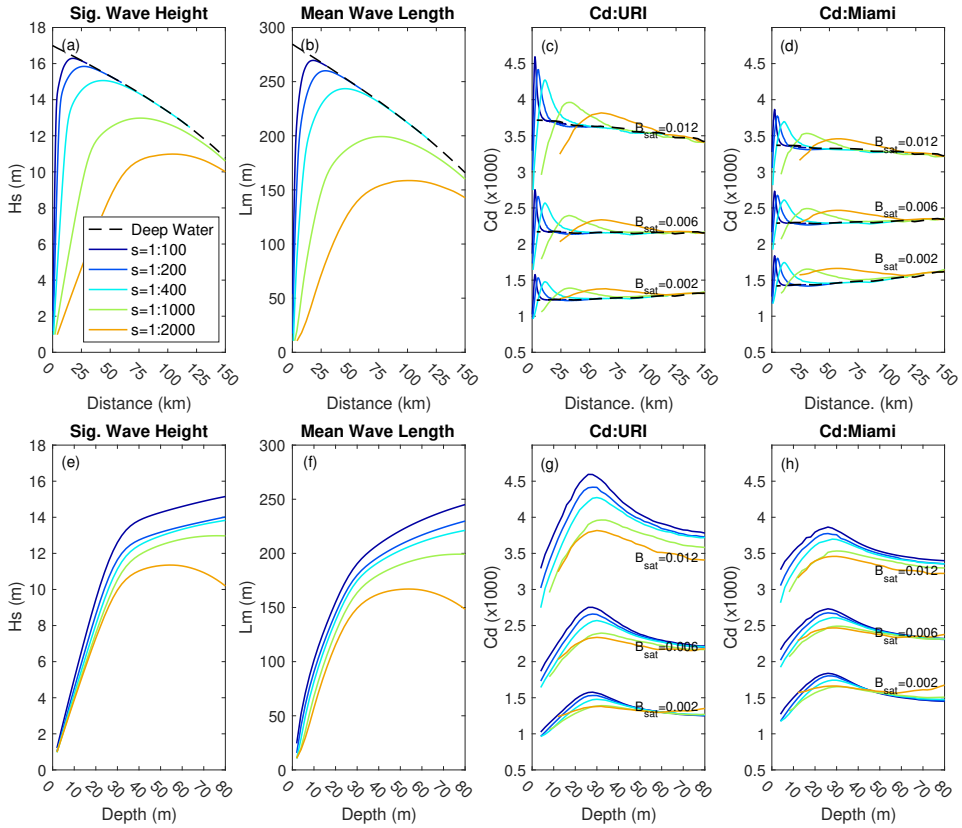

Figure 2.5: Same as Fig. 2.3 but under 65 m/s uniform wind.

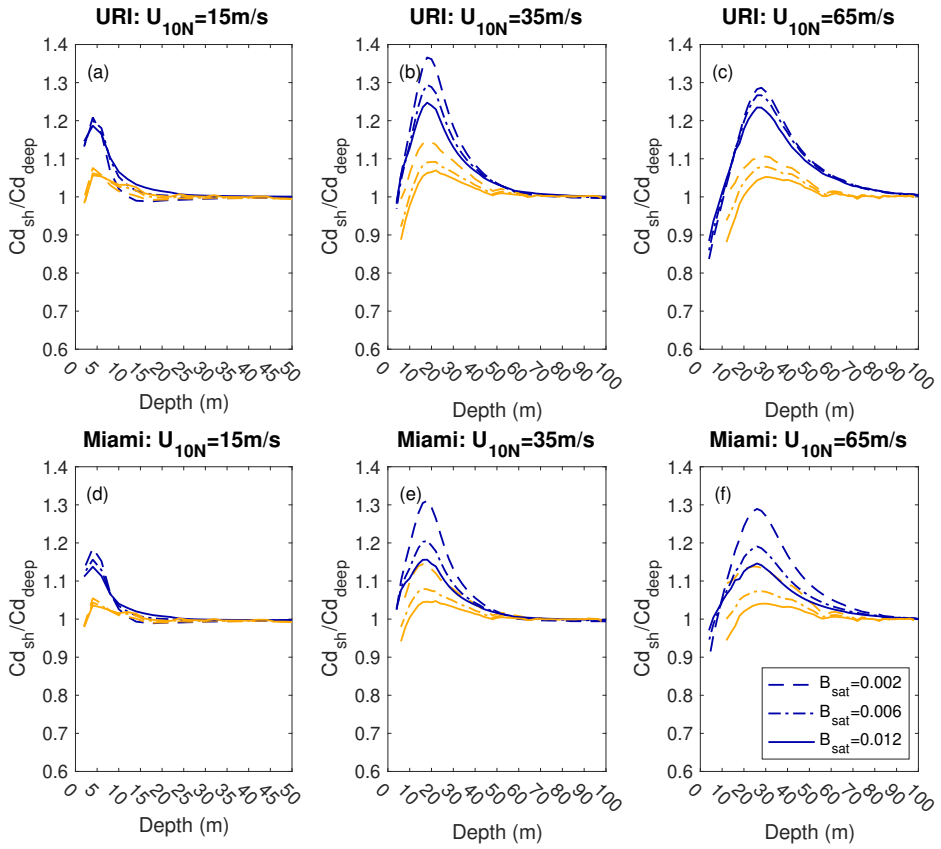

Figure 2.6: Ratio of shoaling impacted C_d ($C_{d_{sh}}$) to deep water C_d ($C_{d_{deep}}$) under 15, 35, and 65 m/s wind speeds. The three B_{sat} levels from low to high are denoted by dash, dash-dot, and solid lines, respectively. Colors indicate bottom slope; blue: 1:100, orange: 1:2000. Upper panels (a-c) show the URI results; lower panels (d-f) show the Miami results.

4. The shoaling effects are qualitatively similar between the URI and Miami methods. The maximum shoaling effect simulated by the URI method displays a -3% to 8% difference from that calculated by the Miami method.

We next focus on the maximum enhancement of C_d due to shoaling. The results are summarized in Fig. 2.7, where the experiments with the larger wind domain lengths of 600 km are also included. For a given tail level B_{sat}, as wind speed increases, the maximum C_d enhancement tends to increase first and then either decreases or saturates depending on the level of B_{sat}. The maximum C_d enhancement decreases with increasing B_{sat} except at the lowest wind speed. The sensitivity of the maximum C_d enhancement to the bottom slope is apparent in all experiments. Larger shoaling wave impacts on C_d are associated with steeper bottom slope values. Overall, the C_d enhancement is within 40%.

The results are qualitatively similar between the URI and Miami methods. Both methods indicate significant C_d enhancement, particularly with higher wind speed and steeper bottom slope. There are some notable differences, however. The maximum C_d enhancement tends to be larger with the URI method and the Miami method shows less sensitivity to the changes of the cross-shore domain length.

2.3.2 C_d Results with Empirical B_{sat}

2.3.2.a Empirical B_{sat} as a Function of Wind Speed

So far, we have examined the shoaling effect on C_d with a range of the saturation level B_{sat}, because this value is not well constrained by existing observations. However, the bulk C_d value is better constrained in low to medium wind speeds (up to about 18 m/s), for example by the COARE 3.5 drag coefficient formulation by *Edson et al.* (2013). It is possible to tune the B_{sat} value (as a function of wind speed) so that the calculated sea-state dependent C_d is roughly consistent with a given C_d formulation on average. At higher wind speeds the drag coefficient is not well constrained. Here we employ the C_d parameterization implemented in the Geophysical Fluid Dynamics Laboratory (GFDL)

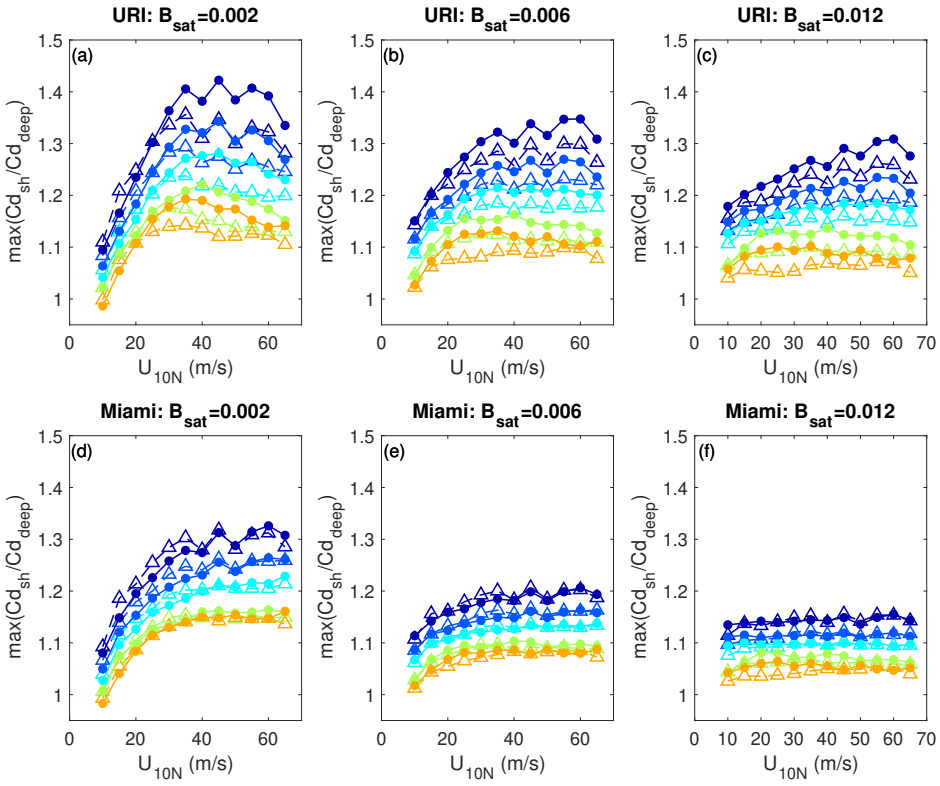

Figure 2.7: Maximum enhancement of drag coefficient as a function of wind speed on different slopes and with two different domain lengths computed with URI (upper) and Miami (lower) methods. Colors represent bottom slopes. Dashed lines with open triangles and solid lines with filled circles indicate the results with the 200 km and 600 km domain lengths, respectively.

hurricane model in 2015 (*Ginis et al.*, 2015, hereafter the GFDL C_d) as a guidance for deriving the empirical B_{sat} to be used in the following analysis. This particular C_d parameterization is chosen because it is close to the COARE 3.5 formulation at lower wind speeds and it also produced the best tropical cyclone intensity forecast using the GFDL hurricane model (*Ginis et al.*, 2015). Note that a similar C_d formulation is used in the current NOAA HWRF hurricane prediction model (*Biswas et al.*, 2018). It is straightforward to carry out the empirical B_{sat} derivation described below using a different drag coefficient formulation if desired (See also Appendix A of Part II).

The empirical B_{sat} is derived by calculating the drag coefficient values with many different (but realistic) wave fields and taking their average. Here, we use complex wave fields under hurricanes to provide a large and non-arbitrary range of wind and wave conditions to define the mean C_d. Specifically, 27 idealized hurricanes with different maximum wind speeds (40 m/s, 55 m/s, 70 m/s), radius of maximum winds (20 km, 40 km, 65 km) and translation speeds (2.5 m/s, 6 m/s, 10 m/s) are used to create wind fields. These hurricane parameters are determined statistically from the Atlantic Hurricane Best Track record (HURDAT2) during 1990–2016 (*Landsea and Franklin*, 2013) with maximum wind speed larger than 33m/s. The hurricane wind fields are created using the *Holland* (1980) parametric model and then applied to the WW3 model until the wave fields become stationary relative to the moving storm. Using the URI and Miami wind stress methods, the sea-state dependent C_d values at each location under the storm (excluding the area of wind speeds less than 10 m/s) are computed from the WW3 wave spectra with an attached spectral tail of 7 different constant B_{sat} levels, from 0.002 to 0.014 with 0.002 increment. The resulting relationship between U_{10} and mean C_d for each B_{sat} level are shown in Fig. 8a. The GFDL C_d is also shown in the same figure. From these data, we can determine the B_{sat} value as a function of wind speed so that the mean C_d becomes equal to the GFDL C_d value. The resulting empirical B_{sat}-U_{10} relation is shown in Fig. 8b. Fig. 8c shows the calculated drag coefficient values and their mean using the empirical B_{sat}-U_{10} relation under all 27 hurricanes. This figure confirms that

the mean of the model estimated sea-state dependent C_d (red cross) is consistent with the GFDL bulk C_d (blue solid line).

Using the deep water fetch-dependent WW3 wave spectra and the empirical B_{sat} the mean square slope can be calculated from the full wave spectrum at different wind speeds. Such results are shown in Fig. 8d. For wind speed below 15 m/s, the mean square slope values compare well with the best fit line of *Cox and Munk* (1954) based on their observations under a comparable wind speed range. No reliable mean square slope observations are available to compare with our estimates at higher wind speeds.

2.3.2.b Shoaling Impact on C_d with Empirical B_{sat}

Using the empirically derived saturation level (B_{sat}) C_d is now recalculated for all shoaling experiments. Figs. 2.9 and 2.10 show C_d and C_d ratio (ratio of shoaling $C_{d_{sh}}$ to deep water $C_{d_{deep}}$), respectively, plotted against water depth for three different wind speeds, two different wind domain lengths, and five different bottom slope values. As wind speed increases, C_d and C_d ratio peak at a deeper water depth. The C_d peak moves to a deeper depth as the cross-shore wind domain length (WDL) increases from 200 km to 600 km in the 35 m/s and 65 m/s cases. This is because the longer WDL increases the fetch for wave growth and hence has the same effect as increasing wind speed. In the 15 m/s case, however, the peak of C_d occurs at a similar depth because waves are approaching the fully grown state with both WDLs. In general, the URI and Miami methods yield enhancement up to 40% and 25%, respectively. The magnitude of enhancement always increases with steeper bottom slope, and it tends to increase with wind speed in both methods.

2.3.2.c C_d–U_{10} Relation Impacted by Shoaling Wind Waves

How is the C_d–U_{10} relationship affected by shoaling wind seas? To answer this question, sea-state dependent C_d values at water depths from 10 m to 50 m are aggregated from all shoaling wind sea experiments conducted at different wind speeds, on different slopes

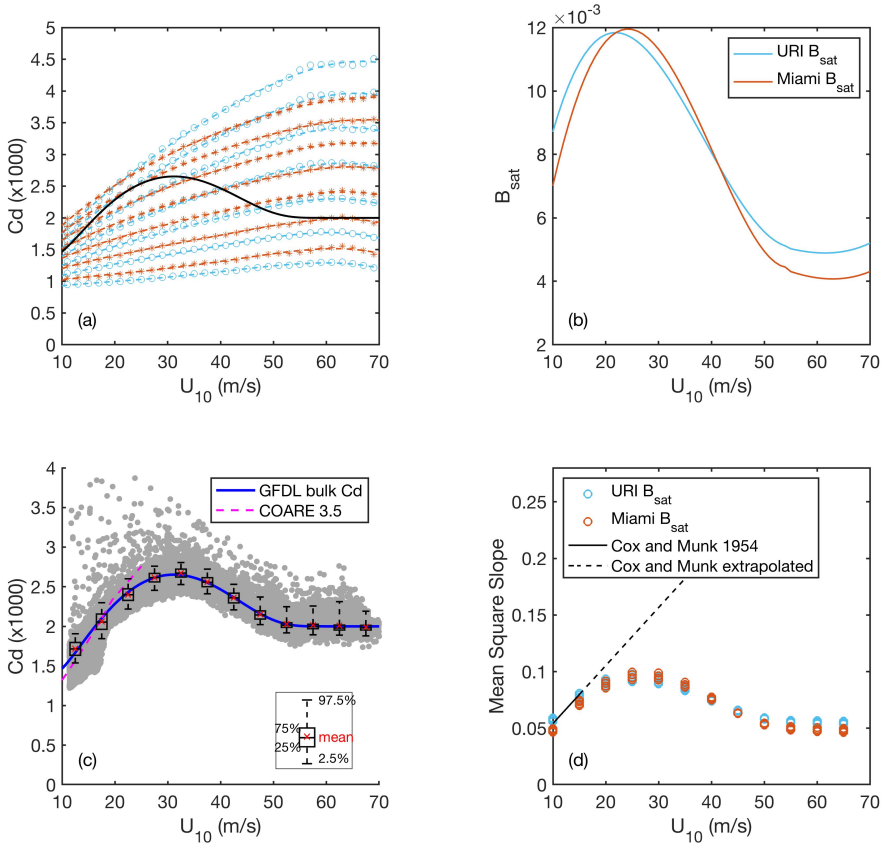

Figure 2.8: a) Mean C_d as a function of U_{10} under 27 idealized hurricanes, calculated with 7 different values of B_{sat} (0.002 to 0.014 with 0.002 increment from bottom up). Black solid line shows GFDL C_d parameterization. b) Empirically derived B_{sat} as a function of U_{10} so that the mean C_d under 27 idealized hurricanes is consistent with GFDL C_d parameterization. c) Calculated C_d, as well as its mean value and variation ranges, as a function of U_{10} using the empirical B_{sat}. Blue line shows GFDL C_d parameterization. d) Calculated mean square slope as a function of U_{10} using the empirical B_{sat}. URI method: light blue; Miami method: orange.

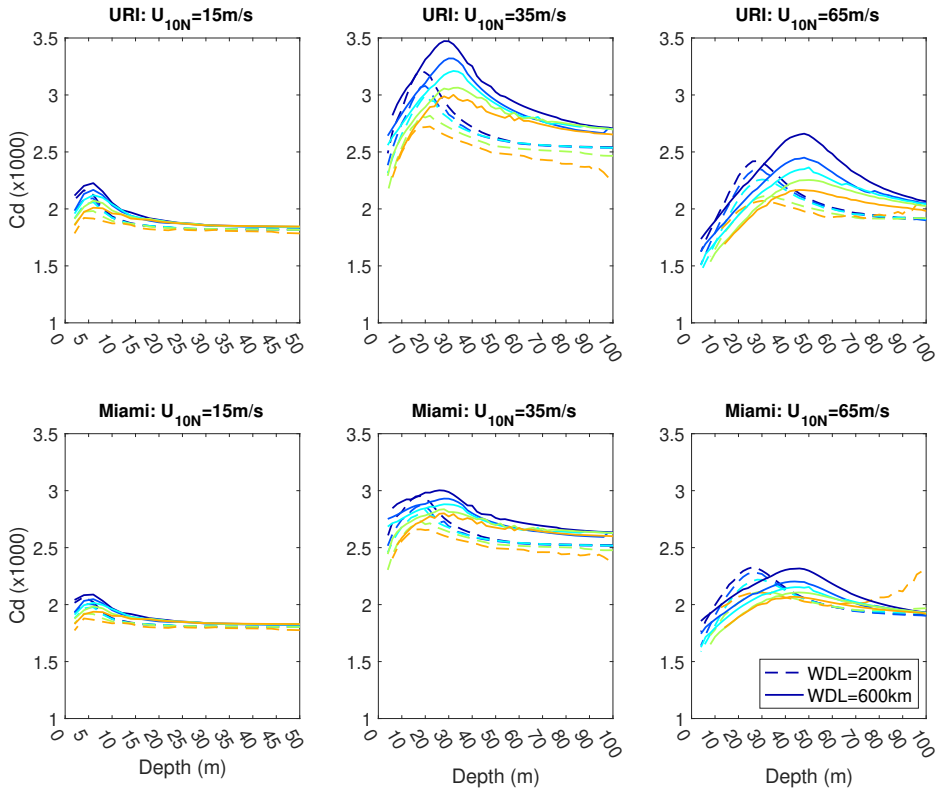

Figure 2.9: Shoaling impacted drag coefficient C_d ($C_{d_{sh}}$) simulated with the empirical B_{sat} as a function of depth under 15, 35, and 65 m/s wind speeds, using URI (top panels) and Miami (bottom panels) methods. Colors represent different bottom slopes as denoted in Fig. 2.1. Dashed and solid lines represent results with the 200 km wind domain length and 600 km wind domain length, respectively.

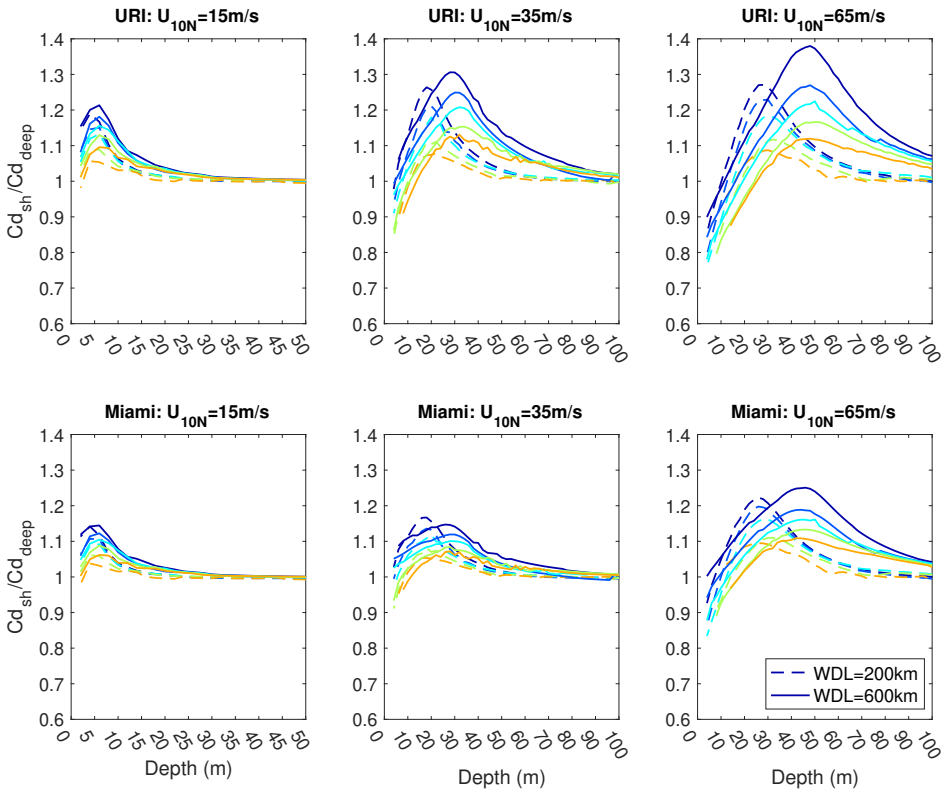

Figure 2.10: Same as Fig. 2.9 but showing the ratio of shoaling impacted C_d to deep water C_d ($C_{d_{sh}}/C_{d_{deep}}$).

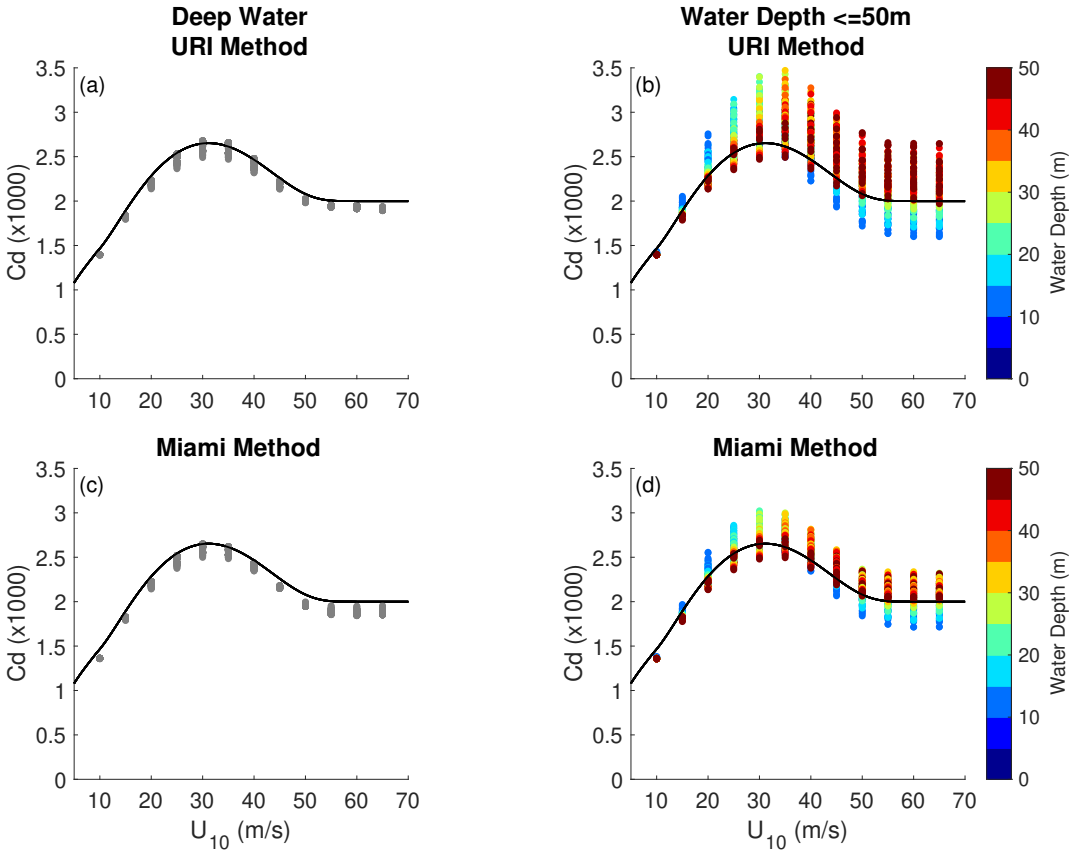

Figure 2.11: Drag coefficient as a function of wind speed in deep water (left panels) and at water depths less than 50 m (right panels). The water depths are color coded. The solid line shows the GFDL C_d bulk parameterization.

and with different cross-shore wind domain lengths. The results are then compared to those in deep water (Fig. 2.11). It is evident that shoaling wind seas significantly increase variability of C_d for a given wind speed in shallow water. This variability is larger using the URI method than using the Miami method. It is interesting to note that at moderate wind speeds (<30 m/s) C_d increases in shallower water (<30 m) while at very high wind speeds (>50m/s) C_d increases in deeper water (>30 m) and decreases in shallower water.

2.3.2.d Depth Range of C_d Enhancement

Fig. 2.12 summarizes the depth ranges in which the significant C_d enhancement (>10%) and the maximum C_d enhancement occurs in all shoaling wave experiments. Results are displayed in dimensional space (depth versus wind speed) and in nondimensional space (relative depth, k_pD, versus wave age, c_p/U_{10}). Here, k_p is the dominant wavenumber at local depth D and c_p is the associated local phase speed. In the dimensional space, the depth ranges of both the maximum and significant C_d enhancement increase with wind speed almost linearly until very high wind speeds. In the nondimensional space, the local relative depth k_pD of the significant C_d enhancement is mainly between 0.5 and 1 and the maximum C_d enhancement occurs roughly in the range of $0.6 < k_pD < 0.9$. It is interesting that the local relative depth k_pD of the maximum C_d enhancement gradually decreases as the local wave age c_p/U_{10} increases, for which there are no obvious explanations.

Our model results can be further compared to AD96 results using the nondimensional parameters. In AD96, the drag coefficients were simultaneously observed at three towers at different depths: Towers 1 (D∼3m), 2 (D∼5m) and 4 (D∼13m). Three observational cases (circles, diamonds, squares in Fig. 2.12) with wind speeds 13–15 m/s were obtained from the tower array. In all three cases, shoaling effects on the C_d were clearly present. Consistently, the C_d observed at Tower 4 were the lowest and were likely close to the deep water values (since the normalized depth k_pD was larger than 1.1), the C_d at Tower 2 were the highest, the C_d at Tower 1 were in between (c.f. AD96 Figure 7a).

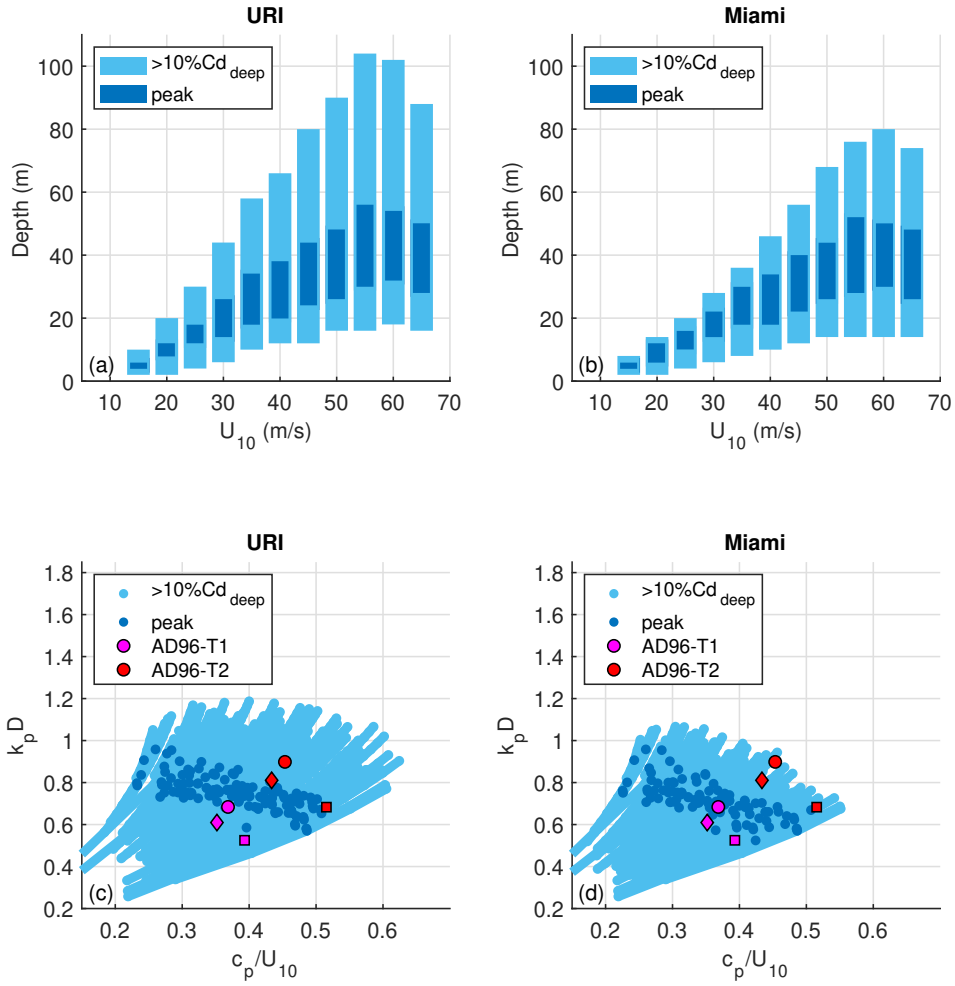

Figure 2.12: Top panels: depth range of significant (>10%) (light blue) and maximum (dark blue) enhancement of C_d, as a function of wind speed. Bottom panels: normalized depth (k_pD) of significant (>10%) (light blue) and maximum (dark blue) enhancement of C_d, as a function of wave age (c_p/U_{10}). The magenta and red data points are from *Anctil and Donelan* (1996) (AD96). The magenta points are from Tower-1 (∼3m), the red points are from Tower-2 (∼5m). These data points denoted by circle, diamond, and square are from 3 observational cases. The maximum C_d was always observed at Tower-2.

Hence, only the local wave age and the relative depth at Towers 1 and 2 (computed from tabulated data in AD96) are marked in Figs. 12c and 12d. The same nondimensional parameters are computed from our modeling data (light and dark blue data points in Figs. 12c and 12d). It can be seen that the relative depth of the increased C_d in AD96 is generally consistent with our model results. Note that the AD96 experiments were conducted in a lake environment with a relatively steep bottom slope estimated to be about 1:100. Interestingly, AD96 also reported that the surface elevation started to decrease rapidly near Tower 2 where the apparent maximum C_d occurred. This finding is qualitatively consistent with our results shown in Figs. 2.3 to 2.5.

2.3.3 Causes of Shoaling-induced C_d Enhancement and its Dependence on Bottom Slope

2.3.3.a Why do Shoaling Wind Waves Increase Drag Coefficient?

In this study the wave form stress integration is performed in the wavenumber space as explained in Section 2.3. However, since a shoaling wave packet of a single frequency/wavenumber preserves its frequency but its wavenumber changes, it is easier to consider the shoaling impact using the frequency spectrum. Furthermore, the form drag is often associated with wave steepness instead of wave height. Therefore, we investigate how the form stress changes as the frequency slope spectrum is modified by shoaling.

Let us first rewrite Eq. (2.2) in terms of the directional frequency spectrum $\Psi(\sigma,\theta)$,

$$\boldsymbol{\tau}_f = \int_{\sigma_{min}}^{\sigma_{max}} \int_{-\pi}^{\pi} \frac{\rho_w g \beta_g(\sigma,\theta)\Psi(\sigma,\theta)}{c} \frac{\mathbf{k}}{k} d\theta d\sigma. \tag{2.6}$$

With the Miami method, Eqs. (2.6) and (2.4) can be combined to yield

$$\boldsymbol{\tau}_f = \int_{\sigma_{min}}^{\sigma_{max}} \int_{-\pi}^{\pi} \rho_a g A_1 [u_{\lambda/2}\cos(\theta-\theta_w) - c]|u_{\lambda/2}\cos(\theta-\theta_w) - c| \frac{S(\sigma,\theta)}{c\sigma} \frac{\mathbf{k}}{k} d\theta d\sigma. \tag{2.7}$$

while with the URI method, Eqs. (2.6) and (2.5) can be combined to yield

$$\boldsymbol{\tau}_f = \int_{\sigma_{min}}^{\sigma_{max}} \int_{-\pi}^{\pi} g c_\beta |\boldsymbol{\tau}_t(z=\delta/k)| \cos^2(\theta-\theta_\tau) \frac{S(\sigma,\theta)}{c\sigma} \frac{\mathbf{k}}{k} d\theta d\sigma. \tag{2.8}$$

Here, $S(\sigma,\theta) = k^2\Psi(\sigma,\theta)$ is the directional frequency wave slope spectrum. Eqs. (2.7) and (2.8) suggest that, with both methods, the form stress for a given wind forcing is roughly determined by the integration of $S(\sigma)/c\sigma$, where $S(\sigma)$ is the directionally integrated slope spectrum, if the directional spreading of the wave energy is small and wind and waves are mostly aligned (as in our shoaling experiments under uniform onshore wind). Then, the effect of shoaling on the form stress appears in two ways, that is, the shoaling modification of the slope spectrum $S(\sigma)$ (increasing/decreasing steepness of waves) and the decrease of c due to shoaling (slowing down of waves).

Two additional experiments are hence designed to probe the effects of these two shoaling effects. In Exp A, the slope spectrum S is modified by shoaling but the phase speed c is kept as in deep water. In Exp B, both S and c are modified by shoaling. These experiments are conducted with a shoaling wind wave spectrum on a 1:200 sloped bottom at 35m/s onshore wind with the wind domain length of 200km.

In Fig. 2.13, the shoaling evolution of the frequency slope spectrum $S(\sigma)$ is shown at different depths. It is evident that the steepness of the dominant waves (that is, the slope spectrum integrated over the dominant frequency band) increases with shoaling and peaks around 20–30m water depth, and then rapidly decreases. The results of Exp A in Fig. 2.14 show that the C_d is enhanced due to this wave steepening (increase of the slope spectrum). However, the total enhancement (Exp B) is significantly larger than the enhancement of the slope spectrum alone (Exp A). This suggests that slowing down of waves (decrease of c) also makes a significant contribution to the C_d enhancement. Once waves are in the surf zone and the slope spectrum rapidly decreases due to depth-induced breaking, C_d also decreases even if c continues to decrease.

As discussed in Section 1, past literature suggests that the drag coefficient is enhanced in shallow water because: 1) reduced wave phase speed (of dominant waves) and hence younger seas; 2) reduced dominant wave phase speed combined with an increased wave amplitude (or steepening of the dominant waves); 3) increased wave breaking during shoaling; 4) different wave shapes during shoaling. Our model results are consistent with

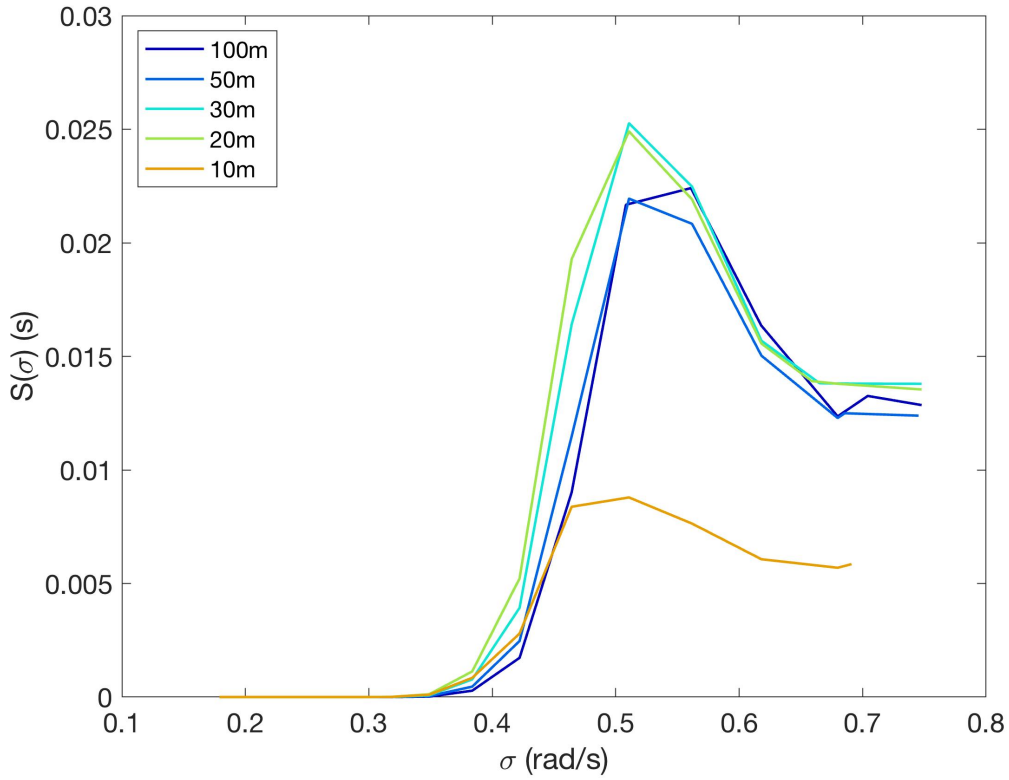

Figure 2.13: Frequency slope spectrum $S(\sigma)$ at different depths. Wind speed is 35m/s, wind domain length is 200km, bottom slope is 1:200.

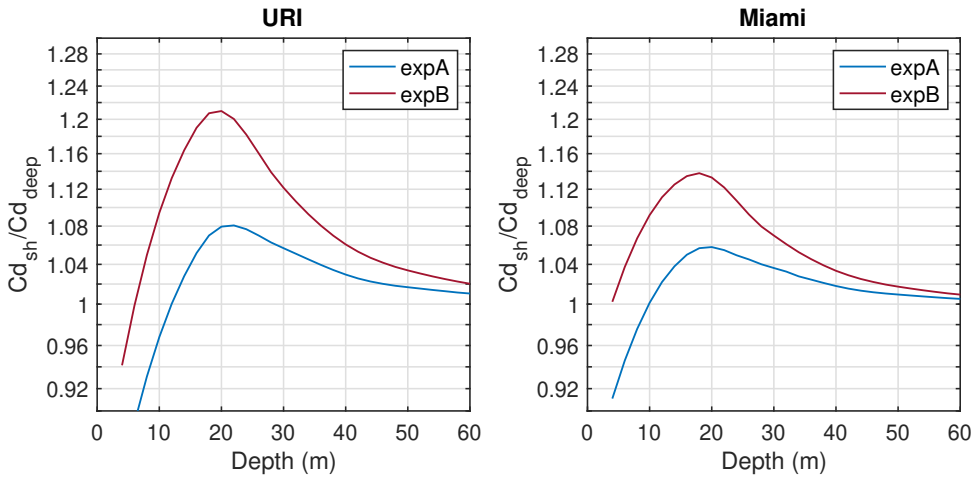

Figure 2.14: Ratio of $C_{d_{sh}}$ to $C_{d_{deep}}$. Exp A: only slope spectrum $S(\sigma)$ is modified by shoaling. Exp B: both slope spectrum $S(\sigma)$ and wave phase speed, c, are modified by shoaling. Wind speed is 35m/s, wind domain length is 200km, bottom slope is 1:200. The vertical axis is in a log scale.

both 1) and 2). Since our wind stress model uses the same wave growth rate parameterization in deep water and in shallow water, the effects of increased wave breaking and the different wave shape are not explicitly included in our results. Therefore, we cannot assess the validity of 3) and 4) in this study.

2.3.3.b Effects of Bottom Slope

One of the most interesting findings in this study is the strong dependence of the C_d enhancement on the bottom slope. To explain this, we show the variation of the significant wave height H_s, mean wave length L_m, and drag coefficient C_d, relative to their deep water values in Fig. 2.15 for two different bottom slopes of 1:200 and 1:2000, with wind speed 35m/s and the wind domain length 200km. With a gentler slope of 1:2000, both H_s and L_m decrease much faster as depth decreases until the depth-induced breaking starts to dominate. This is likely because with a gentler slope dominant waves travel over a longer distance in shallow water and the bottom dissipation is more effective in suppressing the dominant wave energy. Since the dominant wave length is shorter and

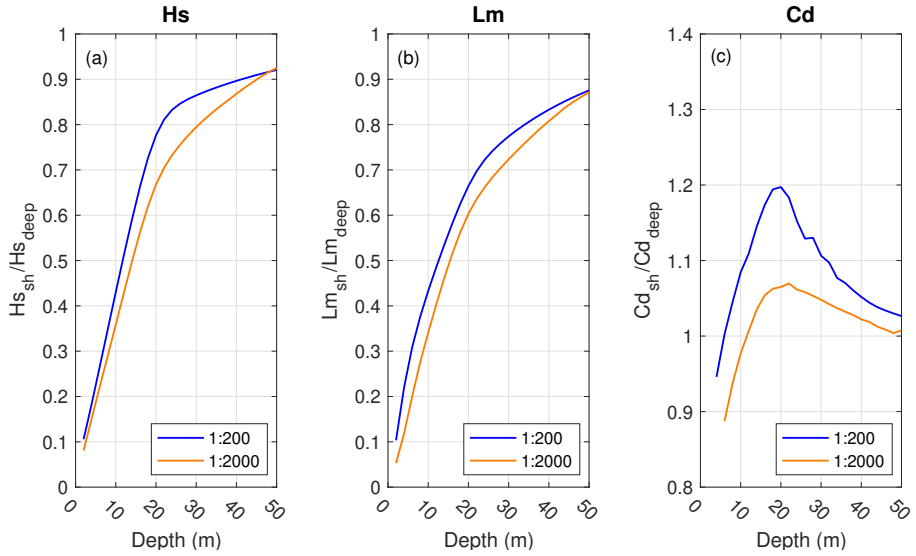

Figure 2.15: Ratio of shoaling impacted H_s, L_m, C_d (using the URI method) to those in deep water. Colors indicate bottom slope; blue: 1:200, orange: 1:2000. Wind speed is 35m/s, wind domain length is 200km.

the wave amplitude is smaller, the drag coefficient is also smaller with a gentler slope at a given depth as seen in Fig. 2.15c.

We have made attempts to validate our finding of the bottom slope effect against available observations in the literature by sorting the reported C_d measurements in shallow water according to bathymetry gradient at the observational sites. However, we were unable to find any clear evidence of the bottom slope effect, likely because the observed C_d values are affected by multiple factors, not just the bottom slope. Well-designed field campaigns or laboratory experiments may be needed to verify this sensitivity to the bottom slope.

2.4 Concluding Remarks

In this study, two wave spectrum-based wind stress calculation methods (Miami and URI) are used to model the cross-shore variation of the drag coefficient under the influence of shoaling idealized wind seas. Our results show that the drag coefficient always increases with shoaling and peaks at a threshold depth, and then rapidly decreases, relative to

its fetch-dependent deep water value. The threshold depth is where the depth-induced wave breaking starts to dominate the dissipation. This variation of C_d is qualitatively consistent with the observational study of *Anctil and Donelan* (1996). The relative C_d enhancement is within 25% with the Miami method and 40% with the URI method.

The enhancement of C_d is sensitive to the bottom slope, with a larger increase on a steeper bottom slope. This implies that the bottom slope needs to be considered as an important parameter in addition to water depth in the future use of drag coefficient in coastal waters.

Our results suggest a larger variability of the C_d–U_{10} bulk relation in shallow water compared to that in deep water. Specifically, at moderate wind speeds (<30m/s), shoaling wind seas can increase the slope of the C_d–U_{10} linear fit for water depth between 15m and 30m. This is qualitatively consistent with existing measurements in coastal waters. Our analysis indicates that the increase of C_d is mainly caused by a combination of wave steepening (increase of the slope spectrum) and decrease of the wave phase speed.

Two strong assumptions have been made in this study. First, we have not included the effect of enhanced wave breaking of shoaling waves on the wave form drag. Although the growth rate parameterizations used in our study have been tuned to open ocean observations and therefore implicitly include breaking wave impacts in deep water conditions, they have not been modified in shallow water.

Since the slope spectrum increases due to shoaling, the form drag of waves increases partially due to wave steepening in this study. However, it is possible that the wave growth rate parameterization also needs to be enhanced, as suggested by *Babanin et al.* (2007). However, the effects of wave breaking and resulting airflow separation on the wave growth rate and form drag are not fully understood. Some studies reported enhancement of form drag by incipient and/or actively breaking waves (e.g., *Banner*, 1990; *Babanin et al.*, 2007; *Sullivan et al.*, 2018). *Babanin et al.* (2007) suggested that the growth rate should be enhanced to model the observed enhancement. However, *Husain et al.* (2019) found that the wave growth rate actually decreases with wave steepness under strong

wind forcing. This result is consistent with previous studies from the field (*Donelan et al.*, 2006) and in the laboratory (*Peirson and Garcia*, 2008). In fact, *Donelan et al.* (2004) suggested that frequent wave breaking and/or airflow separation may cause the observed C_d saturation at very high winds. Because of this uncertainty, we have chosen not to include any explicit shallow water breaking effects, such as modifications of the growth rate parameterization in shallow water (other than the changes in the wave dispersion relationship).

Second, we have assumed that the empirical B_{sat} is a function of the wind speed alone and is not affected by shoaling, again due to observational uncertainties of B_{sat} in shallow water. Validity of these two assumptions (particularly in the surf zone) need to be revisited in the future studies.

Although questions remain regarding some assumptions made in our model approach, our numerical results strongly suggest that the drag coefficient in coastal water (outside the inner surf zone) can increase by shoaling wind seas and hence can be different from that in the open ocean. Our finding is further strengthened because two very different sea-state dependent wind stress models (URI and Miami) yield generally consistent results. Our results here can be valuable for high resolution nearshore modeling applications (e.g., nearshore wind forecasts, storm surge modeling), as well as coastal modeling in high wind conditions. For such applications, incorporating the shoaling wave impact on C_d may improve model performances under onshore wind conditions.

REFERENCES

Anctil, F., and M. A. Donelan (1996), Air-water momentum flux observations over shoaling waves, *Journal of Physical Oceanography*, *26*(7), 1344–1353, doi:10.1175/1520-0485(1996)026<1344:AMFOOS>2.0.CO;2.

Ardhuin, F., et al. (2010), Semiempirical dissipation source functions for ocean waves. Part I: Definition, calibration, and validation, *Journal of Physical Oceanography*, *40*(9), 1917–1941, doi:10.1175/2010JPO4324.1.

Babanin, A. V., M. L. Banner, I. R. Young, and M. A. Donelan (2007), Wave-follower field measurements of the wind-input spectral function. Part III: Parameterization of the wind-input enhancement due to wave breaking, *Journal of Physical Oceanography*, *37*(11), 2764–2775, doi:10.1175/2007JPO3757.1.

Banner, M. L. (1990), The influence of wave breaking on the surface pressure distribution in wind-wave interactions, *Journal of Fluid Mechanics*, *211*(463), 463–495, doi:10.1017/S0022112090001653.

Banta, R. M., et al. (2018), Evaluating and improving nwp forecast models for the future: How the needs of offshore wind energy can point the way, *Bulletin of the American Meteorological Society*, *99*(6), 1155–1176, doi:10.1175/BAMS-D-16-0310.1.

Battjes, J. A., and J. Janssen (1978), Energy loss and set-up due to breaking of random waves, in *Coastal Engineering 1978*, pp. 569–587.

Biswas, M. K., et al. (2018), Hurricane Weather Research and Forecasting (HWRF) Model: 2018 Scientific Documentation, *Tech. Rep. November*.

Cox, C., and W. Munk (1954), Measurement of the Roughness of the Sea Surface from Photographs of the Sun's Glitter, *Journal of the Optical Society of America*, *44*(11), 838, doi:10.1364/josa.44.000838.

Donelan, M. A., F. W. Dobson, S. D. Smith, and R. J. Anderson (1993), On the dependence of sea surface roughness on wave development, *Journal of Physical Oceanography*, *23*(9), 2143–2149, doi:10.1175/1520-0485(1993)023<2143:OTDOSS>2.0.CO;2.

Donelan, M. A., W. M. Drennan, and K. B. Katsaros (1997), The air-sea momentum flux in conditions of wind sea and swell, *Tech. Rep. 10*, doi:10.1175/1520-0485(1997)027<2087:TASMFI>2.0.CO;2.

Donelan, M. A., B. K. Haus, N. Reul, W. J. Plant, M. Stiassnie, H. C. Graber, O. B. Brown, and E. S. Saltzman (2004), On the limiting aerodynamic roughness of the ocean in very strong winds, *Geophysical Research Letters*, *31*(18), L18,306, doi:10.1029/2004GL019460.

Donelan, M. A., A. V. Babanin, I. R. Young, and M. L. Banner (2006), Wave-follower field measurements of the wind-input spectral function. Part II: Parameterization of the wind input, *Journal of Physical Oceanography*, *36*(8), 1672–1689, doi:10.1175/JPO2933.1.

Donelan, M. A., M. Curcic, S. S. Chen, and A. K. Magnusson (2012), Modeling waves and wind stress, *Journal of Geophysical Research: Oceans*, *117*(7), doi:10.1029/2011JC007787.

Drennan, W. M., K. K. Kahma, and M. A. Donelan (1999), On momentum flux and velocity spectra over waves, *Boundary-Layer Meteorology*, *92*(3), 489–515, doi:10.1023/A:1002054820455.

Drennan, W. M., P. K. Taylor, and M. J. Yelland (2005), Parameterizing the sea surface roughness, *Journal of Physical Oceanography*, *35*(5), 835–848, doi:10.1175/JPO2704.1.

Edson, J. B., et al. (2013), On the exchange of momentum over the open ocean, *Journal of Physical Oceanography*, *43*(8), 1589–1610, doi:10.1175/JPO-D-12-0173.1.

Eldeberky, Y. (1996), Nonlinear transformations ofwave spectra in the nearshore zone,

Ph.D. thesis, Fac. of Civil Engineering and Geosciences, Delft University of Technology, The Netherlands.

Geernaert, G. L., K. B. Katsaros, and K. Richter (1986), Variation of the drag coefficient and its dependence on sea state, *Journal of Geophysical Research*, *91*(C6), 7667, doi: 10.1029/jc091ic06p07667.

Ginis, I., M. Bender, B. Thomas, M. Morin, V. Tallapragada, and A. Soloviev (2015), A new drag coefficient formulation and its impact on the gfdl and hwrf hurricane model predictions, 19th Conference on Air-Sea Interaction, Phoenix, AZ, January 4-8.

Hara, T., and S. E. Belcher (2004), Wind profile and drag coefficient over mature ocean surface wave spectra, *Journal of Physical Oceanography*, *34*(11), 2345–2358, doi:10.1175/JPO2633.1.

Hasselmann, K., et al. (1973), Measurements of wind-wave growth and swell decay during the joint North Sea wave project (JONSWAP)., *Erganzungsheft zur Deutschen Hydrographischen Zeitschrift*, *12*(8).

Holland, G. J. (1980), An analytic model of the wind and pressure profiles in hurricanes., *Monthly Weather Review*, *108*(8), 1212–1218, doi:10.1175/1520-0493(1980)108<1212:AAMOTW>2.0.CO;2.

Husain, N. T., T. Hara, M. P. Buckley, K. Yousefi, F. Veron, and P. P. Sullivan (2019), Boundary layer turbulence over surface waves in a strongly forced condition: LES and observation, *Journal of Physical Oceanography*, *49*(8), 1997–2015, doi:10.1175/JPO-D-19-0070.1.

Irish, J. L., D. T. Resio, and J. J. Ratcliff (2008), The influence of storm size on hurricane surge, *Journal of Physical Oceanography*, *38*(9), 2003–2013, doi: 10.1175/2008JPO3727.1.

Janssen, J. (1997), Does wind stress depend on sea-state or not? A statistical error analysis of HEXMAX data, *Tech. Rep. 3*, doi:10.1023/A:1000336814021.

Janssen, P. A. E. M. (1989), Wave-Induced Stress and the Drag of Air Flow over Sea Waves, *Journal of Physical Oceanography*, *19*(6), 745–754, doi:10.1175/1520-0485(1989)019<0745:wisatd>2.0.co;2.

Jiménez, P. A., and J. Dudhia (2018), On the need to modify the sea surface roughness formulation over shallow waters, *Journal of Applied Meteorology and Climatology*, *57*(5), 1101–1110, doi:10.1175/JAMC-D-17-0137.1.

Johnson, H. K., and H. Kofoed-Hansen (2000), Influence of bottom friction on sea surface roughness and its impact on shallow water wind wave modeling, *Journal of Physical Oceanography*, *30*(7), 1743–1756, doi:10.1175/1520-0485(2000)030<1743:IOBFOS>2.0.CO;2.

Landsea, C. W., and J. L. Franklin (2013), Atlantic hurricane database uncertainty and presentation of a new database format, *Monthly Weather Review*, *141*(10), 3576–3592, doi:10.1175/MWR-D-12-00254.1.

Large, W. G., and S. Pond (1981), Open ocean momentum flux measurements in moderate to strong winds., *J. Phys. Oceanogr.*, *11*(3 , Mar. 1981), 324–336, doi:10.1175/1520-0485(1981)011<0324:oomfmi>2.0.co;2.

Laxague, N. J., C. J. Zappa, D. A. LeBel, and M. L. Banner (2018), Spectral Characteristics of Gravity-Capillary Waves, With Connections to Wave Growth and Microbreaking, *Journal of Geophysical Research: Oceans*, *123*(7), 4576–4592, doi:10.1029/2018JC013859.

Li, R., L. Xie, B. Liu, and C. Guan (2013), On the sensitivity of hurricane storm surge simulation to domain size, *Ocean Modelling*, *67*, 1–12, doi:10.1016/j.ocemod.2013.03.005.

Liu, Q., A. Babanin, Y. Fan, S. Zieger, C. Guan, and I. J. Moon (2017), Numerical simulations of ocean surface waves under hurricane conditions: Assessment of existing model performance, *Ocean Modelling*, *118*, 73–93, doi:10.1016/j.ocemod.2017.08.005.

MacMahan, J. (2017), Increased aerodynamic roughness owing to surfzone foam, *Journal of Physical Oceanography*, *47*(8), 2115–2122, doi:10.1175/JPO-D-17-0054.1.

Mahrt, L., E. L. Andreas, J. B. Edson, D. Vickers, J. Sun, and E. G. Patton (2016), Coastal zone surface stress with stable stratification, *Journal of Physical Oceanography*, *46*(1), 95–105, doi:10.1175/JPO-D-15-0116.1.

Makin, V. K., and V. N. Kudryavtsev (1999), Coupled sea surface-atmosphere model: 1. Wind over waves coupling, *Journal of Geophysical Research: Oceans*, *104*(C4), 7613–7623, doi:10.1029/1999jc900006.

Makin, V. K., and V. N. Kudryavtsev (2002), Impact of dominant waves on sea drag, *Boundary-Layer Meteorology*, *103*(1), 83–99, doi:10.1023/A:1014591222717.

Moon, I. J., T. Hara, I. Ginis, S. E. Belcher, and H. L. Tolman (2004), Effect of surface waves on air-sea momentum exchange: Part I: Effect of mature and growing seas, *Journal of the Atmospheric Sciences*, *61*(19), 2321–2333, doi:10.1175/1520-0469(2004)061<2321:EOSWOA>2.0.CO;2.

Oost, W. A. (1998), The KNMI HEXMAX stress data - a reanalysis, *Tech. Rep. 3*, doi:10.1023/A:1000824918910.

Oost, W. A., G. J. Komen, C. M. Jacobs, and C. Van Oort (2002), New evidence for a relation between wind stress and wave age from measurements during ASGAMAGE, *Boundary-Layer Meteorology*, *103*(3), 409–438, doi:10.1023/A:1014913624535.

Ortiz-Suslow, D. G., B. K. Haus, N. J. Williams, N. J. Laxague, A. J. Reniers, and H. C. Graber (2015), The spatial-temporal variability of air-sea momentum fluxes observed at a tidal inlet, *Journal of Geophysical Research: Oceans*, *120*(2), 660–676, doi:10.1002/2014JC010412.

Peirson, W. I., and A. W. Garcia (2008), On the wind-induced growth of slow water waves of finite steepness, *Journal of Fluid Mechanics*, *608*, 243–274, doi:10.1017/S002211200800205X.

Reichl, B. G., T. Hara, and I. Ginis (2014), Sea state dependence of the wind stress over the ocean under hurricane winds, *Journal of Geophysical Research: Oceans*, *119*(1), 30–51, doi:10.1002/2013JC009289.

Romero, L., and W. K. Melville (2010), Airborne observations of fetch-limited waves in the gulf of tehuantepec, *Journal of Physical Oceanography*, *40*(3), 441–465, doi: 10.1175/2009JPO4127.1.

Shabani, B., P. Nielsen, and T. Baldock (2014), Direct measurements of wind stress over the surf zone, *Journal of Geophysical Research: Oceans*, *119*(5), 2949–2973, doi: 10.1002/2013JC009585.

Smith, S. D., et al. (1992), Sea surface wind stress and drag coefficients: The hexos results, *Boundary-Layer Meteorology*, *60*(1-2), 109–142, doi:10.1007/BF00122064.

Sullivan, P. P., M. L. Banner, R. P. Morison, and W. L. Peirson (2018), Turbulent flow over steep steady and unsteady waves under strong wind forcing, *Journal of Physical Oceanography*, *48*(1), 3–27, doi:10.1175/JPO-D-17-0118.1.

The WAVEWATCH III ® Development Group (2016), User manual and system documentation of WAVEWATCH III ® version 5.16, *Tech. Note 329*, NOAA/NWS/NCEP/MMAB, College Park, MD, USA, 326 pp. + Appendices.

Toffoli, A., L. Loffredo, P. Le Roy, J. M. Lefèvre, and A. V. Babanin (2012), On the variability of sea drag in finite water depth, *Journal of Geophysical Research: Oceans*, *117*(7), n/a–n/a, doi:10.1029/2011JC007857.

Vickers, D., and L. Mahrt (1997), Fetch limited drag coefficients, *Tech. Rep. 1*, doi: 10.1023/A:1000472623187.

Vickers, D., and L. Mahrt (1999), Observations of non-dimensional wind shear in the coastal zone, *Quarterly Journal of the Royal Meteorological Society*, *125*(559), 2685–2702, doi:10.1002/qj.49712555917.

MANUSCRIPT 3

Impact of Shoaling Ocean Surface Waves on Wind Stress and Drag Coefficient in Coastal Waters: Part II Tropical Cyclones

Xuanyu Chen[1*], Isaac Ginis[1], and Tetsu Hara[1]

Published in Journal of Geophysical Research: Oceans, June 2020

[1]Graduate School of Oceanography, University of Rhode Island, Narragansett, Rhode Island

[*]Corresponding author email: xychen@my.uri.edu

Abstract

This study investigates the impacts of shoaling waves on the wind stress and drag coefficient (C_d) in coastal waters during tropical cyclone (TC) landfall. Numerical experiments are conducted using idealized TCs with two intensities, Category 1 and 5, and two translation speeds, 5 m/s and 10 m/s, propagating toward and normal to the shoreline over two bottom slopes, 1:200 and 1:2000. The wave spectra are simulated using the WAVEWATCH III wave model. The unresolved high-frequency spectral tail is parameterized as a function of wind speed and the full wave spectrum is used to calculate the wind stress and drag coefficient. Our results show that the sea-state dependence of wind stress magnitude (or C_d) is significantly increased in shallow water at a given wind speed. Compared to its deep-water value, C_d is enhanced in the right (due to shoaling fetch-dependent waves) and in the left (due to shoaling opposing-wind swells) TC quadrants. However, C_d is reduced in the front/rear quadrants due to weaker wind seas. The misalignment between the wind stress and wind speed directions is enhanced in shallow water. In general, the shoaling wave effects on the wind stress and C_d are much stronger on steeper bottom slopes and in faster moving storms.

3.1 Introduction

Exchange of momentum at the air-sea interface is one of the fundamental processes that influences the tropical cyclone (TC) intensity, the associated wind hazards and storm surges (*Emanuel*, 1986; *Ginis*, 2002; *Black et al.*, 2007). In the tropical cyclone, ocean (including storm surge), and coupled TC-ocean models, the wind stress is usually parameterized using the drag coefficient (C_d) that is a function of the 10-meter neutral wind speed (corrected for stability). Furthermore, it is often assumed that the drag coefficient is the same in deep water and in shallow water.

The drag coefficient in TC conditions has been extensively investigated in the past

two decades. Although uncertainty of C_d in high wind speeds remains large (e.g., *Hsu et al.*, 2017, Figure 1) observations generally agree that the well-established increase of C_d between 10m/s and gale-force winds ($17-20\ m/s$) does not continue in the hurricane-force wind ($> 33\ m/s$). Some observations show that C_d decreases roughly between 30 m/s and 50 m/s (e.g., *Powell et al.*, 2003; *Black et al.*, 2007; *Jarosz et al.*, 2007; *Holthuijsen et al.*, 2012; *Hsu et al.*, 2017, 2019). In other observations, C_d ceases to increase at a lower wind speed around $20-22\ m/s$ (e.g., *French et al.*, 2007; *Sanford et al.*, 2011; *Potter et al.*, 2015b). In extreme wind speeds above 50 m/s, *Bell et al.* (2012) and *Emanuel* (2003) suggest a constant C_d on average and *Soloviev et al.* (2014) suggest that C_d may have a local minimum around 60 m/s.

In contrast to deep water, observations of C_d in coastal waters ($< 30 - 50m$) during TC landfall are limited. *Zachry et al.* (2013) estimated C_d in a 3-km-wide ship channel during the passage of Hurricane Ike (2008). They report C_d to be higher than those observed in the open ocean for wind speeds below 30 m/s. *Zhao et al.* (2015) obtained wind profiles in two typhoons from a coastal observation tower located at 14 m water depth in the South China Sea. The C_d they derived reaches a maximum of $\sim 4 \times 10^{-3}$ at approximately $24m/s$ and decreases at higher wind speeds. From the same tower as in *Zhao et al.* (2015) and a nearby tower on the island, *Bi et al.* (2015) estimated C_d in the right quadrants of 7 typhoons using three methods (wind profile, inertial dissipation, and eddy covariance). The authors conclude that the wind profile method systematically overestimates C_d magnitude in coastal waters. Their estimated C_d is consistent with COARE 3.5 up to 18 m/s, and decreases above 18 m/s to around $1.5{\times}10^{-3}$ at 27 m/s. Among these three observational studies, the latter two better represent the effects of shoaling waves on C_d in TC conditions. Unfortunately, due to uncertainties associated with estimation methods and/or different TC wave conditions, the C_d magnitudes reported by these two studies differ by a factor of two. Hence, the impact of water depth on C_d in TCs remains inconclusive.

C_d in shallow waters has also been estimated in modeling studies, where the C_d–U_{10}

bulk relation is determined using optimization methods to improve accuracy of storm surge prediction (e.g., *Peng and Li*, 2015; *Zheng et al.*, 2018). These studies suggest that the C_d value at a given wind speed must be higher in shallow water than the commonly used deep-water values. However, these model-based estimates can be subject to uncertainties in the storm surge models and the optimization methods used.

Wave fields generated by tropical cyclones are often complex mixtures of wind seas and swells (e.g., *Wright et al.*, 2001; *Walsh et al.*, 2002; *Holthuijsen et al.*, 2012). *Potter et al.* (2015a) and *Hsu et al.* (2019) estimate that the wind stress direction can be rotated away from the wind direction by as much as 35° to 40° under TCs. To our best knowledge, the misalignment angle between wind and wind stress in shallow water during TC passage has not been observed so far.

Chen and Curcic (2016) used a fully coupled atmosphere–wave–ocean model to simulate wind stress in coastal waters during the landfall of Hurricanes Ike (2008) and Sandy (2012). Their results show an increase of wind stress at water depths less than 20 m, which is attributed to a decreased wave phase speed due to shoaling. It is also noted that C_d is increased by up to 25% on the left side of the TC center at landfall due to short-fetch waves against incoming swells. They also show that the misalignment between the wind and dominant waves is increased by refraction of dominant waves, and it is the largest in the front-left quadrant of the storms. These results suggest that the shoaling waves can significantly modify the wind stress and C_d. Therefore, it is highly desirable to expand such investigations beyond the two historical hurricanes.

In this study the shoaling wave impacts on the wind stress (C_d) are systematically investigated using idealized landfalling TCs with two different intensities, two different translation speeds, and two different bottom slopes. The same methodology is adopted as in Part I for simulation of the wave spectrum, parameterization of the spectral tail, and calculation of the sea-state dependent wind stress.

3.2 Method

3.2.1 WAVEWATCH III and Wind Stress Calculation

As in Part I, surface wave spectra are simulated using the WAVEWATCH III (WW3) wave model (v5.16), and the sea-state dependent wind stress is calculated using the two methods, Miami (*Donelan et al.*, 2012) and URI (*Reichl et al.*, 2014), with the empirical saturation spectrum tail level B_{sat} derived based on the GFDL bulk C_d parameterization as a function of 10-meter wind speed (see Part I Section 3.2.1).

3.2.2 Idealized TC Wind

Idealized tropical cyclone wind fields are generated using the Holland model (*Holland*, 1980). The tangential wind speed (V) at a radial distance (r) from the storm center is parameterized with the following equations:

$$V(r) = \begin{cases} \left(\frac{AB(P_n - P_c)}{\rho r^B} e^{-A/r^B} \right)^{1/2} & 0 \le r \le R_{max} \\ \left(\frac{AB(P_n - P_c)}{\rho r^B} e^{-A/r^B} + \frac{r^2 f^2}{4} \right)^{1/2} - \frac{rf}{2} & r > R_{max} \end{cases} \tag{3.1}$$

with,

$$B = \frac{\rho e V_{max}^2}{P_n - P_c} \tag{3.2}$$

$$A = R_{max}^B.$$

where V_{max} is the maximum wind speed, R_{max} is the radius of maximum wind, and P_c, P_n are central pressure and environmental pressure, respectively. The air density ρ is assumed constant at $1.15 kg/m^3$ and the Coriolis parameter f is set to the value at $20°N$. The value of B is set to 1.6 and hence the pressure deficit is not explicitly specified. In order to introduce a radial wind component and asymmetry to the wind field, the inflow angle is specified, and half the translation speed is added to the wind field above as in *Moon et al.* (2003).

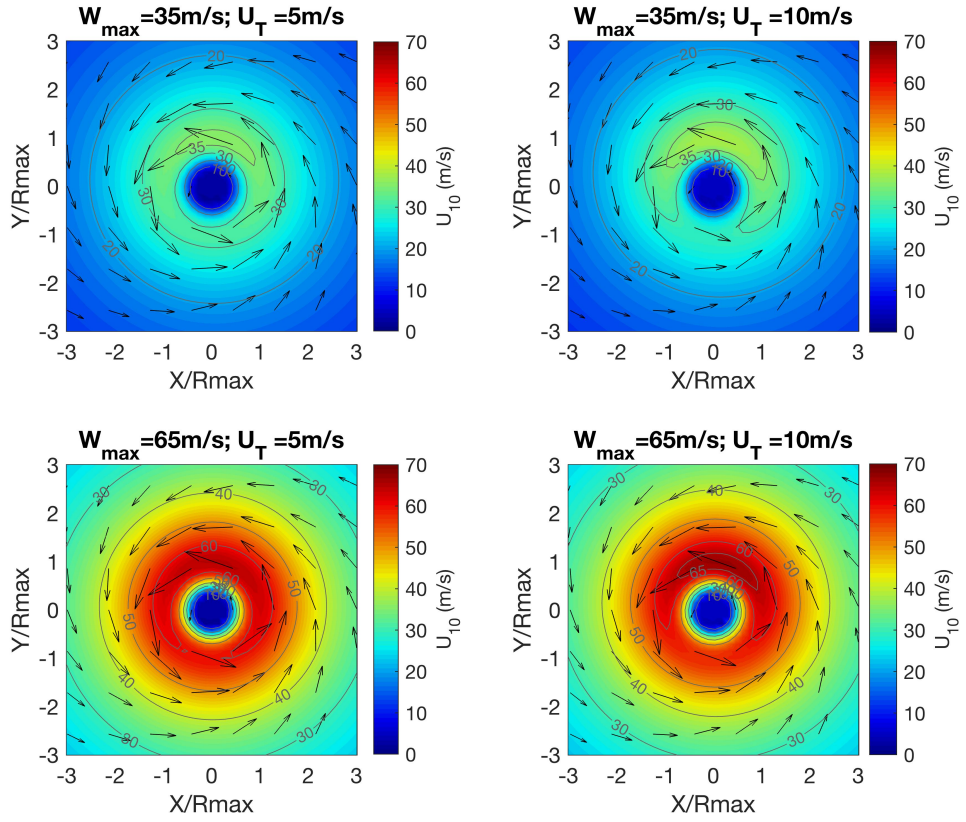

Figure 3.1: Wind fields of four idealized tropical cyclones in this study. Upper (lower) panels: TC with maximum wind speed V_{max}= 35 m/s (65 m/s), Category 1 (5) hurricane strength. Left (right) panels: translation speed U_T=5 m/s (10 m/s). Radius of maximum wind (R_{max}) is 70 km. Distance in x-, y-axis is normalized by R_{max}. The TCs propagate in the negative x direction.

Four idealized TCs with two maximum wind speeds, V_{max}= 35 m/s and 65 m/s, (corresponding to Category 1 and Category 5 hurricanes according to the Saffir-Simpson hurricane wind scale) and two translation speeds, U_T= 5 m/s and 10 m/s, are used to force the wave model. The radius of maximum wind (R_{max}) is set 70 km for all cases. These four idealized TC wind fields are shown in Fig. 3.1.

3.2.3 Wave Spectra Simulations

The shoaling wave spectra are simulated in the TCs approaching the coastline at a normal angle. When a TC propagates at a constant translation speed in deep water, a quasi-

Table 3.1: Multi-grid resolutions in the shoaling domain

Bottom Slope	Coarse Grid (km)	Fine Grid (km)
1:200	$\Delta x = 1$, $\Delta y = 2$	$\Delta x = 0.4$, $\Delta y = 0.8$
1:2000	$\Delta x = \Delta y = 10$	$\Delta x = \Delta y = 4$

steady wave field (a wave field that is steady in a reference frame that moves with the storm) is established. Such deep-water quasi-steady TC wave fields are generated in a 4000 km by 1800 km domain with a uniform water depth of 4000 m at 10 km uniform spatial resolution. This deep-water domain is then attached to a high-resolution shoaling domain. Starting from the time when the TC center is 800km from the boundary between the two domains, the quasi-steady deep-water TC wave field is gradually introduced into the shoaling domain through 1-way nesting. The wave simulation in the shoaling domain is terminated when the TC center is 600 km inland from the shoreline.

In the shoaling domain, the simulations are conducted on two grids with different spatial resolutions using the multi-grid version of WW3. In the area with 50 m to 500 m water depth, a coarser grid is used with a 5-m depth variation between the grid points. In the nearshore region shallower than 50 m, a finer grid is used with a 2-m depth variation between the grid points. The cross-shore dimension of the coarse and fine grids with a 1:200 bottom slope is 100km and 10km, respectively, and it is ten times larger with a 1:2000 bottom slope. The alongshore dimension of both grids is 1200 km, regardless of the bottom slope. The spatial resolution of the coarse and fine grids vary depending on the bottom slope, either 1:200 or 1:2000 (Table 3.1).

Similar to the uniform wind experiments in Part I, for each landfalling TC experiment, a control experiment is conducted with a flat and deep bottom, and sea-state dependent C_d is calculated for comparison. Although the wave fields are quasi-steady in deep water, the wave spectra can be slightly altered by the varying grid resolutions. Therefore, the control experiment for each case is performed with the same grid configuration as in the shoaling domain (Table 3.1).

3.3 Results

When the quasi-steady wind/wave fields are established under a translating TC in deep water, the spatial distribution of a wind or wave variable (such as, significant wave height, sea-state dependent drag coefficient) also represents the temporal evolution of the same variable along a transect that is perpendicular to the storm track. (Since the storm propagates in the negative x direction, the x-axis of the spatial snapshot is equivalent to the time (t) axis, with a relation $x = U_T t$, where U_T is the storm translation speed.)

Once the storm enters the shoaling region, the wave field is not quasi-steady anymore. Nevertheless, it is beneficial to examine how a variable at a particular location relative to the storm center is modified due to the depth change. In this section, all the two-dimensional (2D) figures at a particular depth are constructed by first extracting results at that depth (i.e., along a y- transect perpendicular to the storm propagation) as time progresses. To enable comparison in the TC-centered spatial coordinates, time t is then converted to distance x using the same relation $x = U_T t$. Therefore, negative x values denote results prior to the TC center arrival at that depth and positive x values indicate results after the passage of the TC center. Only in deep water the 2D figures are true spatial snapshots in the quasi-steady state.

All the 2D figures shown in this section are generated under the intense TC with V_{max}=65 m/s and U_T=5 m/s or 10 m/s. The results of the weaker TC (V_{max}=35 m/s) are qualitatively similar and are not shown.

3.3.1 Characteristics of Shoaling TC Waves

Shoaling wave fields generated by the strong fast-moving hurricane (V_{max}=65 m/s and U_T=10 m/s) are shown in Fig. 3.2 and Fig. 3.3. As expected, the significant wave height (H_s) and the mean wavelength (L_m) are both reduced everywhere as water depth decreases because of the enhanced wave dissipation. Even at the 40 m water depth, the wave field has already been modified significantly compared to those in the deep water. At a given water depth, both H_s and L_m are reduced more strongly in the gentler

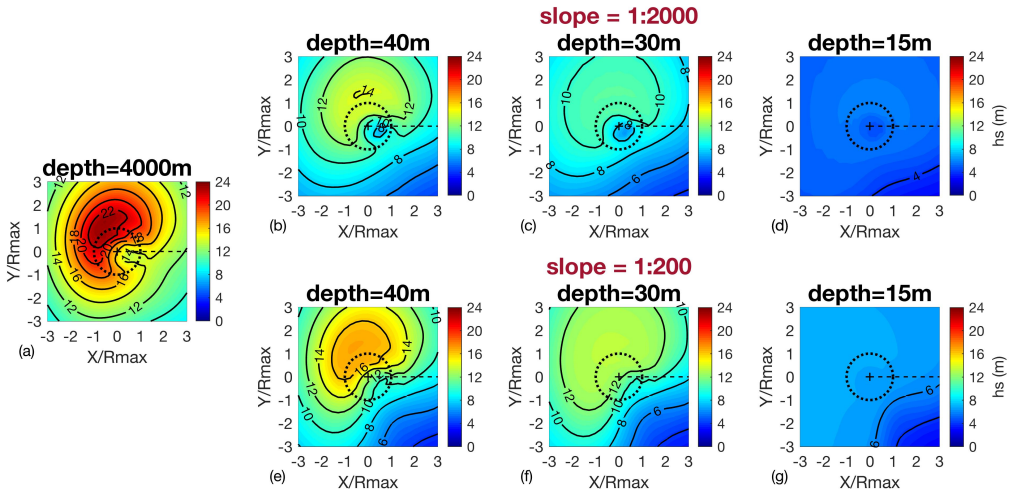

Figure 3.2: Spatial-temporal variation of significant wave height (H_s) in deep water (a) and at three different depths, 40 m (b,e), 30 m (c,f), 15 m (d,g), under a strong fast-moving TC with V_{max}=65 m/s and U_T=10 m/s. The upper panels (b–d) show results on 1:2000 slope, the lower panels (e–g) show results on 1:200 slope. Black solid contours are drawn every 2 m in significant wave height. Dashed horizontal line is the TC track. Thin dotted circle marks R_{max}.

slope case. Since waves propagate a longer distance over a gentler slope compared to a steeper slope they are dissipated through breaking and bottom friction more efficiently, as discussed in Part I.

3.3.2 Variability of Drag Coefficient due to Shoaling TC Waves

3.3.2.a Spatial-temporal Variability

The spatial-temporal variation of the shoaling wave-impacted drag coefficient during TC landfall is shown in Figs. 3.4, 3.6 and 3.8. The ratio of the shoaling-impacted C_d to the deep-water C_d for the corresponding three cases is shown in Figs. 3.5, 3.7 and 3.9, respectively. Here, the drag coefficient is defined as the wind friction velocity squared divided by the 10-meter wind speed magnitude squared, even if the 10-meter wind direction and the wind stress direction are misaligned (as discussed in section 3.3).

Fig. 4 shows the sea-state dependent C_d in the strong slow-moving TC (V_{max}=65 m/s

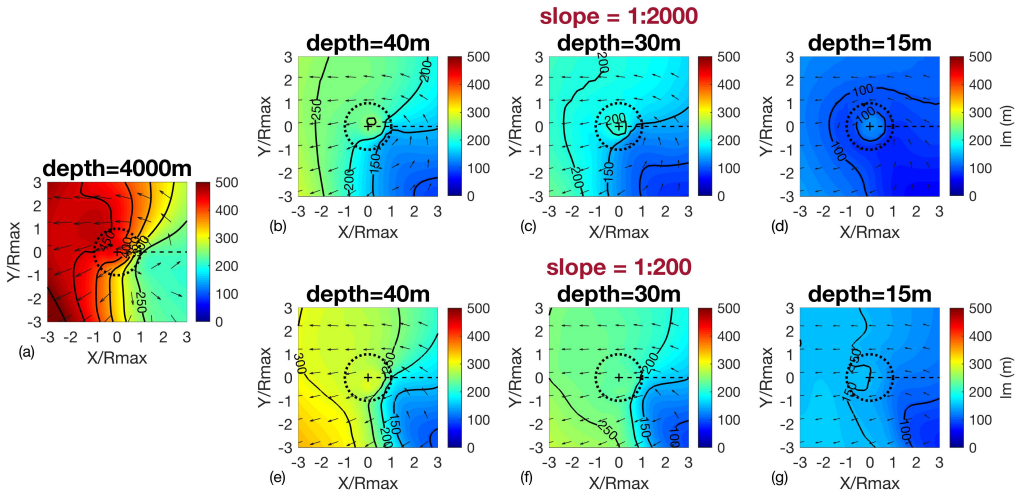

Figure 3.3: Spatial-temporal variation of mean wavelength (L_m) in deep water (a) and at three different depths, 40 m (b,e), 30 m (c,f), 15 m (d,g), under a strong fast-moving TC with V_{max}=65 m/s and U_T=10 m/s. The upper panels (b-d) show results on 1:2000 slope, the lower panels (e-g) show results on 1:200 slope. Black solid contours are drawn every 50m in mean wavelength. The vectors represent propagation direction of dominant waves and the length of the vectors is proportional to the phase speed of dominant waves. Dashed horizontal line is the TC track. Thin dotted circle marks R_{max}.

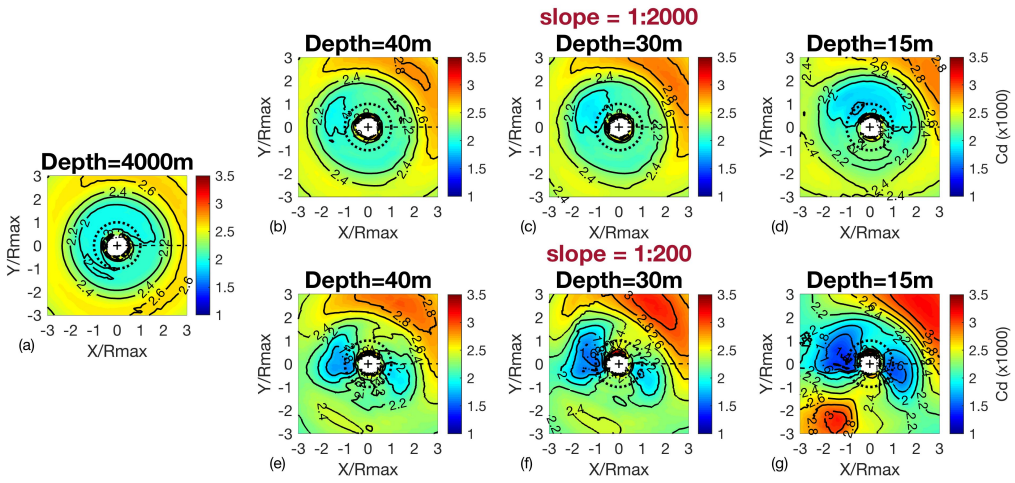

Figure 3.4: Spatial-temporal variation of C_d (calculated using URI method) in deep water (a) and at three different depths, 40 m (b,e), 30 m (c,f), 15 m (d,g), under a strong slow-moving TC with V_{max}=65 m/s and U_T=5 m/s. The upper panels (b-d) show results on 1:2000 slope, the lower panels (e-g) show results on 1:200 slope. Solid black contours are drawn every 0.2 in C_d(x1000). Dashed horizontal line is the TC track. Thin dotted circle marks R_{max}.

and U_T=5 m/s) case calculated using the URI method. The contours of the deep-water C_d (Fig. 4a) almost follow the circular wind speed contours, that is, C_d mainly depends on wind speed and its sea-state dependence is quite weak. Relative to the bulk GFDL C_d, the sea-state dependent C_d near R_{max} is slightly lower in the front-right quadrant of the TC, where the waves are higher and more developed than those in the rear-left TC quadrant. Note that the sea-state dependence of C_d in deep water in this study is not as strong as those reported in *Reichl et al.* (2014). This is because the wave fields, simulated with source term parameterization of *Ardhuin et al.* (2010) in WW3 in this study, show reduced spatial variation (or reduced asymmetry) of H_s along wind speed contours, compared to those in *Reichl et al.* (2014) simulated with *Tolman and Chalikov* (1996) source term parameterizations in WW3.

As water depth decreases, the magnitude and spatial distribution of C_d are modified in a complex manner underneath the landfalling TC (Fig. 4b–4g). Interestingly, these

C_d modifications show significant differences between cases with different bottom slopes. It is easier to interpret these results by examining the shoaling effect (Fig. 5), which is the ratio of C_d in shallow water relative to C_d in deep water at the same location relative to the storm center (for example, Fig. 5a shows the ratio of C_d in Fig. 4b and Fig. 4a).

Here, we mainly focus on the high wind area (the distance from the storm center roughly between R_{max} and $3R_{max}$). On the steeper bottom slope at a 40m depth (Fig. 5d), C_d is significantly increased (by more than 20%) in the right (toward right-rear) TC quadrant. It is also increased in the left (toward left-front) quadrant, but it is decreased in the front (toward front-right) and rear (toward rear-left) quadrants. As depth decreases from 40m to 30m (Fig. 5e), the increase/decrease of C_d is further enhanced. When depth decreases to 15m (Fig. 5f), the C_d increase on the right almost disappears, but the increase on the left and the decrease in the front/rear are significantly enhanced. On the gentler slope (Fig. 5a–c), the overall shoaling effect is much weaker. Significant C_d increase (more than 10%) is observed only on the right (toward right-rear) at 40m and 30m depths, and on the left (toward left-front) at 15m depth. No significant C_d decrease is observed.

When the TC translation speed is doubled to 10m/s (Figs. 6 and 7), the overall spatial-temporal patterns of C_d and C_d ratio are similar to those with the slow-moving TC (Figs. 4 and 5) but the increase/decrease of C_d is further enhanced. In particular, at 15m depth on the steeper bottom, the increase of C_d in the left (toward left-front) quadrant exceeds 70% (Fig. 7f).

The C_d results in the strong fast-moving TC case calculated using the Miami method are shown in Figs. 8 and 9. In general, the Miami method shows very similar patterns of C_d and C_d ratio compared to those using the URI method (Figs. 6 and 7) The results in other cases are also very similar between the two methods (not shown). This suggests that the shoaling impact on the sea-state dependent C_d is quite robust and is not dependent on how the C_d is calculated.

In summary, the shoaling impact on C_d is much stronger on a steeper bottom slope

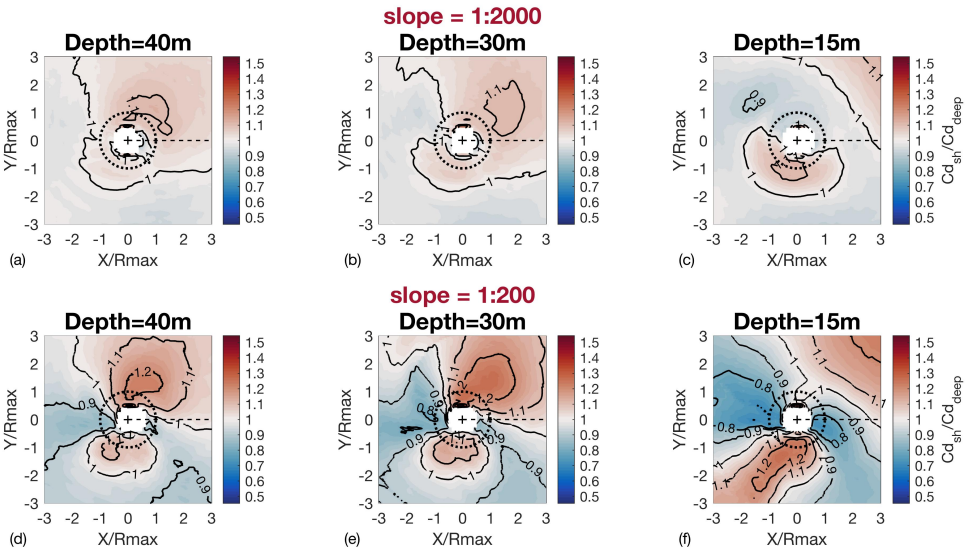

Figure 3.5: Spatial-temporal variation of C_d ratio (ratio of sea-state dependent C_d in shallow water to that in deep water, calculated using URI method) at three different depths, 40 m (a,d), 30 m (b,e), 15 m (c,f), under a strong slow-moving TC with V_{max}=65 m/s and U_T=5 m/s. The upper panels (a–c) show results on 1:2000 slope, the lower panels (d-f) show results on 1:200 slope. Solid black contours are drawn every 0.1 in C_d ratio. Dashed horizontal line is the TC track. Thin dotted circle marks R_{max}.

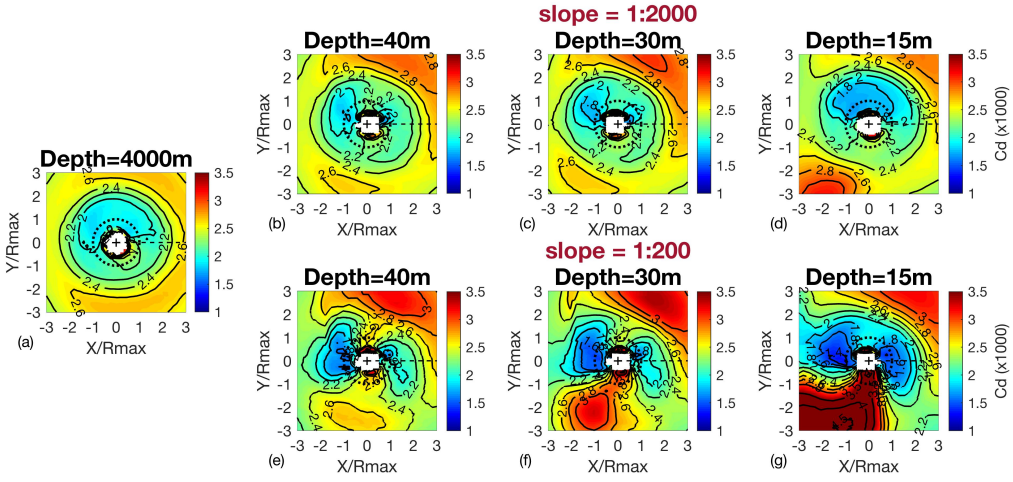

Figure 3.6: Same as Fig. 3.4, but under a strong fast-moving TC with V_{max}=65 m/s and U_T=10 m/s.

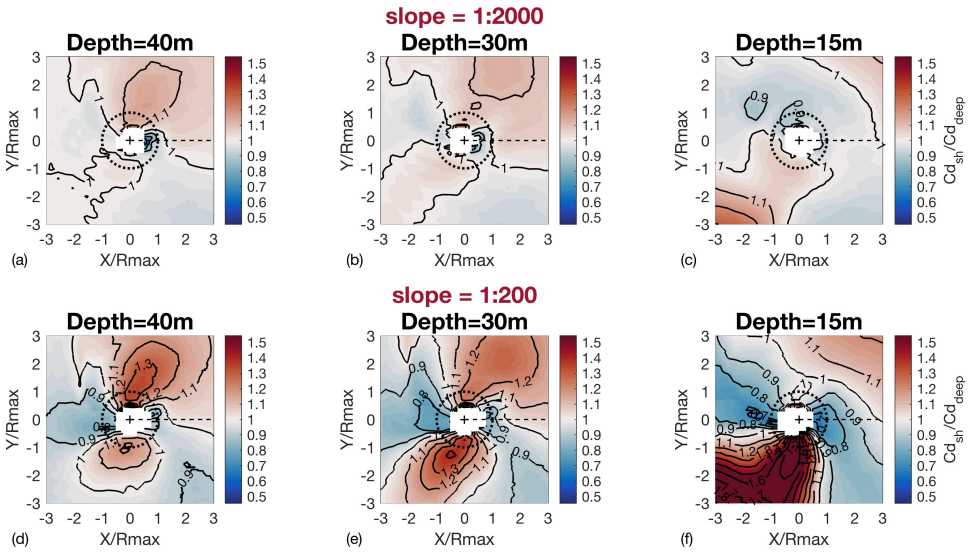

Figure 3.7: Same as Fig. 3.5, but under a strong fast-moving TC with V_{max}=65 m/s and U_T=10 m/s.

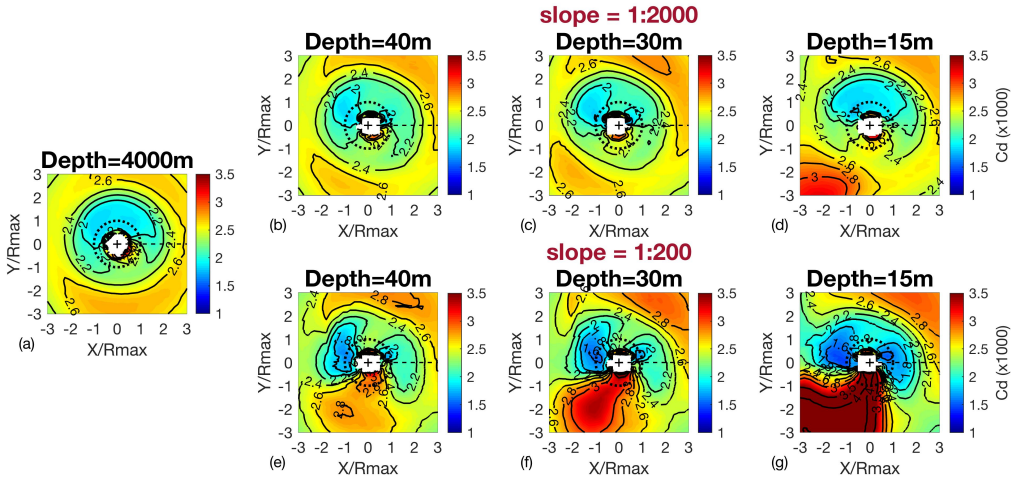

Figure 3.8: Spatial-temporal variation of C_d computed using Miami Method under a strong fast-moving TC with V_{max}=65 m/s and U_T=10 m/s (compare to Fig. 6).

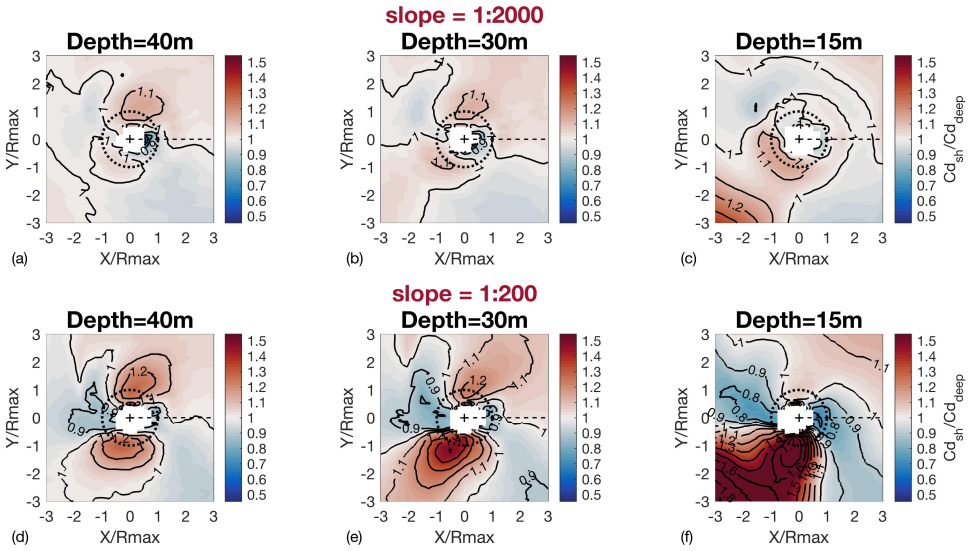

Figure 3.9: Spatial-temporal variation of C_d ratio computed using Miami Method under a strong fast-moving TC with V_{max}=65 m/s and U_T=10 m/s (compare to Fig. 3.7).

and in a faster propagating TC. It varies significantly depending on the location relative to the storm center. This is further investigated in Section 3.4.

3.3.2.b Variability in the C_d–U_{10} Relation

In this section, the results of the sea-state dependent C_d with shoaling waves are presented as C_d–U_{10} scatter figures. The data are binned every 5m/s interval, and the statistical distribution of C_d in each wind speed bin is shown with a box-whisker plot, indicating its mean, median, as well as the lowest 2.5%, 25%, 75%, and 97.5% values. The data are color coded by the wave age, which is defined as $c_p \cos\psi/u_*$, where ψ is the angle between the dominant wave direction and the wind stress direction. Negative wave ages suggest presence of opposing-wind swells (swell whose direction is more than 90 degrees away from the wind direction), which generally occurs to the left of the TC.

Fig. 3.10 shows the results at all locations where wind speed exceeds 10 m/s in the strong slow-moving TC case (V_{max}=65 m/s, U_T=5 m/s). Here, C_d is calculated using the URI method. In deep water (Fig. 3.10a), sea-state dependence is generally weak. Although there are some outliers with high C_d values (over opposing-wind swells),

the 95% interval is quite small. As the water depth decreases, the variability of C_d significantly increases particularly with the steeper bottom slope. As discussed above, higher values of C_d in the high wind region mainly occur on the right (positive wave age) at 30 to 40 m depths and on the left (negative wave age) at 15 m depth. The mean and median values of C_d still closely follow the GFDL bulk C_d parameterization.

As the translation speed increases to 10 m/s (Fig. 3.11), the variability of C_d further increases. In particular, at the 15 m depth with the steeper slope (Fig. 3.11g), some C_d values with negative wave ages (over opposing-wind swells) become very large, and the mean and median values are increased by 5–10% relative to the GFDL bulk C_d. These high C_d values are mainly observed in the TC left-front quadrant (Fig. 3.6g).

The C_d variability in the weak slow-moving TC (V_{max}=35 m/s, U_T=5 m/s, not shown) and the weak fast-moving TC (V_{max}=35 m/s, U_T=10 m/s, Fig. 3.12) is overall similar to the C_d variability in the strong TC cases (Figs. 3.10 and 3.11). The only notable difference from the strong TC cases is that the effect of opposing-wind swells on the left is significantly reduced with the weak TCs.

The results under the strong fast-moving TC (V_{max}= 65m/s, U_T=10 m/s) but calculated with the Miami method are shown in Fig. 3.13. The overall results are quite similar to those with the URI method (Fig. 3.11). However, the variability of C_d with positive wave ages (mainly on the right of the TC track) is reduced, and the variability with negative wave ages (mainly on the left of the TC track) is enhanced.

3.3.3 Misalignment Between 10-meter Wind and Wind Stress Directions

The misalignment angle (ϕ) between the 10-meter wind direction and wind stress direction for the strong and fast-moving TC are shown in Fig. 3.14 and Fig. 3.15. Positive (negative) values mean the wind stress direction turns clockwise (counter-clockwise) from the 10-meter wind direction. In general, the results are qualitatively similar between the URI and Miami methods, but the magnitude of misalignment angle is consistently much larger with the Miami method particularly in the TC front-left quadrant. With both

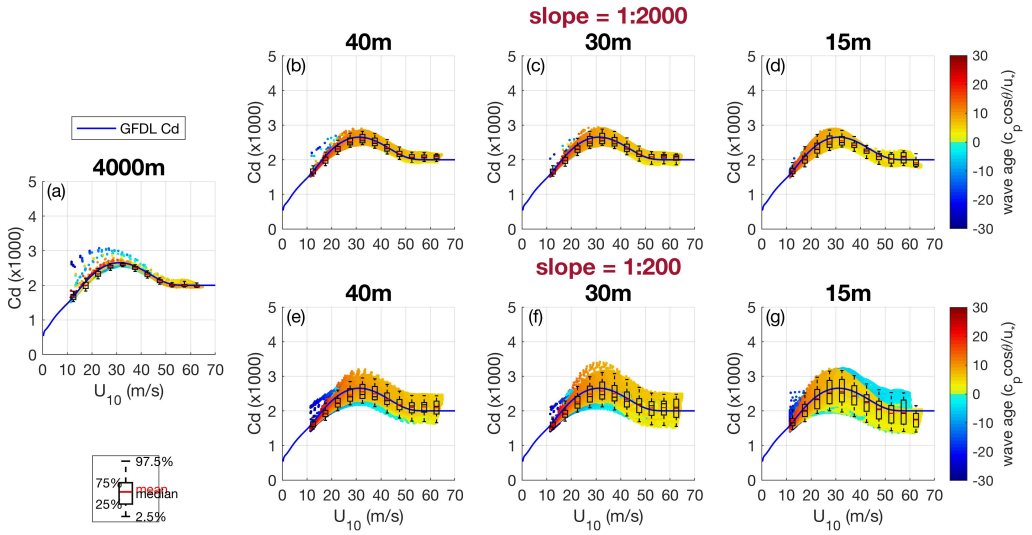

Figure 3.10: C_d–U_{10} scatter plots in deep water (a) and at three different depths, 40m (b,e), 30m (c,f), 15m (d,g), under a strong slow-moving TC with V_{max}=65 m/s, U_T=5 m/s. C_d is computed using URI Method. The upper panels (b-d) show results on 1:2000 slope, the lower panels (e-g) show results on 1:200 slope. Data are color coded by wave age ($c_p \cos\psi/u_*$). The rectangular box with two whiskers shows data statistics in a given wind speed bin. The red and black lines in the box denote the mean and median C_d values respectively. The bottom and top of the rectangular box mark the 25^{th} and 75^{th} percentile of the C_d values. The lower and upper whisker levels indicate the 2.5^{th} and 97.5^{th} percentile of the data. The blue line is the GFDL bulk C_d.

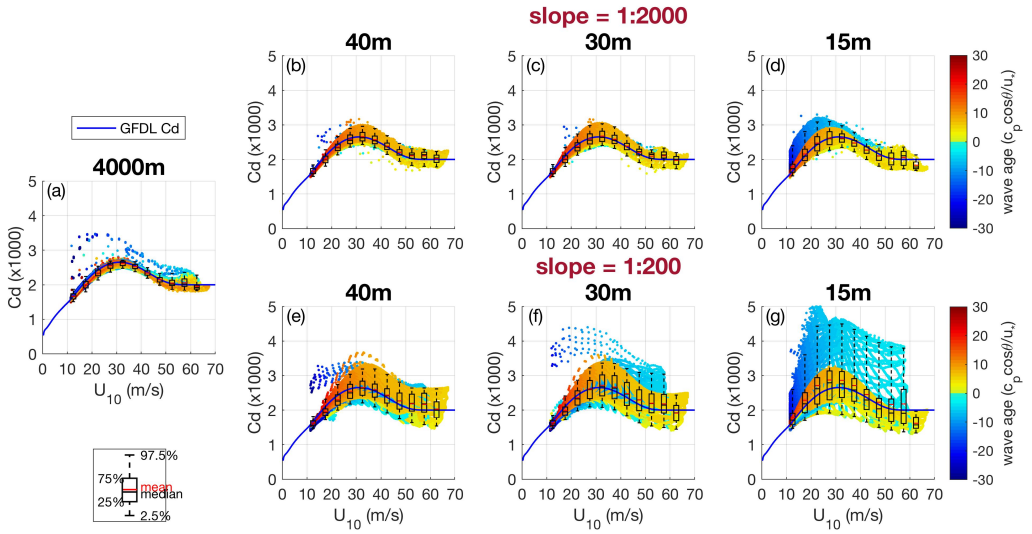

Figure 3.11: Same as Fig. 3.10, but under a strong fast-moving TC with V_{max}=65 m/s, U_T=10 m/s.

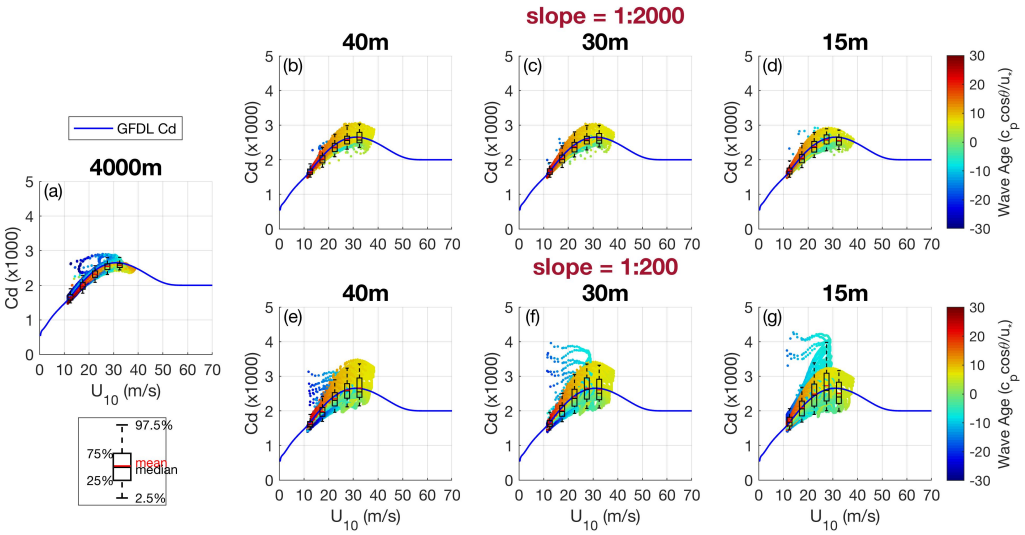

Figure 3.12: Same as Fig. 3.10, but under a weak fast-moving TC with V_{max}=35 m/s, U_T=10 m/s.

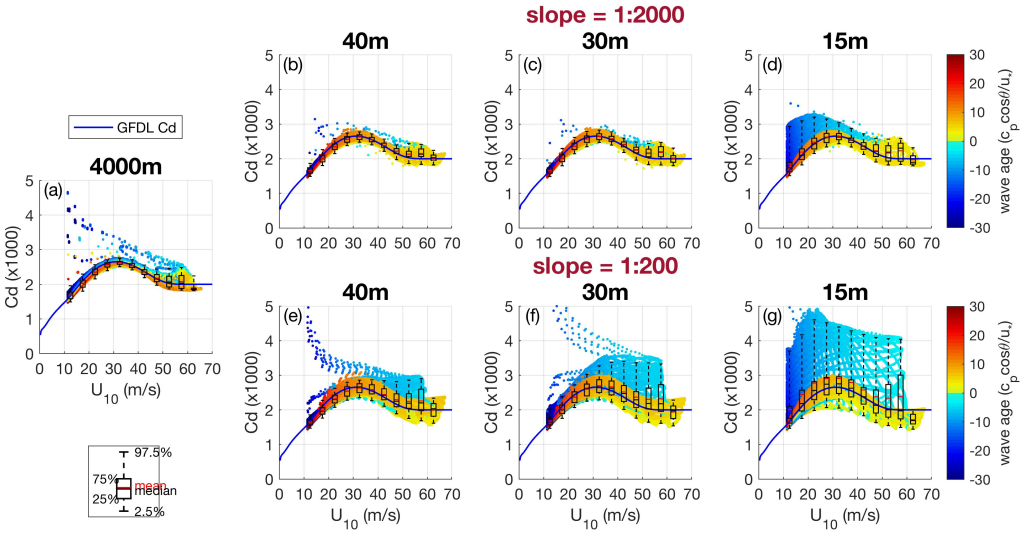

Figure 3.13: C_d calculated using Miami method under a strong fast-moving TC with V_{max}=65 m/s, U_T=10 m/s (compare to Fig. 11).

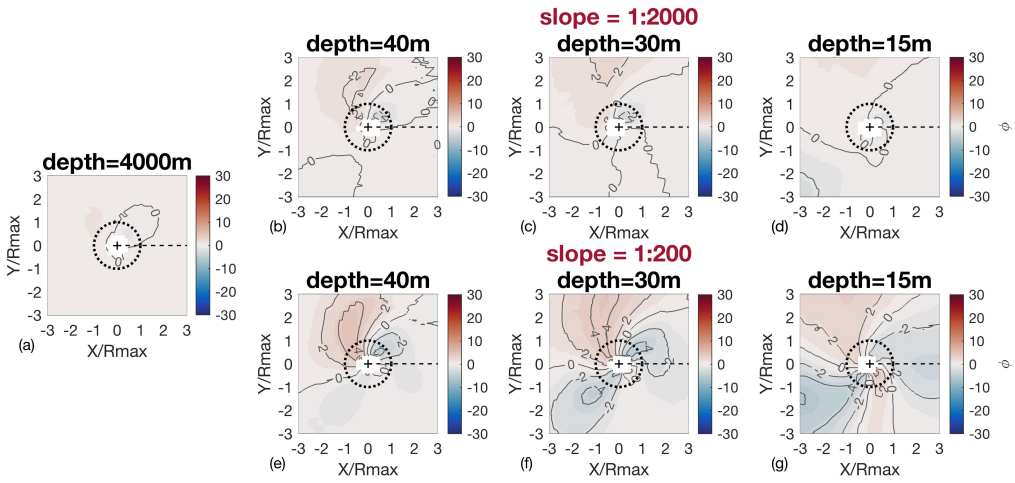

Figure 3.14: Spatial-temporal variation of misalignment angle (in degrees) between 10-meter mean wind direction and wind stress direction, in deep water (a) and at three different depths, 40m (b,e), 30m (c,f), 15m (d,g), under a strong fast-moving TC with V_{max}=65 m/s and U_T=10 m/s. The upper panels (b–d) show results on 1:2000 slope, the lower panels (e–g) show results on 1:200 slope. Thin black contours are drawn every 2 degrees. Dashed horizontal line is the TC track. Thin dotted circle marks Rmax. Wind stress is calculated using the URI method.

methods the misalignment is significantly increased in shallow water, particularly with the steeper bottom slope of 1:200. At all shallow water depths, the misalignment is positive in the TC front-right quadrant and negative in the rear-right quadrant. This is because part of the stress is supported by the misaligned dominant waves, hence, the wind stress direction turns toward the dominant wave direction (see Fig. 3.3).

The misalignment angle is negative in the TC front-left, because part of the stress is supported by the opposing-wind swell. Since such swell is pushed backward by wind, the stress supported by the swell is in the opposite direction of the swell propagation. Hence, the wind stress direction turns toward the opposite of the swell direction (see Fig. 3.3). At the 15m depth, the misalignment becomes positive in the TC rear-left for the same reason.

The large difference of the misalignment angle magnitude between the URI and Miami methods is due to different assumptions made in modeling the vertical wind profile

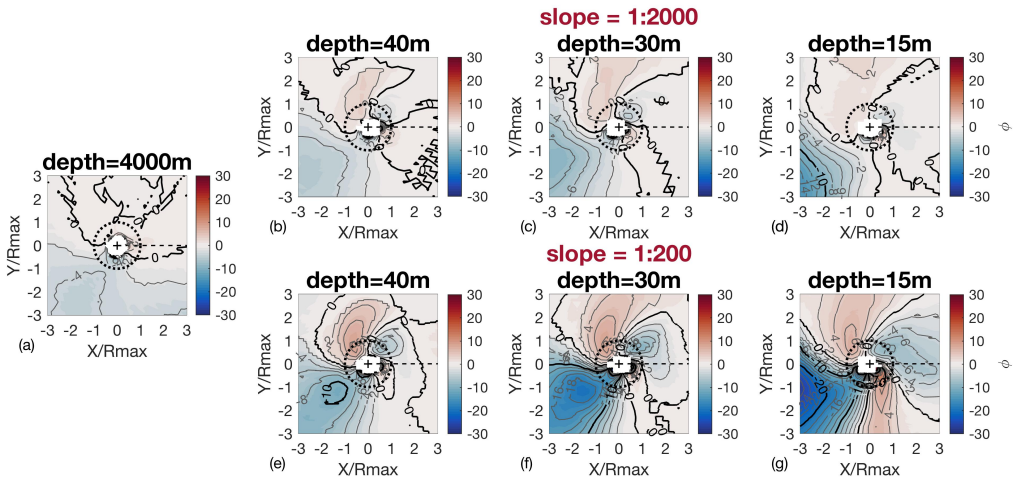

Figure 3.15: Same as Fig. 3.14 but wind stress is calculated using the Miami method. Thin black contours are drawn every 2 degrees. Thick black contours are drawn every 10 degrees.

(*Reichl et al.*, 2014). In the Miami method, the wind profile is assumed to be logarithmic with no variation of the wind direction with height up to 10m. As a result, the misalignment angle ϕ at 10m is the same as that at the water surface. However, in the URI method the wind is allowed to turn with height and the misalignment angle ϕ varies with height; it is smaller at 10m height compared to that near the surface.

In summary, regardless of the modeling methods, wind stress direction is steered toward the dominant wave direction wherever dominant waves are misaligned with wind by less than 90 degrees, and wind stress direction is steered toward opposite of the dominant wave direction wherever the dominant waves are misaligned with wind by more than 90 degrees. These patterns of rotation are mainly determined by the characteristics of the TC wave fields and they are qualitatively consistent with the illustration in *Grachev et al.* (2003), who systematically investigated misalignment between wind and wind stress in different conditions.

3.3.4 Explanation of Shoaling Impacts on C_d in Different TC Quadrants

One significant finding of this study is that the shoaling impact on C_d at a particular point strongly depends on its location relative to the storm center. In this section, we examine the impacts of shoaling in four different TC quadrants. For reference, the selected points are described in a TC-following polar coordinate system (r, θ), where the origin is at the TC center, θ=0 is the TC translation direction (negative x direction), and θ increases in the clockwise direction.

3.3.4.a C_d in the TC Right (toward rear-right) Quadrant

A point at (r=R_{max}, θ=90°) is selected to analyze the increase of C_d in the TC right (toward right-rear) quadrant. The wave field at this location is dominated by waves whose group velocity is similar to the storm translation speed U_T and are continuously forced by wind as the storm propagates. Therefore, it is expected that such a wave field is not very different from a simple fetch-limited wave field, and its effective fetch is determined by the TC maximum wind speed V_{max} and the TC translation speed U_T. Indeed, the directional wavenumber spectrum at this location is well aligned with wind and is relatively simple (Fig. 3.16a,b,c).

Fig. 3.17 compares the variation of C_d with decreasing depth at the location (R_{max}, 90°) to the corresponding C_d variation obtained from the uniform wind experiments (Part I) with the wind speeds equal to V_{max} of the TCs and with the same bottom slope. It is seen that the variation of C_d in all TC experiments (regardless of V_{max}, U_T, and bottom slope) is quite similar to the variation of C_d under the uniform wind with a particular fetch (WDL). The effective fetch of the TC wave field increases with V_{max} and U_T, as expected. As in the uniform wind case, the C_d enhancement in the TC case is also significantly reduced with a gentler slope. The only notable difference between the two cases (TC versus uniform wind) is that the enhancement of C_d is slightly larger in the TC case than that in the uniform wind case.

In summary, the C_d increase in the right (toward right-rear) quadrant of a TC

during landfall can be mostly explained by the shoaling of simple fetch-dependent waves investigated in Part I. The enhancement seen in this quadrant is mainly due to slowing down and steepening of the dominant long wave components when they propagate from deep to finite depth water.

3.3.4.b C_d in the TC Front (toward front-right) and Rear (toward rear-left) Quadrants

Over the steeper slope (1:200), C_d is significantly reduced in the front (toward front-right) and rear (toward rear-left) quadrants. At these locations, the wave fields are categorized as crossing-swells (*Liu et al.*, 2017), where the TC generated swells cross the wind seas at an angle close to 90°. Therefore, swells are not likely responsible for the C_d reduction (see Eqs. 2.3 & 2.4 in Part I). Instead, a closer inspection of the directional wavenumber spectra reveals that the reduced wind sea spectra are responsible for the C_d reduction.

Figs. 16d–16f show the mixed-sea wave spectra taken at $(R_{max}, 0°)$ in deep water and at 30 m depth with two different bottom slopes. In deep water (Fig. 16d), even though the dominant wave direction is significantly misaligned from the wind direction, the wind sea is well developed and the directional spread of wind sea energy is symmetric with respect to the wind. At 30 m depth with the gentler slope (1:2000) (Fig. 16e), longer wind seas appear to be rotated to the shore normal direction due to refraction, but shorter wind seas are still well aligned with wind and as energetic as in deep water. In contrast, with the steeper slope (Fig. 16f), the wind sea spectrum is significantly reduced compared to that in deep water. Waves longer than 50 m in the wind direction mostly disappear and even shorter waves are less developed and primarily moving toward the shore. This significant reduction of the wind sea spectrum inevitably decreases the magnitude of wind stress and hence C_d. The spectra taken at $(R_{max}, 180°)$ also display similar (but weaker) trend of reduced wind sea spectrum at 30 m depth with the steeper slope (Figs. 16g-16i).

This reduction of the wind sea spectra at 30 m depth with the 1:200 bottom slope is

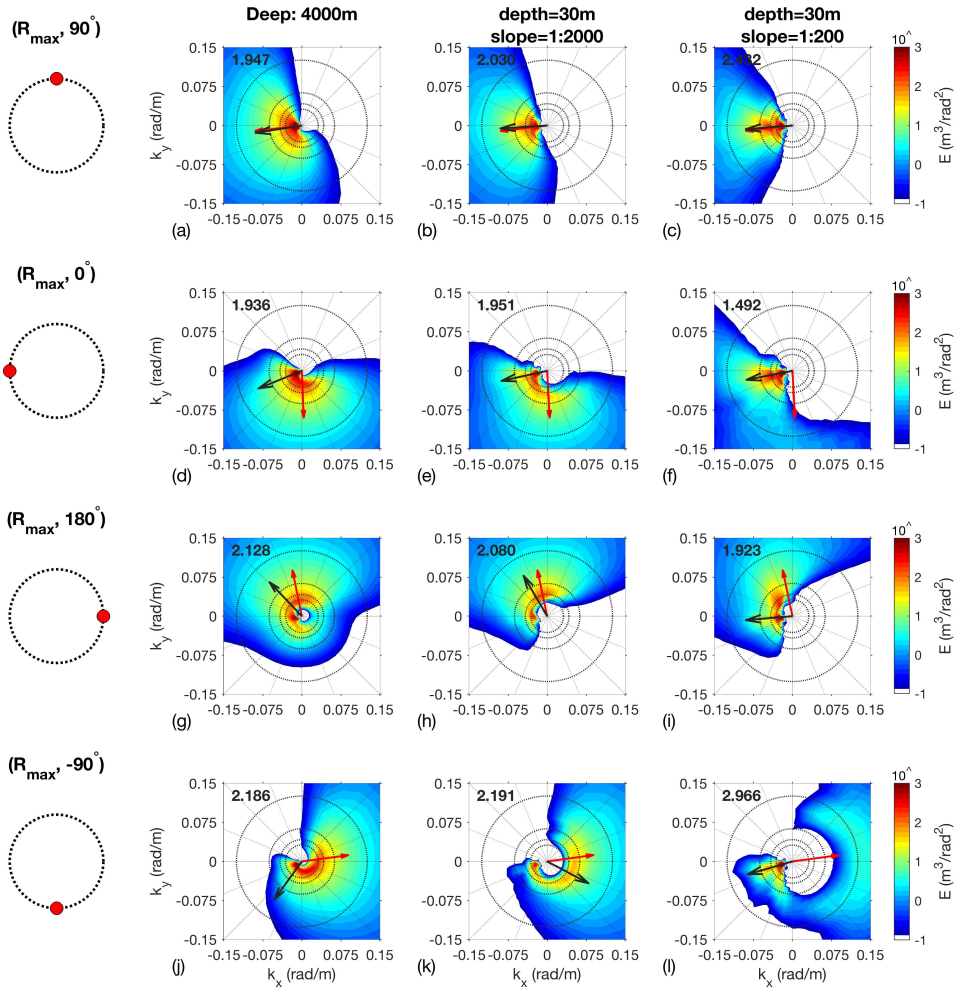

Figure 3.16: Comparison of directional wavenumber spectra at deep water (4000 m) and at 30m depth on two bottom slopes at 4 different locations relative to the TC center. From top to bottom, spectra are shown in the right (90°), front (0°), rear (180°) and left (−90°) of the TC center as indicated by the sketch in the first column. In each spectrum plot, red arrows show wind direction and black arrows show dominant wave direction. Dotted concentric circles denote wavelength every 50 m starting from 50 m. Numbers on the upper left corner in each panel is the drag coefficient value (x1000).

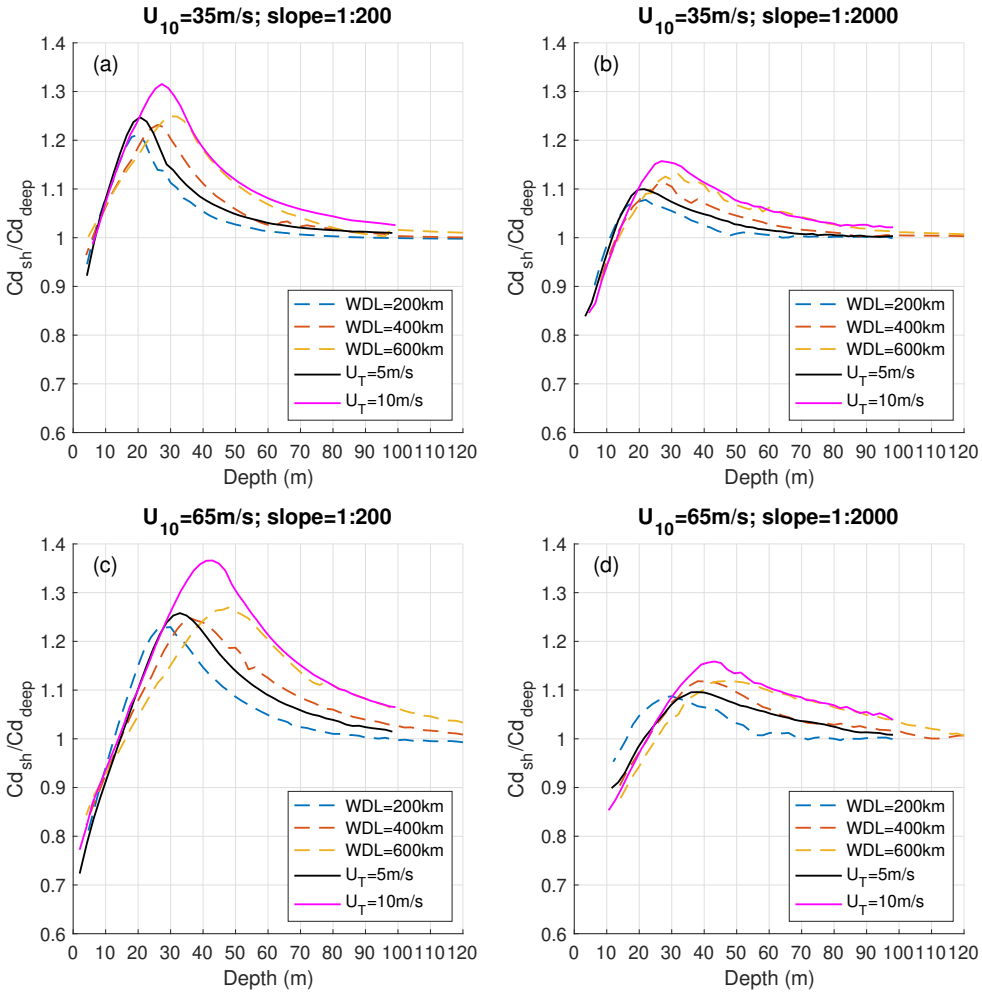

Figure 3.17: Variation of C_d ratio (ratio of sea-state dependent C_d in shallow water to that in deep water, calculated using the URI method) with decreasing water depth. Dashed lines are results from the uniform wind experiment in Part I with wind speed 35 m/s (a,b) or 65 m/s (c,d) and with three different domain lengths. Solid lines are results under a weak TC (V_{max}= 35m/s) (a,b) or a strong TC (V_{max}= 65m/s) (c,d) with two translation speeds, observed at distance R_{max} to the right of the storm center. The left panels (a,c) show results on 1:200 slope, the right panels (b,d) show results on 1:2000 slope.

mainly because this location is only 6 km from the shoreline. When the point $(R_{max}, 0°)$ reaches this depth, most of the forward half of the TC is already on land and does not generate wind seas. This explains almost complete disappearance of wind waves propagating toward offshore. In contrast, with the gentler slope of 1:2000, the 30 m depth location is 60 km from the shoreline and the storm can generate well-developed wind seas by the time the point $(R_{max}, 0°)$ reaches this depth. The same explanation can be applied to the point $(R_{max}, 180°)$.

In summary, the reduction of energetic, stress supporting, wind seas (offshore propagating waves in particular) is responsible for the C_d reduction in the front (toward front-right) and rear (toward rear-left) quadrants. The reduction of wind seas is caused by the proximity to the shoreline and is only important when the bottom slope is steep.

3.3.4.c C_d in the TC Left (toward left-front) Quadrant

The enhancement of C_d in the TC left (toward left-front) quadrant is associated with opposing-wind swells, that is, where the wind-wave misalignment angle exceeds 90°. This has been further confirmed by an additional experiment in which the negative growth rate parameter (c_β) for opposing-wind swells is set to zero. The associated results (not shown) indicate that the C_d enhancement in the TC left (toward left-front) quadrant disappears. Therefore, it is expected that the magnitude of C_d enhancement in this quadrant is sensitive to the choice of the negative wave growth rate parameter (c_β) of opposing-wind swells used in the wind stress model (both URI and Miami).

Closer examination of the wave spectra shows that the energy level of swell is also an essential factor in increasing the drag under opposing-wind swell conditions. Figs. 16j–16l show the wavenumber-direction spectra at $(R_{max}, -90°)$ in deep water and at 30 m water depth on two sloping bottoms. It is seen that the swell energy at 30 m depth with the steeper slope (1:200) is more energetic (due to shoaling) and more directed toward the shore (due to refraction) compared to that in deep water. In contrast, the swell energy at 30 m depth with the gentler slope (1:2000) is much lower because the dissipation of the

swell is more efficient on the gentler slope (swell propagates ten times longer distance in shallow water). This explains why the C_d enhancement is much stronger with the steeper slope.

3.4 Discussion and Conclusion

In this study, the effects of shoaling waves on the sea-state dependent wind stress and the drag coefficient (C_d) under landfalling TCs were investigated. Numerical experiments were conducted using idealized TCs with two intensities and two translation speeds, propagating toward and normal to the shoreline over two different bottom slopes. The shoaling wave spectra were simulated using the WW3 wave model, and the unresolved spectral tail (saturation level) was empirically parameterized and assumed to be unaffected by shoaling. The sea-state dependent wind stress was calculated using the two methods, URI and Miami.

The main findings of the study are summarized as follows:

1. Shoaling TC waves can significantly modify the wind stress and C_d in a complex manner compared to those in deep water. The modification is stronger over a steeper bottom slope and is further enhanced with a faster moving TC. The overall results are similar between the URI and Miami methods.

2. The wind stress magnitude (or C_d) is enhanced relative to that in deep water in the right (toward right-rear) quadrant due to shoaling of fetch-limited waves — similar to the results of the uniform wind experiments in Part I. The wind stress magnitude is also enhanced by shoaling of opposing-wind swells in the TC left (toward left-front) quadrant.

3. Over a steeper bottom the wind stress magnitude (or C_d) is reduced relative to that in deep water in the TC front (toward front-right) and real (toward rear-left) quadrants because wind seas are reduced due to the storm's proximity to the shoreline.

4. The variability of the drag coefficient at a given wind speed significantly increases due to shoaling waves, especially with a steeper bottom and a faster moving TC. However, the mean and median values of the drag coefficient are not significantly modified from those in deep water.

5. When dominant waves (swells) are misaligned with wind by less (more) than 90 degrees, the wind stress direction turns toward (opposite of) the dominant wave (swell) direction, hence, the 10-meter wind direction is misaligned with the wind stress direction. This misalignment angle significantly increases due to shoaling waves. The calculated misalignment angle is much larger with the Miami method than with the URI method.

Some of our results (e.g., increased C_d on the TC right attributed to shoaling wind waves, increased C_d on the TC left due to shoaling opposing-wind swells) are qualitatively consistent with those of *Chen and Curcic* (2016) who simulated landfall of two historical TCs. However, our study has further clarified how the shoaling wave effects on wind stress and C_d depend on the storm intensity, translation speed, and, importantly, on bottom slope. In addition, this study has provided detailed explanations as to why the shoaling wave effect on C_d significantly varies depending on the location relative to the storm center.

It is difficult to compare our model results with existing C_d observations under landfalling TCs in shallow water, mainly because such data are very scarce and the shoaling wave effect on C_d is very complex. The only statement that we can make at this time is that the large variability of C_d in shallow water found in this study is generally consistent with the C_d observations in landfalling TCs.

As discussed in Part I, the sea-state dependent stress calculations in our study are based on a set of strong assumptions. In particular, we have not included any explicit shallow water breaking wave effects, and we have assumed that the spectral tail level is not affected by shoaling. The validity of the first assumption is particularly questionable inside the surf zone. The second assumption means that the modification of the wind

stress reported here is solely due to the modification of the resolved part of the wave spectrum. Therefore, the shoaling wave effects on wind stress and C_d may be underestimated in this study. In addition, our estimates of the effect of opposing-wind swells may be correct only qualitatively, because the negative growth rate parameter of such waves is not well constrained.

Despite these shortcomings, this study strongly suggests that the wind stress and C_d can be significantly modified under landfalling TCs in shallow water. Hence, predictions of landfalling TCs and their impacts (e.g., storm surge) are likely affected by the modified wind stress and C_d as well.

REFERENCES

Ardhuin, F., et al. (2010), Semiempirical dissipation source functions for ocean waves. Part I: Definition, calibration, and validation, *Journal of Physical Oceanography*, *40*(9), 1917–1941, doi:10.1175/2010JPO4324.1.

Bell, M. M., M. T. Montgomery, and K. A. Emanuel (2012), Air-sea enthalpy and momentum exchange at major hurricane wind speeds observed during CBLAST, *Journal of the Atmospheric Sciences*, *69*(11), 3197–3222, doi:10.1175/JAS-D-11-0276.1.

Bi, X., Z. Gao, Y. Liu, F. Liu, Q. Song, J. Huang, H. Huang, W. Mao, and C. Liu (2015), Observed drag coefficients in high winds in the near offshore of the South China sea, *Journal of Geophysical Research*, *120*(13), 6444–6459, doi:10.1002/2015JD023172.

Black, P. G., E. A. D'Asaro, W. M. Drennan, J. R. French, P. P. Niiler, T. B. Sanford, E. J. Terrill, E. J. Walsh, and J. A. Zhang (2007), Air-sea exchange in hurricanes: Synthesis of observations from the coupled boundary layer air-sea transfer experiment, *Bulletin of the American Meteorological Society*, *88*(3), 357–374, doi:10.1175/BAMS-88-3-357.

Chen, S. S., and M. Curcic (2016), Ocean surface waves in Hurricane Ike (2008) and Superstorm Sandy (2012): Coupled model predictions and observations, *Ocean Modelling*, *103*, 161–176, doi:10.1016/j.ocemod.2015.08.005.

Donelan, M. A., M. Curcic, S. S. Chen, and A. K. Magnusson (2012), Modeling waves and wind stress, *Journal of Geophysical Research: Oceans*, *117*(7), doi:10.1029/2011JC007787.

Emanuel, K. A. (1986), An air-sea interaction theory for tropical cyclones. part i: Steady-state maintenance, *Journal of the Atmospheric Sciences*, *43*(6), 585–605, doi:10.1175/1520-0469(1986)043<0585:AASITF>2.0.CO;2.

Emanuel, K. A. (2003), A similarity hypothesis for air-sea exchange at extreme wind speeds, *Journal of the Atmospheric Sciences*, *60*(11), 1420–1428, doi:10.1175/1520-0469(2003)060<1420:ASHFAE>2.0.CO;2.

French, J. R., W. M. Drennan, J. A. Zhang, and P. G. Black (2007), Turbulent fluxes in the hurricane boundary layer. Part I: Momentum flux, *Journal of the Atmospheric Sciences*, *64*(4), 1089–1102, doi:10.1175/JAS3887.1.

Ginis, I. (2002), Tropical cyclone-ocean interactions, *Advances in Fluid Mechanics Series*, *33*, 83–114.

Grachev, A. A., C. W. Fairall, J. E. Hare, J. B. Edson, and S. D. Miller (2003), Wind stress vector over ocean waves, *Journal of Physical Oceanography*, *33*(11), 2408–2429, doi:10.1175/1520-0485(2003)033<2408:WSVOOW>2.0.CO;2.

Holland, G. J. (1980), An analytic model of the wind and pressure profiles in hurricanes., *Monthly Weather Review*, *108*(8), 1212–1218, doi:10.1175/1520-0493(1980)108<1212:AAMOTW>2.0.CO;2.

Holthuijsen, L. H., M. D. Powell, and J. D. Pietrzak (2012), Wind and waves in extreme hurricanes, *Journal of Geophysical Research: Oceans*, *117*(9), doi:10.1029/2012JC007983.

Hsu, J. Y., R. C. Lien, E. A. D'Asaro, and T. B. Sanford (2017), Estimates of surface wind stress and drag coefficients in Typhoon Megi, *Journal of Physical Oceanography*, *47*(3), 545–565, doi:10.1175/JPO-D-16-0069.1.

Hsu, J. Y., R. C. Lien, E. A. D'Asaro, and T. B. Sanford (2019), Scaling of Drag Coefficients Under Five Tropical Cyclones, *Geophysical Research Letters*, *46*(6), 3349–3358, doi:10.1029/2018GL081574.

Jarosz, E., D. A. Mitchell, D. W. Wang, and W. J. Teague (2007), Bottom-up determination of air-sea momentum exchange under a major tropical cyclone, *Science*, *315*(5819), 1707–1709, doi:10.1126/science.1136466.

Liu, Q., A. Babanin, Y. Fan, S. Zieger, C. Guan, and I. J. Moon (2017), Numerical simulations of ocean surface waves under hurricane conditions: Assessment of existing model performance, *Ocean Modelling*, *118*, 73–93, doi:10.1016/j.ocemod.2017.08.005.

Moon, I.-J., I. Ginis, T. Hara, H. L. Tolman, C. W. Wright, and E. J. Walsh (2003), Numerical simulation of sea surface directional wave spectra under hurricane wind forcing, *Journal of Physical Oceanography*, *33*(8), 1680–1706, doi:10.1175/2410.1.

Peng, S., and Y. Li (2015), A parabolic model of drag coefficient for storm surge simulation in the South China Sea, *Scientific Reports*, *5*(1), 15,496, doi:10.1038/srep15496.

Potter, H., C. O. Collins, W. M. Drennan, and H. C. Graber (2015a), Observations of wind stress direction during Typhoon Chaba (2010), *Geophysical Research Letters*, *42*(22), 9898–9905, doi:10.1002/2015GL065173.

Potter, H., H. C. Graber, N. J. Williams, C. O. Collins, R. J. Ramos, and W. M. Drennan (2015b), In situ measurements of momentum fluxes in typhoons, *Journal of the Atmospheric Sciences*, *72*(1), 104–118, doi:10.1175/JAS-D-14-0025.1.

Powell, M. D., P. J. Vickery, and T. A. Reinhold (2003), Reduced drag coefficient for high wind speeds in tropical cyclones, *Nature*, *422*(6929), 279–283, doi:10.1038/nature01481.

Reichl, B. G., T. Hara, and I. Ginis (2014), Sea state dependence of the wind stress over the ocean under hurricane winds, *Journal of Geophysical Research: Oceans*, *119*(1), 30–51, doi:10.1002/2013JC009289.

Sanford, T. B., J. F. Price, and J. B. Girton (2011), Upper-ocean response to hurricane frances (2004) observed by profiling EM-APEX floats, *Journal of Physical Oceanography*, *41*(6), 1041–1056, doi:10.1175/2010JPO4313.1.

Soloviev, A. V., R. Lukas, M. A. Donelan, B. K. Haus, and I. Ginis (2014), The air-sea interface and surface stress under tropical cyclones, *Scientific Reports*, *4*(1), 5306, doi:10.1038/srep05306.

Tolman, H. L., and D. Chalikov (1996), Source terms in a third-generation wind wave model, *Journal of Physical Oceanography*, *26*(11), 2497–2518, doi:10.1175/1520-0485(1996)026<2497:STIATG>2.0.CO;2.

Walsh, E. J., et al. (2002), Hurricane directional wave spectrum spatial variation at landfall, *Journal of Physical Oceanography*, *32*(6), 1667–1684, doi:10.1175/1520-0485(2002)032<1667:HDWSSV>2.0.CO;2.

Wright, C. W., E. J. Walsh, D. Vandemark, W. B. Krabill, A. W. Garcia, S. H. Houston, M. D. Powell, P. G. Black, and F. D. Marks (2001), Hurricane directional wave spectrum spatial variation in the open ocean, *Journal of Physical Oceanography*, *31*(8 PART 2), 2472–2488, doi:10.1175/1520-0485(2001)031<2472:hdwssv>2.0.co;2.

Zachry, B. C., J. L. Schroeder, A. B. Kennedy, J. J. Westerink, C. W. Letchford, and M. E. Hope (2013), A case study of nearshore drag coefficient behavior during hurricane ike (2008), *Journal of Applied Meteorology and Climatology*, *52*(9), 2139–2146, doi:10.1175/JAMC-D-12-0321.1.

Zhao, Z. K., C. X. Liu, Q. Li, G. F. Dai, Q. T. Song, and W. H. Lv (2015), Typhoon air-sea drag coefficient in coastal regions, *Journal of Geophysical Research: Oceans*, *120*(2), 716–727, doi:10.1002/2014JC010283.

Zheng, X., R. Mayerle, Y. Wang, and H. Zhang (2018), Study of the wind drag coefficient during the storm Xaver in the German Bight using data assimilation, *Dynamics of Atmospheres and Oceans*, *83*, 64–74, doi:10.1016/j.dynatmoce.2018.06.001.

MANUSCRIPT 4

Impact of Sea-State Dependent Wind Stress on Storm Surge

Xuanyu Chen[1*], Isaac Ginis[1], Tetsu Hara[1], and David Ullman[1]

Manuscript prepared for submission to Journal of Coastal Research

[1]Graduate School of Oceanography, University of Rhode Island, Narragansett, Rhode Island

[*]Corresponding author email: xychen@my.uri.edu

Abstract

This study investigates the impacts of sea-state dependent (SSD) wind stress on storm surge using a two-dimensional steady-state model and the Advanced Circulation (ADCIRC) model. The SSD wind stress is calculated using wave spectra simulated by the WAVEWATCH III (WW3) model under both steady uniform onshore wind and tropical cyclones (TC). In the steady onshore wind conditions, the SSD wind stress can increase the sea surface elevation by as much as 15% on a steep bottom slope compared to the result using the bulk wind stress as a function of wind speed. Next, the sensitivity of storm surge response to the SSD wind stress is investigated in idealized landfalling tropical cyclones. The results show that the differences in sea level simulated by the SSD stress and the bulk stress are sensitive to storm intensity, storm forward speed, storm size, and bottom slope. Larger differences are seen with more intense, faster-moving, and larger TCs that make landfall over a steeper bottom slope. The maximum impact of the SSD wind stress occurs to the left of the storm track near the radius of maximum wind (R_{max}) around the time of TC landfall. The set-down of the sea level is significantly enhanced due to increased offshore wind stress. However, the SSD wind stress impact on the peak surge to the right of the storm track is negligibly small. Hence, our analysis suggests that the SSD wind stress has the biggest impact in uniform onshore wind conditions (such as under large, slow moving extratropical cyclones) than in TC conditions. Our results also suggest that the water level prediction at the shoreline is sensitive to the wind stress in the surf zone, which is not resolved explicitly in our model.

4.1 Introduction

Storm surge, a natural hazard generated by tropical cyclones (TC) (hurricanes) and extratropical cyclones (e.g., Nor'easters in the eastern U.S.), frequently poses serious safety and economic threats to coastal communities worldwide. Studies have suggested that climate change and sea-level rise can increase the frequency of severe storm surge flooding in certain areas, for instance, New York City (*Lin et al.*, 2012; *Garner et al.*, 2017). The rising of sea level particularly increases the vulnerability of shallow marginal seas (e.g., the North Sea) to the storm surge due to nonlinear interactions (*Arns et al.*, 2017).Therefore, improving the storm surge models is of great importance not only for real-time forecast and hazard preparation but also for projecting and assessing the future risk of storm-surge flooding in different coastal areas.

Storm surge is scientifically defined as the abnormal rise of water level above the astronomical tide. The total surge can be a combination of wind-, pressure-, surface wave-, Coriolis-, and rainfall-induced components (*Harris*, 1963), where the Coriolis-induced surge is also commonly known as the forerunner (*Kennedy et al.*, 2011). Previous studies have shown that storm surge is sensitive to storm intensity, storm size (characterized by the radius of maximum wind), storm translation (or forward) speed, storm track orientation relative to the coast (angle of attack), and bottom slope (e.g., *Weisberg and Zheng*, 2006; *Irish et al.*, 2008; *Rego and Li*, 2009).Based on these studies, *Irish and Resio* (2010) developed the hydrodynamics-based storm surge scale, which estimates the storm surge potential, to assist hazard communication and public warning.

For given storm intensity, storm surges are most sensitive to the storm size (*Resio and Westerink*, 2008). Larger storms generate higher surges, especially on a wide and mildly sloping shelf with an intense TC (*Irish et al.*, 2008). The second most important parameter is the storm forward speed. It has been shown in multiple studies that the peak surge level increases with storm translation speed. *Irish et al.* (2008) show that a 50% increase in the forward speed leads to a 15%-20% increase in the peak surge. *Rego and Li* (2009) also find a similar response of the maximum surge to the forward speed.

Moreover, they show that faster storms reduce the maximum flooded volumes. The storm attack angle (or the storm track orientation) has also been shown to impact the peak surge magnitude but to a lesser extent (*Irish et al.*, 2008; *Ramos-Valle et al.*, 2020).

Ocean surface waves have been widely acknowledged to be an important factor affecting storm surge modeling (e.g., *Xie et al.*, 2008; *Dietrich et al.*, 2011; *Mao and Xia*, 2017).Ocean surface waves can influence storm surge mainly through three aspects: the wave radiation stress, the wave modified wind stress, and the wave modified bottom stress. The wave radiation stress is responsible for wave-setup and has been commonly included in the depth-integrated storm surge models (e.g., *Dietrich et al.*, 2011). The sum of the latter two stresses serves as the net driving force in these storm surge models. It is known that surface waves can modify both stresses by interacting with the atmospheric wind (e.g., *Janssen*, 1989; *Donelan et al.*, 1993; *Drennan et al.*, 2005) and the near-bottom ocean current (e.g., *Grant and Madsen*, 1979; *Soulsby et al.*, 1993). *Torres* (2017) have investigated the impact of wave-enhanced bottom stress (or bottom friction) parameterization on storm surge in Rhode Island coastal waters using the vertically-integrated ADCIRC model. In their study, the wave-induced enhancement in bottom friction is mainly determined by the ratio of near-bed wave orbital velocity to depth-averaged current velocity.

Some studies have suggested importance of a wave-dependent wind stress formulation for storm surge modeling (e.g., *Xie et al.*, 2003, 2008; *Chen and Curcic*, 2016; *Zheng et al.*, 2018). Using a three-dimensional coupled wave-ocean model, *Xie et al.* (2008) evaluated the individual and combined effects of the wave-age dependent wind stress, the wave-induced bottom stress, and the radiation stress on storm surge and inundation generated by Hurricane Hugo (1989) in the Charleston Harbor of South Carolina. They reported that the wave-age dependent wind stress (*Donelan et al.*, 1993) played a more significant role in affecting the peak surge and inundation area than the wave-induced bottom stress and the radiation stress.

Zheng et al. (2018) retrieved the optimal (bulk) wind drag coefficient for storm surge

simulation under storm Xavier in German Bight using the data assimilation method. They showed that the optimal wind drag coefficient is larger than the open ocean drag coefficient of *Smith* (1980) at all wind speeds. In addition, they suggested that the wave-age dependent surface roughness parameterization of *Donelan et al.* (1993) can explain the increase of the bulk drag coefficient and hence improve the storm surge modeling in the shallow seas. The wave-dependent wind stress in both these two studies was implicitly calculated based on the phase speed (or wave age) of the surface waves alone, which is not sufficient to fully account for the shoaling wave effect. Moreover, these two studies assumed that the wind stress is aligned with the wind speed, which is not the case in the presence of storm-generated swells (e.g., *Grachev et al.*, 2003).

Chen et al. (2020a) have investigated the shoaling-wave modified wind stress based on wave spectra simulated by the WAVEWATCH III (WW3) model, using two established sea-state dependent wind stress calculation methods (*Reichl et al.*, 2014; *Donelan et al.*, 2012). They show that the drag coefficient and wind stress vector can be significantly modified by water depth as the hurricane-generated ocean surface waves shoal during hurricane landfall. The results from this idealized numerical study are consistent with the nearshore wind stress variation of two historical hurricanes modeled in *Chen and Curcic* (2016). Hence, it is of interest to investigate whether the shoaling wave-modified wind stress, calculated from wave spectra, has an impact on storm surge modeling.

This study aims to investigate and quantify the impacts of sea-state dependent wind stress on storm surge modeling. We conduct idealized numerical experiments using a simplified ocean basin and idealized tropical cyclones. The experiments are focused on the shoaling-wave modified wind stress impact and do not include other surface wave impacts, such as the radiation stress and the wave modified bottom friction. The results of this process-based sensitivity study will be valuable for guiding the development of the state-of-the-art storm surge models.

4.2 Method

4.2.1 Steady State Surge Model

The following vertically-integrated primitive equations are commonly used to model storm surge in numerical models (*Luettich and Westerink*, 2004).

$$\frac{\partial \zeta}{\partial t} + \frac{\partial (UH)}{\partial x} + \frac{\partial (VH)}{\partial y} = 0 \tag{4.1}$$

$$\frac{\partial U}{\partial t} + U\frac{\partial U}{\partial x} + V\frac{\partial U}{\partial y} - fV = -g\frac{\partial}{\partial x}\left[\zeta + \frac{P_s}{g\rho_o} - \alpha\eta\right] + \frac{\tau_{sx} - \tau_{bx}}{\rho_o H} + \frac{M_x - D_x - B_x}{H} \tag{4.2}$$

$$\frac{\partial V}{\partial t} + U\frac{\partial V}{\partial x} + V\frac{\partial V}{\partial y} + fU = -g\frac{\partial}{\partial y}\left[\zeta + \frac{P_s}{g\rho_o} - \alpha\eta\right] + \frac{\tau_{sy} - \tau_{by}}{\rho_o H} + \frac{M_y - D_y - B_y}{H} \tag{4.3}$$

where ζ is the water surface elevation relative to the mean sea level, U,V is the depth-averaged velocity components, f is the Coriolis parameter, P_s is the surface pressure, α is the effective earth elasticity factor, η is the Newtonian equilibrium tidal potential, τ_s is surface wind stress, τ_b is bottom stress (or friction), M is vertically-integrated lateral stress gradient, D is momentum dispersion term, B is the vertically-integrated baroclinic pressure gradient, g is gravitational acceleration, ρ_o is reference density of sea water, $H = \zeta + h$ is the total water column thickness (a sum of the surface elevation and bathymetric depth).

We introduce the following assumptions:

i) The wind (speed) is steady, uniform, and blows onshore

ii) The bottom topography and the solution do not vary in the alongshore direction and there are no alongshore currents.

iii) The wind forcing is applied for a long period of time so that the solution reaches a steady state.

iv) The ocean is barotropic.

v) The tides and the surface pressure variation are ignored.

vi) The bottom stress, the lateral stress gradient, and the momentum dispersion are negligible compared to the wind stress

Then, the wind set-up can be estimated with a simplified momentum balance (Eq. (4.4)), where wind stress is only balanced by the cross-shore surface gradient. Note that the x axis is aligned with the onshore wind direction.

$$g\frac{\partial \zeta}{\partial x} = \frac{\tau_s}{\rho_o H} \tag{4.4}$$

$$\zeta\left(x_{i+1}\right) = \zeta\left(x_i\right) + \frac{\tau_x(x_i)}{\rho_o g\left[\zeta(x_i) + h(x_i)\right]}\left(x_{i+1} - x_i\right) \tag{4.5}$$

With this simplified balance, the effect of a shoaling wave-impacted wind stress on the surface elevation (ζ) can be evaluated using the finite difference method with the forward difference scheme (Eq. (4.5)). Note that the integration starts at an offshore boundary (x_o), which can be interpreted as the edge of the wind forced region, where the surface elevation is set zero.

4.2.2 Advanced Circulation Model (ADCIRC)

ADCIRC is a continuous-Galerkin, finite-element, shallow-water model (*Dietrich et al.*, 2011). The ADCIRC model can be run in the vertically-integrated (ADCIRC-2DDI) mode and in the fully three-dimensional mode (ADCIRC-3D). In this study, the storm-induced ocean circulation and sea surface elevation are simulated with ADCIRC-2DDI. The water surface elevation is solved from the continuity equation listed in Eq. (4.1) using the Generalized Wave Continuity Equation (GWCE) formulation (*Luettich and Westerink*, 2004). The depth-averaged current is solved from Eq. (4.2) and Eq. (4.3) without the momentum dispersion term D, which requires vertical profiles of the horizontal currents to evaluate (*Luettich and Westerink*, 2004).

In this study, we consider a barotropic coastal ocean (constant density) and do not consider the tide and the wave radiation stress for simplicity. Therefore, the ADCIRC are effectively solving the following horizontal momentum equations.

$$\frac{\partial U}{\partial t} + U\frac{\partial U}{\partial x} + V\frac{\partial U}{\partial y} - fV = -g\frac{\partial \zeta}{\partial x} - \frac{1}{\rho_o}\frac{\partial P_s}{\partial x} + \frac{\tau_{sx} - \tau_{bx}}{\rho_o H} + \frac{M_x}{H} \tag{4.6}$$

$$\frac{\partial V}{\partial t} + U\frac{\partial V}{\partial x} + V\frac{\partial V}{\partial y} + fU = -g\frac{\partial \zeta}{\partial y} - \frac{1}{\rho_o}\frac{\partial P_s}{\partial y} + \frac{\tau_{sy} - \tau_{by}}{\rho_o H} + \frac{M_y}{H} \tag{4.7}$$

ADCIRC is commonly forced by atmospheric wind and pressure fields. The wind stress is parameterized by a bulk parameterization as a function of wind speed using the drag coefficient (C_d) (Eq. (4.8)). The default drag coefficient used in the model follows *Garratt* (1977) formula, which describes the drag coefficient as a linear function of the wind speed (Eq. (4.9)). For forecasts or hindcasts of storm surge, a cap is usually applied to the Garratt formula to limit the drag coefficient at high winds.

$$\vec{\tau}_s = \rho_a C_d |\vec{U}_{10}| \vec{U}_{10} \tag{4.8}$$

$$C_d = 0.75 + 0.067 |\vec{U}_{10}| \tag{4.9}$$

In this study, the simulations with the bulk drag coefficient uses this Garratt formula with a cap of 0.0028 following *Ullman et al.* (2019). The simulations with the shoaling-wave impacted (sea-state dependent (SSD)) wind stress are carried out by forcing the ADCIRC model using wind stress instead of wind speed.

In this study, quadratic bottom friction law is used for bottom stress parameterizations with a spatially uniform bottom friction coefficient of 0.0025. Finite amplitude terms are included in the model run (a.k.a. $H = \zeta + h$); wetting and drying of elements is enabled with a default minimum velocity for wetting at 0.05 m/s. Horizontal eddy viscosity used in vertically-integrated lateral stress gradient term is set to 2.0 m^2/s.

4.2.3 WAVEWATCH III Model and Sea-State Dependent Wind Stress

The WAVEWATCH III (WW3) model predicts wave spectra by solving wave-action equation. The wind input term (S_{in}) and the white-capping term (S_{dis}) are computed with the ST4 physics parameterization (*Ardhuin et al.*, 2010). Four-wave interaction (S_{nl}) is computed with the standard discrete interaction approximation (DIA). In shallow water, the bottom friction (S_{btm}), the depth-induced breaking (S_{db}) , and the triad interaction (S_{tr}) are activated. The wave action equation is solved with these 6 source terms to generate wave spectra during shoaling and the settings of each source terms follow *Chen et al.* (2020b) (see Manuscript 2). Surface wave spectra are simulated on a structured grid using 40 frequency bins starting at 0.0125Hz with a logarithmic increment factor of 1.1, and 36 equally spaced directional bins.

In *Chen et al.* (2020b,a), the sea-state dependent wind stress calculation is performed using a complete wave spectrum, consisting of the WW3 spectrum in the resolved frequency range and the empirical saturation spectrum tail (B_{sat}) in the unresolved high frequency range. This empirical spectrum tail is assumed to be a function of 10-meter wind speed (U_{10}), and is determined so that the mean level of the sea-state dependent Cd agrees with a particular bulk formula. *Chen et al.* (2020b,a) chose the Geophysical Fluid Dynamics Laboratory (GFDL) hurricane model Cd (*Ginis et al.*, 2015) for their study, but they also showed that the shoaling wave modifications of the wind stress, namely, the Cd ratio ($r = Cd_{sh}/Cd_{deep}$) and wind stress direction (θ_τ), are almost independent of the bulk formula selected (see Fig. B.1). Therefore, in this study we determine the sea-state dependent wind stress $\vec{\tau}_s$ as

$$|\vec{\tau}_s| = \rho_a r C_d |\vec{U}_{10}|^2 \tag{4.10}$$

$$(\tau_{sx}, \tau_{sy}) = |\vec{\tau}_s| \, (\cos\theta_\tau, \sin\theta_\tau) \tag{4.11}$$

where C_d is the ADCIRC bulk formula (Garratt formula with a cap of 0.0028), and r and θ_τ are calculated following *Chen et al.* (2020b,a) using the spectral tail B_{sat} derived

for the GFDL Cd. In addition, *Chen et al.* (2020a) showed that the URI (*Reichl et al.*, 2014) and Miami (*Donelan et al.*, 2012) methods produce similar modification to the drag coefficient and the wind stress. Therefore, the investigation here uses only the URI method for wind stress calculation.

After the wind stress field is computed from the structured WW3 model, it is spatially interpolated on each node of the ADCIRC triangular mesh to force the ADCIRC model. The wind stress forcing is updated every half hour. We have confirmed that the magnitude of the surface elevation has not been significantly modified using a 15-min update frequency.

4.2.4 Idealized Tropical Cyclone Wind Field and Pressure Field

Idealized tropical cyclones are generated using the Holland model (*Holland*, 1980) and also a blended Holland-Rankine model (Eq. (4.12)). In the blended model, the wind profile within the radius of maximum wind (R_{max}) is constructed with the Holland model but the wind decay outside is modeled with the Rankine model. The purpose of using the Rankine model for wind outside R_{max} is to simulate storms of different sizes.

In the Holland model, the wind decay rate is controlled by the B parameter. It is determined by the maximum wind and the central pressure deficit (Δp) of the TC. Here, B is set to 2.0 for the Holland parametric TCs. In the Rankine model, the wind decay rate is controlled by the exponential factor n. For a pure Rankine vortex, $n = 1$ and for storms where surface friction is large, $n = 0.5$ is a typical value (*Holland et al.*, 2010) (Holland et al. 2010). We choose $n = 0.55$ for a large storm case because this value produces roughly the averaged R_{50kts} =300 km and R_{34kts} =750 km observed in the North-East quadrant of Hurricane Sandy (2012) when it turned toward the U.S. east coast and made landfall. We also choose n=1 for a small storm case. The effects of TC translation speed and inflow angle are added to the parametric wind field following *Chen et al.* (2020a) (See manuscript 3).

$$V(r) = \begin{cases} \left(\frac{AB\Delta p}{\rho r^B} e^{-A/r^B} \right)^{1/2} & 0 \le r \le R_{max} \quad (Holland) \\ \left(\frac{AB\Delta p}{\rho r^B} e^{-A/r^B} + \frac{r^2 f^2}{4} \right)^{1/2} - \frac{rf}{2} & r > R_{max} \quad (Holland) \\ V_{max} \left(\frac{R_{max}}{r} \right)^n, & r > R_{max} \quad (Rankine) \end{cases} \tag{4.12}$$

with,

$$A = R_{max}^B$$
$$\Delta p = \frac{\rho e V_{max}^2}{B}$$

The idealized pressure field of a TC can be derived from the Holland model as following:

$$P(r) = P_n - \Delta p \exp\left(\frac{r}{R_{max}} \right)^B \tag{4.13}$$

where, P_n is the environmental pressure set to 101200 Pa, r is the distance from the TC center, B is set to 2.0, ρ_a is the air density set to 1.15 kg/m^3.

4.2.5 Experimental Design

Idealized storm surge experiments are conducted in a simplified semi-circle ocean basin with a north-south oriented straight coastline and a constant bottom slope extending eastward, similar to the idealized ocean basin used in *Irish et al.* (2008). The semi-circle domain with a radius of about 1500 km is used to simulate the storm surge. This simulation domain is covered with an unstructured (triangular) mesh with 722,729 nodes and 1,432,762 elements. The resolution of the mesh increases from 160m at the land boundary (10m above mean sea level) to 50km at the eastern edge of the semi-circle domain. The triangulation of the mesh is constructed by the Surface-water Modeling System (SMS) software. On the land boundary, the node spacing within 750 km from the central latitude of the domain is set to 160 m uniformly. It is gradually increased outward to 1.1 km where the land boundary meets the outer open boundary. On the

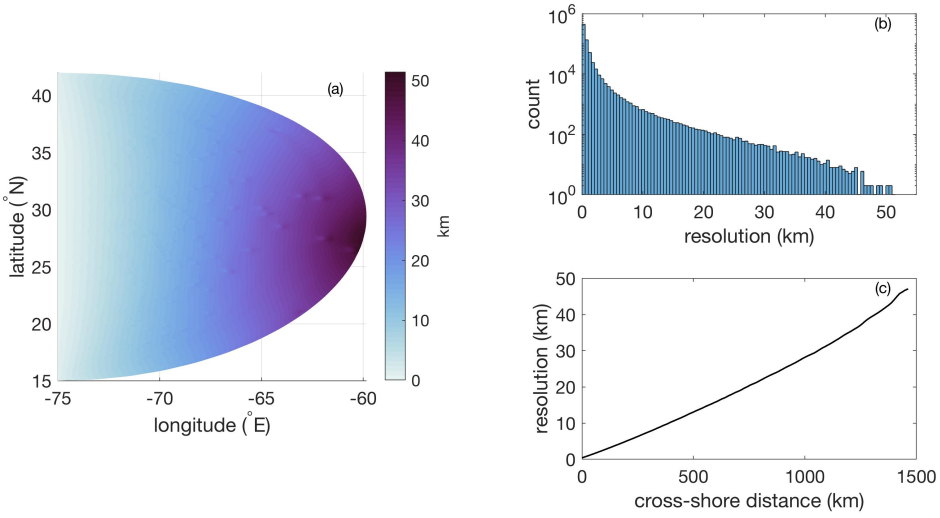

Figure 4.1: Averaged mesh resolution in the idealized semi-circle domain (panel a); Distribution of the averaged mesh resolution (panel b); averaged cross-shore variation of the mesh resolution (panel c).

curved open boundary, nodes are distributed in a way that the resolution increases from 1.1 km on the landside to 50 km offshore. Fig. 4.1 shows the averaged mesh resolution at each mesh node, its density distribution, and its averaged cross-shore variation. Zero normal flux and no slip conditions are used for the land boundary. A Sommerfield radiation condition is used at the curved open boundary allowing waves to propagate freely out of the domain.

Sensitivity experiments are designed to investigate the conditions at which the impact of the SSD wind stress on storm surge is the largest. The following geographical and meteorological parameters are varied in the sensitivity experiments: 1) the shelf slope, 2) storm intensity (defined by maximum wind speed), 3) storm size (measured by the radius of 34 kts wind R_{34kts}), 4) storm translation speed, and 5) angle between storm track and the coastline (storm attack angle).

All idealized TCs share the same R_{max} (70 km) but different R_{34kts}. The wind radial profiles in these TCs are shown in Figure Fig. 4.2. The TC with a 65 m/s maximum wind speed, 70 km radius of maximum wind with $R_{34kts} = 426km$, and moving at 10 m/s

normal to the coastline is designated as the base case scenario for atmospheric forcing. Variations of four storm parameters (see Table 4.1) from the base scenario are made to test the sensitivity of SSD wind stress effects on storm surge simulations. In addition, the storm surge responses to the SSD wind stress on a moderately gentle slope (1 : 2000) and a steep slope (1 : 200) are compared.

Table 4.1: TC parameters used in the sensitivity experiments

Scenario Number	Storm Intensity (V_{max})	Storm Size (R_{34kts})	Forward Speed (U_T)	Attack Angle (γ)
A	35 m/s (Cat. 1)	237 km (n=1.1)	2.5 m/s	45°
B	50 m/s (Cat. 3)	728 km (n=0.55)	5 m/s	135°
C	65 m/s (Cat. 5)	426 km (B=2.0)	10 m/s	90°

For a given experimental setting, a control case and an SSD case are conducted. In the control case, the simulation is forced with wind stress computed from the bulk method (Eq. (4.8), Eq. (4.9)) with the Cd capped at 0.0028. In the SSD case, the shoaling wave affected wind stress calculated from WW3 is used as forcing. (Noted that the WW3 model is forced by the same idealized TC wind field used to compute the bulk wind stress.) The differences in surface elevation between the control case and the SSD case quantify the impact of the SSD wind stress.

4.3 Results

4.3.1 Storm Surge Response in the Steady State Surge Model

The cross-shore surface elevation forced by the shoaling-wave impacted (sea-state dependent) wind stress (τ_{SSD}) is computed with the steady state model and compared to that generated by the bulk wind stress (τ_{BLK}). Fig. 4.3(a)-(c) demonstrates the shoaling-wave modified wind stress and the bulk wind stress on a 1:200 sloping bottom under 15 m/s, 35 m/s, and 65 m/s onshore winds with a 200 km fetch. Because the wind stress calculation methods do not explicitly resolve the surf zone, two possible scenarios for the surf-zone wind stress have also been investigated in addition to that computed from the URI method (SSD_{v0}). In scenario one (SSD_{v1}), the minimum wind stress in the surf

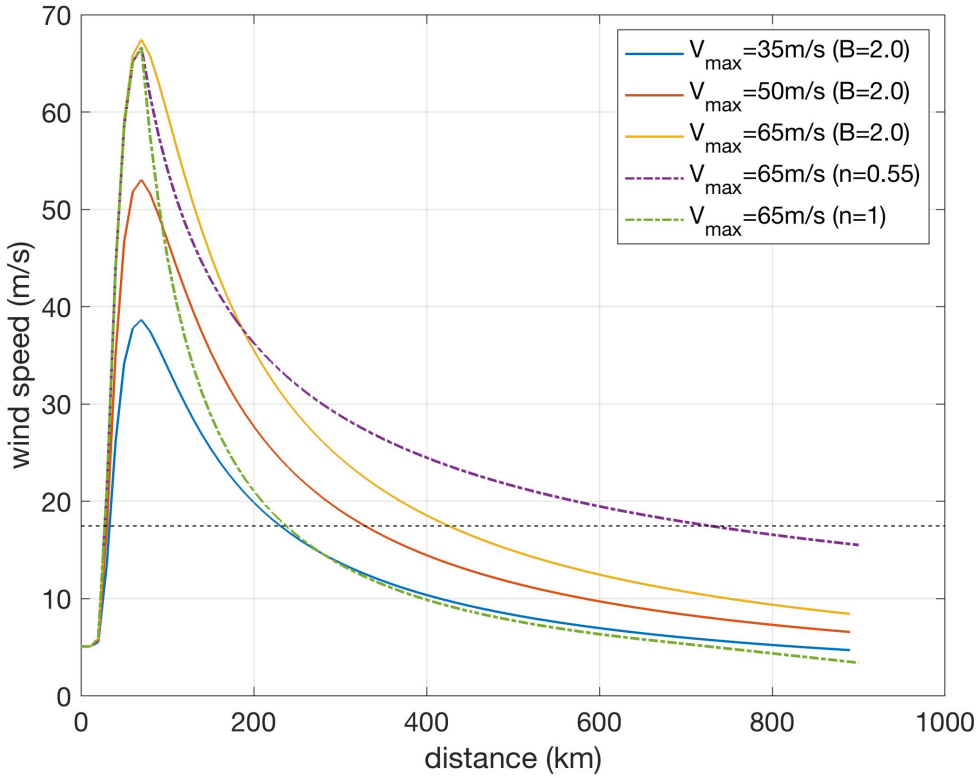

Figure 4.2: Wind radial profiles in five idealized TCs used in this study. Solid lines denote wind profiles generated from the Holland model; dash-dot lines denote wind profiles generated from the blended Holland-Rankine model. The dashed black line marks the level of the 34 kts (17.5 m/s) wind.

zone is set to the bulk level; in scenario two (SSD_{v2}), the maximum shoaling impact on the wind stress, which occurs just outside the surf zone, is kept inside the surf zone. Fig. 4.3(d)-(f) compares the surface elevation profiles generated with the different wind stress profiles at different wind speeds. The surface elevation increases monotonically with decreasing water depth as expected. As wind speed increases, the surge level at the shoreline increases, and its variation due to the different wind stress profiles also increases.

For easier comparison, the wind stress ratio (τ_{SSD}/τ_{BLK}) and the surface elevation ratio (ζ_{SSD}/ζ_{BLK}) between the SSD case and the bulk case are shown in Fig. 4.4. The surge response at the shoreline shows significant sensitivity to the wind stress behavior

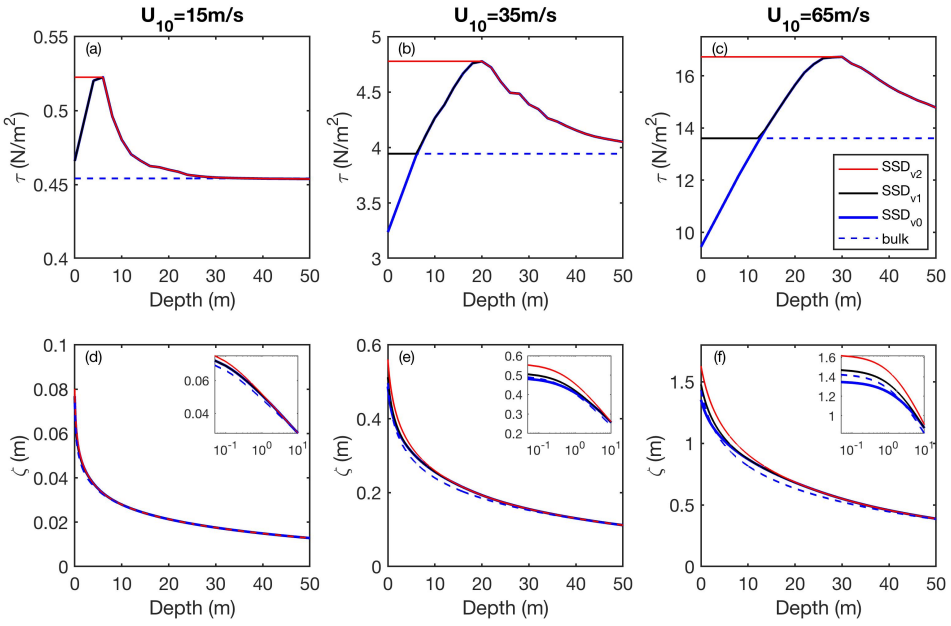

Figure 4.3: Cross-shore profile of the sea-state dependent wind stress and bulk wind stress (a–c), and the corresponding surface elevation (d–f) as a function of water depth on a 1:200 sloping bottom. The blue dashed lines mark the bulk wind stress and the associated surface elevation. Three versions of sea-state dependent (SSD) wind stress and the associated surface elevation are represented by solid lines with different colors. Blue solid lines: the wind stress is computed from the URI method. Black solid lines: the minimum SSD wind stress in the surf zone is set to the bulk value. Red solid lines: maximum enhancement of the wind stress due to shoaling waves is kept in the surf zone. In panel d to f, a sub-panel with a logarithmic x-axis is inserted to show the surface elevation below 10 m water depth.

inside the surf zone (Fig. 4.3d-f, Fig. 4.4d-f). When the maximum shoaling impact on the wind stress is kept inside the surf zone, the surface elevation ratio (relative to the bulk) continuously increases shoreward (red lines). However, if the wind stress is allowed to decrease from its maximum value in the surf zone (blue and black lines), the maximum surge ratio occurs at some distance offshore in the surf zone, instead of at the coastline. Therefore, in these two scenarios (SSD_{v0} and SSD_{v1}), the maximum impact of the shoaling enhanced wind stress does not occur at the coastline.

Furthermore, the variation of the surface elevation relative to the bulk results at the coastline depends on the extent to which the wind stress is decreased in the surf zone.

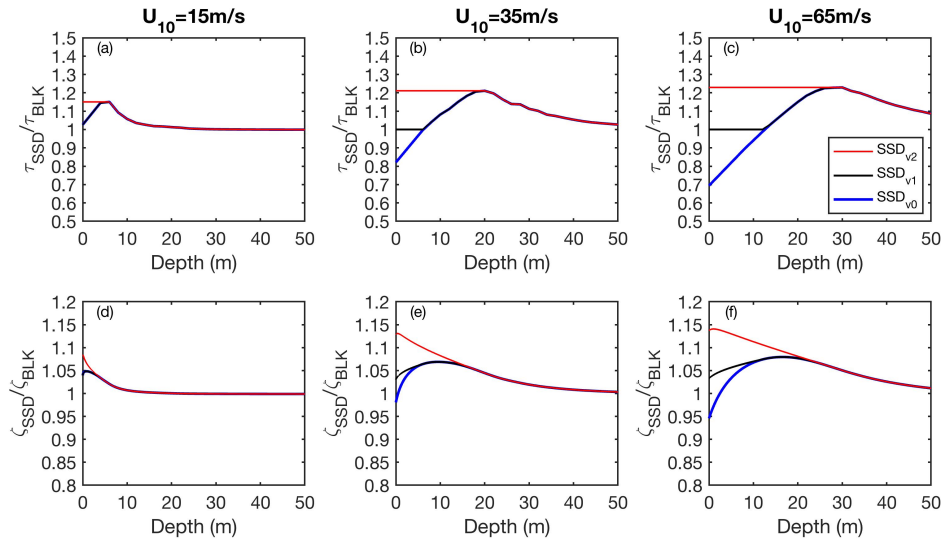

Figure 4.4: Ratio of sea-state dependent wind stress to the bulk wind stress (a–c) and the surface elevation ratio (d–f) as a function of water depth on a 1:200 sloping bottom. Blue, black and red solid lines represent three versions of the shoaling wave impacted wind stress in the surf zone as described in Fig. 4.3

When the SSD wind stress (τ_{SSD}) is applied, the surface elevation can be lower than its bulk counterpart when the SSD wind stress near the coastline is much lower (>20%) than its bulk value (Fig. 4.4c & f).

Fig. 4.5 shows the maximum surface elevation ratio in the surf zone under the three wind stress scenarios. The ratios are computed at 15m/s, 35m/s, 45m/s, 55m/s, and 65m/s wind speeds, with 200 km and 600 km fetch, and as a function of the bottom slope. The maximum impact of the SSD wind stress on surface elevation is sensitive to the bottom slopes in a similar manner as the maximum wind stress enhancement.

On a 1:200 bottom slope, the SSD cross-shore wind stress variation (calculated from URI method) can increase the surface elevation of the control case by as much as 5%∼15%, depending on the wind speed and the wind fetch (Fig. 4.5a). Setting the minimum wind stress to the bulk value in the surf zone does not change the maximum effect of the SSD wind stress (compare Fig. 4.5a & b). However, if the maximum shoaling impact on Cd applies everywhere in the surf zone (Fig. 4.5c), its maximum effect on storm surge is increased to 13%∼20%.

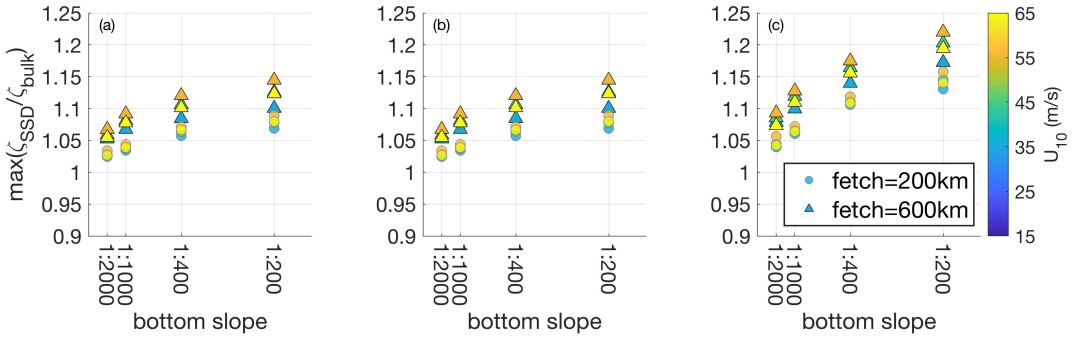

Figure 4.5: Maximum surface elevation ratio in the surf zone as a function of bottom slopes. Panel (a): surf-zone wind stress as it is computed from the URI wind stress method. Panel (b): the minimum value of the SSD surf-zone stress is set to the bulk value. Panel (c): wind stress is kept constant in the surf zone at the maximum level caused by shoaling waves.

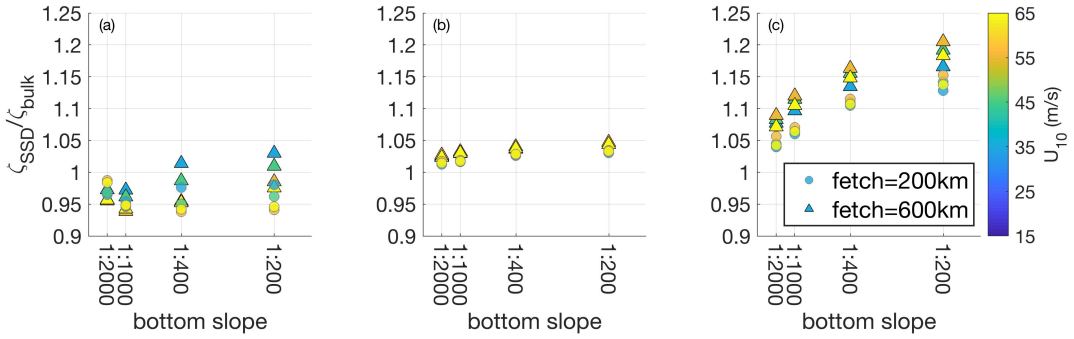

Figure 4.6: Surface elevation ratio at the shoreline (h=0) as a function of bottom slopes. Panel (a): surf-zone wind stress as it is computed from the URI wind stress method. Panel (b): the minimum value of the unmodified surf-zone stress profile is set to the bulk value. Panel (c): wind stress is kept constant in the surf zone at the maximum level caused by shoaling waves.

The surface elevation ratio at the shoreline, shown in Figure 4.5, is much more sensitive to wind stress variations in the surf zone. When Cd decreases in the surf zone

and is allowed to fall below its bulk value, the shoaling modified wind stress can lead to a -5%∼5% variation of the surface elevation (relative to the control case) on a 1:200 bottom slope (Fig. 4.6a). If the lower bound of the shoaling wave modified Cd is set to the bulk level in the surf zone, its effect on storm surge becomes less dependent on the wind and fetch conditions and is limited within 5% (Fig. 4.6b). However, if the Cd in the surf zone remains the same as the maximum Cd just outside the surf zone, the impact can be increased to 10∼20% (see Fig. 4.6c).

In summary, the steady state surge sensitivity experiments show that the SSD wind stress can significantly increase the surface elevation just outside the surf zone, where the maximum enhancement of Cd occurs due to shoaling waves. However, the surface elevation at the coastline can increase or decrease, depending on how the drag coefficient varies in the surf zone.

4.3.2 Storm Surge Response in the ADCIRC Model

4.3.2.a Sensitivity to bottom slope

The shoaling wave modifications on the wind stress strongly depend on the bottom slopes *Chen et al.* (2020b,a). Fig. 4.7 shows the time evolution of the SSD wind stress at different water depths on a 1:200 sloped bottom for the base case scenario (a TC with a 65 m/s maximum wind speed, 70 km radius of maximum wind, and moving at 10 m/s normal to the coastline). As the storm center passes over a given depth contour, the SSD wind stress is increased in the TC right-rear quadrants and left-front quadrants relative to the bulk wind stress. It is, however, reduced in the TC front (toward right) and rear (toward left) sectors compared to the bulk wind stress. This reduction is magnified as the TC approach closer to land until around 4 m bathymetric depth. As the water depth decreases from 30 m to 10 m, the increase of wind stress magnitude in the TC left-front sector is also strengthened and extended to a larger area. Then from 10 m to 2m, the wind stress magnitude in this region starts to reduce. In contrast, as water depth decreases from 30 m to 2 m, the wind stress enhancement in the right-rear sector

reduces monotonically as the enhancement region shifts outward to a lower wind speed area. This quadrant-dependent modifications on the wind stress magnitude and their depth variations are consistent with those reported in *Chen et al.* (2020a). Note, waves are unresolved below 2 m by the WW3 structured grid used in this study.

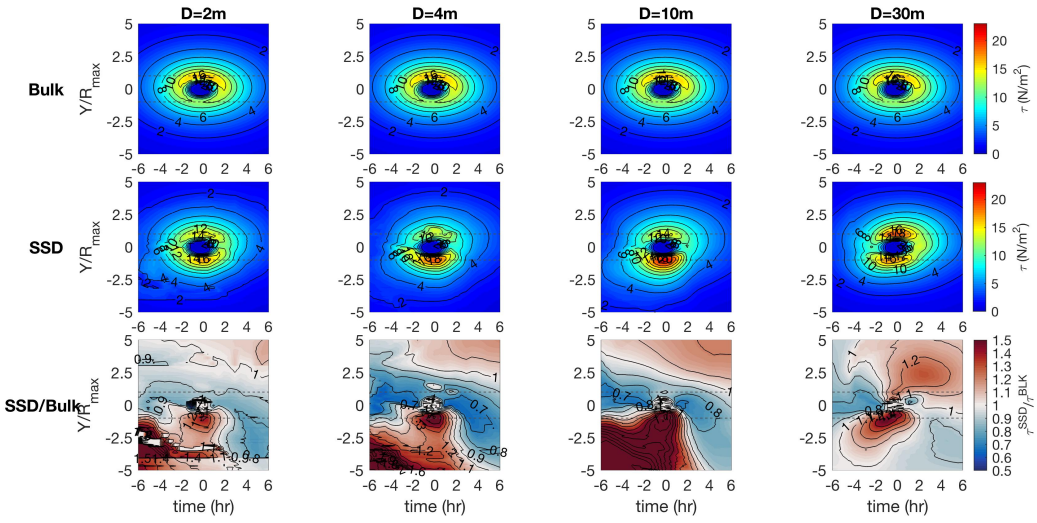

Figure 4.7: Spatial-temporal variation of the bulk wind stress (1^{st} row), the sea-state dependent wind stress (2^{nd} row), and the ratio between them (3^{rd} row) at various water depth with the 1:200 bottom slope. The wind stress contours are drawn every 2 N/m^2. The increment of the contours for Cd ratio is 0.1. The x-axis shows time relative to when the TC center arrives at the given depth contour. The y-axis shows the along-shore distance relative to the TC track normalized by R_{max}. The thin dotted lines denote R_{max} and -R_{max}.

The alongshore and temporal variations of sea surface elevation in the bulk case and the SSD case are compared at four water depths in Fig. 4.8. In both cases, the local water level to the right of the storm track peaks when the TC center arrives at the given water depth. Meanwhile, the local water level to the left of the storm track recedes, creating the "negative surge". The maximum storm surge and the maximum negative surge occur around R_{max} and -R_{max}, respectively. Overall, the magnitude of the sea-level change at R_{max} is larger than that at -R_{max}. The maximum surge difference between the SSD case and the control case occurs to the left of the TC track where the negative surge is generated. To the right of the storm track where the storm surge is significant, the

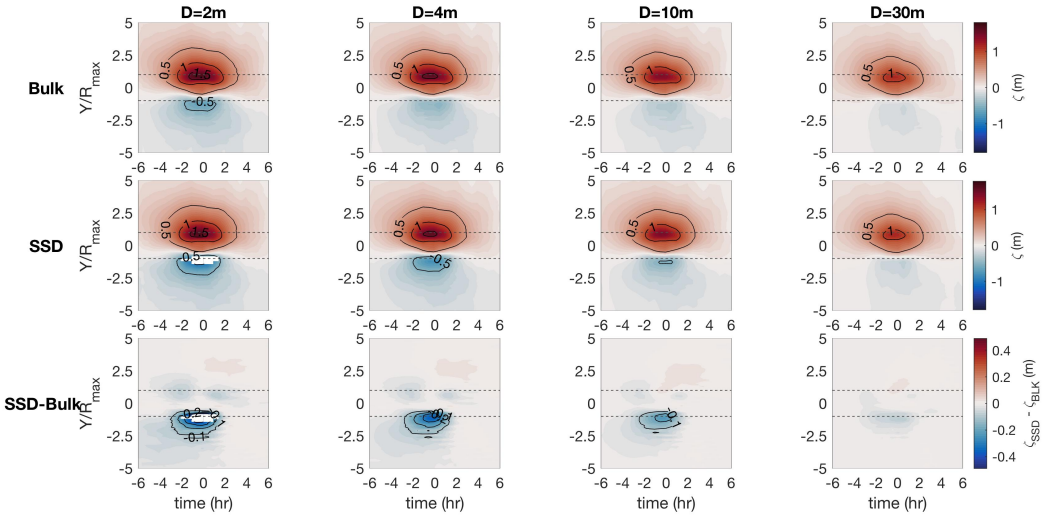

Figure 4.8: Spatial-temporal variation of the sea surface elevation generated by the bulk wind stress (1^{st} row), by the sea-state dependent wind stress (2^{nd} row), and the elevation ratio between the two cases (3^{rd} row) at various water depth with the 1:200 bottom slope. The sea surface elevation contours are drawn every 0.5 m. The increment of the ratio contours is 0.1. The x-axis shows time relative to when the TC center arrives at the given depth contour. The y-axis shows the along-shore distance relative to the TC track normalized by R_{max}. The thin dotted lines denote R_{max} and -R_{max}.

impact of the SSD wind stress is rather small (<0.1m). Note that the blank area at 1 m and 2 m around -R_{max} indicates that the offshore blowing TC wind has drained the water at those two depths.

On a moderately gentle slope (1:2000), the shoaling ocean surface waves impose weaker impacts on wind stress (compare Fig. 4.7 and Fig. 4.9). Relative to the bulk wind stress, the shoaling induced variations of the wind stress magnitude is overall smaller compared to those on the 1:200 sloped bottom. Meanwhile, the maximum storm surge is 3 to 4 times higher than that generated on the steep slope(see Fig. 4.8 and Fig. 4.10). Therefore, even though the surface elevation difference between the control and SSD cases is of the same order of magnitude as that on the steep slope, the relative impact of SSD wind stress on storm surge is much smaller with a gentle bottom slope.

The SSD stress impacts can be seen more clearly by comparing the surface elevation time series on both slopes at different bathymetric depths (Fig. 4.11). With the 1:200

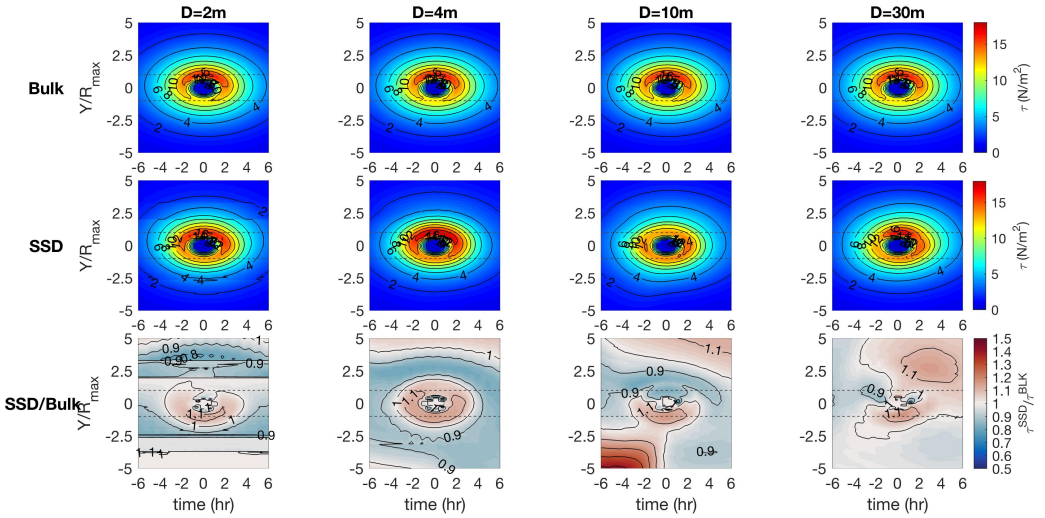

Figure 4.9: Same as Fig. 4.7, but on a 1:2000 sloped bottom.

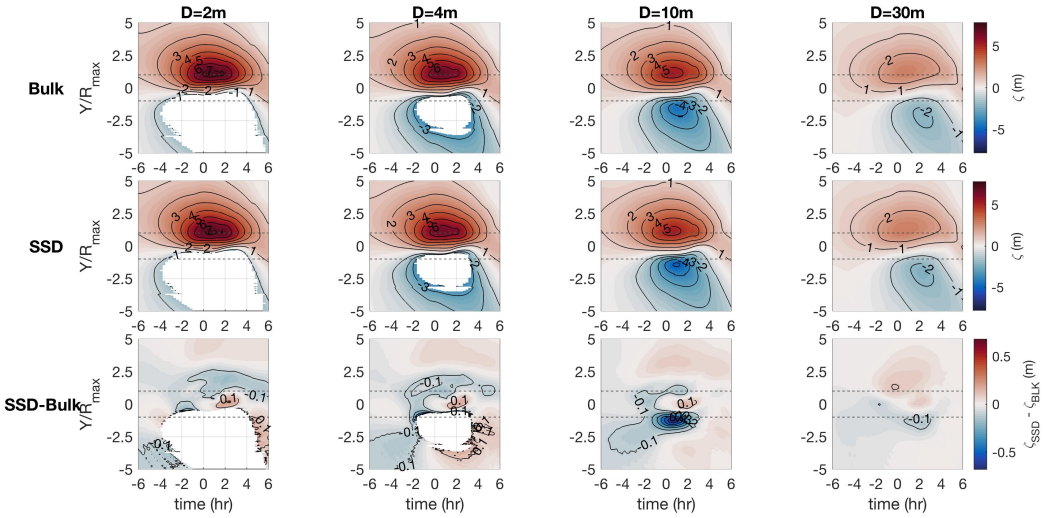

Figure 4.10: Same as Fig. 4.8, but on a 1:2000 sloped bottom.

bottom slope, the maximum reduction of water level to the left of the storm track (at -R_{max}) is enhanced by the SSD wind stress by almost 100% relative to that generated by the bulk wind stress (Fig. 4.11a–c). With the 1:2000 bottom slope, the relative change from the control case is only about 14% at 10 m water depth, even though the absolute difference (∼0.5 m) between the SSD and the bulk case is slightly larger than those on

the 1:200 slope (∼0.2–0.3m). Regardless of the bottom slopes, the SSD wind stress plays a negligible role in affecting the storm surge to the right of the storm track. For the rest of this section, we focus on analyzing experiments conducted on the 1:200 slope.

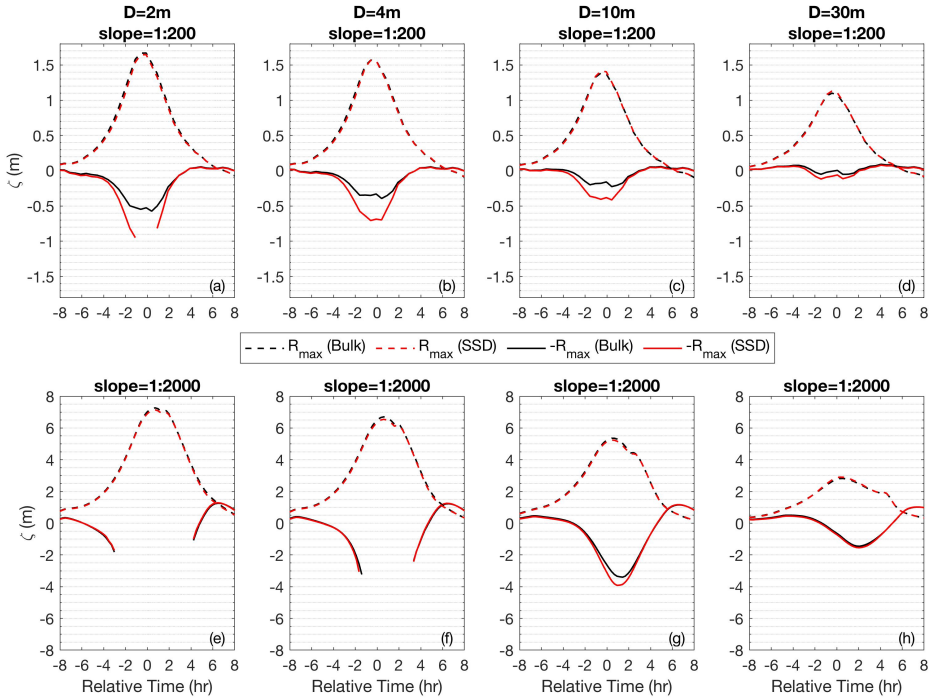

Figure 4.11: Time series of surface elevation at various depths at R_{max} to the right (dashed lines) and at R_{max} to the left (solid lines) of the storm track. Black lines denote results generated with the bulk wind stress; red lines denote results generated with the sea-state dependent wind stress. The upper and lower four panels show the time series from 1:200 and 1:2000 bottom slope, respectively.

4.3.2.b Sensitivity to Storm Parameters

In this subsection, we use the surface elevation time series taken along the 2 m depth contour (on the 1:200 slope) at $\pm R_{max}$ from the storm track (for storms with a perpendicular track relative to the coastline) or at $\pm R_{max}$ from the intersection between the storm track and the 2 m isobath (for storms with an oblique track) as a proxy to describe the storm surge characteristics and the impacts of the SSD wind stress on storm surge simulation.

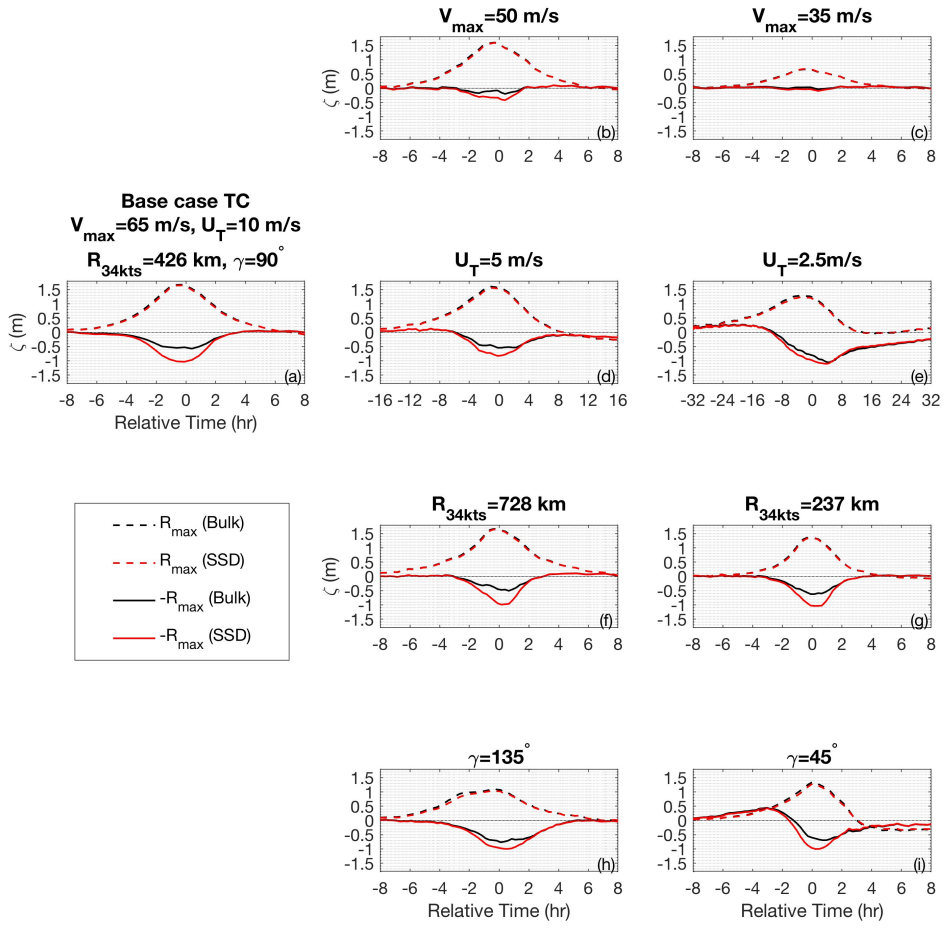

Figure 4.12: Comparison of the sea surface elevation time series extracted at 2m water depth from 9 TC scenarios. The title of panel b to g lists the parameter that is varied from the base TC scenario (panel a). Line color marks the control case (black) and the sea-state dependent case (blue). Dashed (solid) lines represent results from R_{max} on the right (left) side of the storm track. The thin dotted line marks the level of zero. Note that the time axis (x-axis) in panel d and e is stretched to account for the slower forward speed.

Fig. 4.12a to Fig. 4.12c compare the water level time series under TCs with different intensity. As the storm intensifies from 35 m/s to 65 m/s, the magnitude of the positive surge at R_{max} and the negative surge at -R_{max} increases. Like previous results, the SSD wind stress impact on the surge level at R_{max} is minimal but it appears to be more

significant on the negative surge. The absolute water level difference at -R_{max} between the SSD case and the bulk case increases for more intense storms due to the higher offshore wind speed. Note that the storm intensity does not significantly change the ratio between the SSD wind stress and the bulk wind stress.

Figs. 4.12a, 4.12d, and 4.12e the sensitivity of the storm surge response to the SSD wind stress to the storm forward speed. As the storm slows down, the time series of surface elevation become less symmetric before and after the arrival of the storm center. At R_{max}, the water level starts increasing one day before TC landfall when the forward speed is the slowest at 2.5 m/s. The sea-level rise during this period is caused by the shoreward Ekman transport induced by the southward wind in the TC front sector (explained in Kennedy et al. (2011)). This Coriolis-induced setup also affects the water level at -R_{max} one day before the TC landfall. However, SSD wind stress does not have a significant impact on this process.

After TC landfall, it takes about 8 hours for the sea level at R_{max} to return to the still water level (0 m) in all three forward speed scenarios. At -R_{max}, however, the adjustment time is longer for a slower TC. In addition, the trough of the sea level at -R_{max} starts to lag the peak of the sea level at R_{max} as the TC moves slower. Overall, the impacts of the SSD wind stress on the sea level at -R_{max} decrease as the landfalling storm slows down.

Figs. 4.12a, 4.12f and 4.12g test the sensitivity of the SSD impacts to storm size, measured by R_{34kts} in this study. When the R_{34kts} is 728km (the Sandy-type TC), the maximum storm surge is higher than that produced by a smaller one (Fig. 4.12g). (Also, the storm surge affected area is larger for the Sandy-type TC, not shown). However, the impact of SSD wind stress remains insignificant. The negative surge magnitude at -R_{max} is not affected by the size of the TC. Therefore, the difference between the SSD and the bulk cases is less sensitive to the R_{34kts} compared to the storm intensity and storm translation speed.

As the storm attack angle changes from 90° to more oblique angles (135° and 45°),

the time series of sea level at $\pm R_{max}$ changes its shape. With the 135° attack angle, which is measured counterclockwise from the due north, the right-hand side of the TC approaches the coastline first, the surge level at R_{max} is slightly lower 2∼4 hours before TC landfall in the SSD case compared to that in the bulk case (Fig. 4.12h). The difference in the water level at -R_{max} between the SSD case and the bulk case is slightly reduced compared to that in the scenario with 90° attack angle. When the attack angle is 45°, the storm travels from southeast to northwest, and the wind on the left-hand side of the TC affects the coast first. There is a rise of the water level at -R_{max} before the TC landfall (Fig. 4.12i) similar to that in the 2.5 m/s translating TC (Fig. 4.12e). This is likely caused by a combination of the Coriolis-setup and wind-induced set-up. Although the TC forward speed is not changed, changing the land approach angle increases the distance traveled by a TC before landfall and effectively reduces the translation speed. Also, in this attack angle scenario, the wind in front of the TC blows onshore and hence can generate wind set-up. However, the SSD wind stress does not show any effects on the storm surge simulation in this early period. In general, the differences between the SSD case and the bulk case are not sensitive to the attack angle at -R_{max}. At R_{max}. Even though still minimal, the effect of the SSD wind stress on water level becomes slightly larger with an oblique storm track than with the perpendicular storm track.

Fig. 4.13 summarizes the sensitivity experiments using the maximum absolute difference in surface elevation between the SSD cases and the bulk cases evaluated at 2 m water depth. Overall, we see that using SSD wind stress affects the water level to the left of the storm track to a greater degree than that to the right. The impact of the SSD wind stress on the water level solution at -R_{max} is more sensitive to the storm intensity and forward speed than to the storm size and attack angle. The SSD wind stress creates a larger reduction of water level to the left of the storm track when the TC is more intense (larger maximum wind), moves perpendicular to the coast with a faster forward speed, and is larger (larger R_{34kts}).

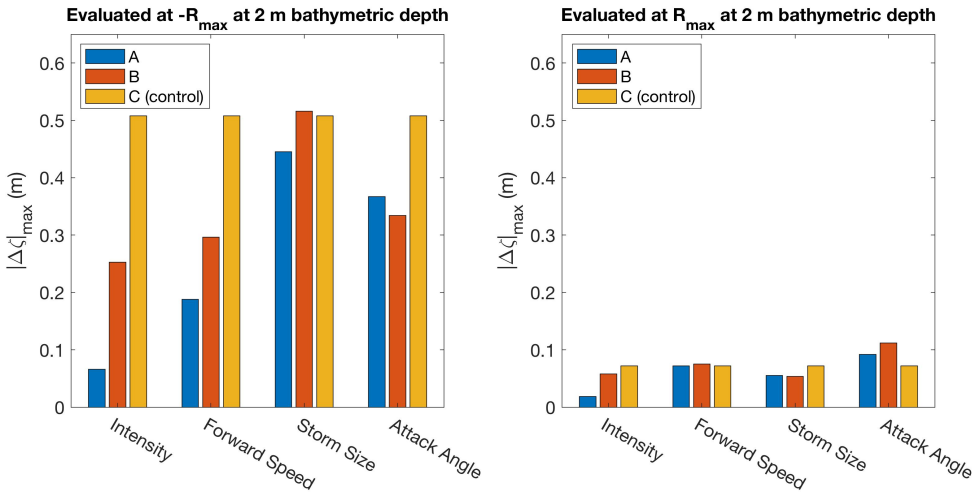

Figure 4.13: Sensitivity of the maximum absolute differences in the surface elevation between the SSD case and the bulk case to four groups of TC parameters. . Left and right panels show sensitivity evaluated from locations at R_{max} to the left and right side of the TC track respectively. Scenarios A, B, C correspond to scenarios in each parameter group noted in Table 4.1.

4.3.2.c Sensitivity to the Wind Stress in the Surf Zone

Two other experiments are conducted to test the sensitivity of water level response to the wind stress in the surf zone using the base TC scenario on the 1:200 bottom slope. Fig. 4.4c shows that the SSD drag coefficient may be enhanced by about 20% under steady strong onshore wind just outside the surf zone. A similar condition of strong onshore wind occurs to the right of the storm track, and the SSD drag coefficient is also enhanced by about 20% (Fig. 4.7 right bottom panel). Motivated by these observations, in the first test, the SSD wind stress in the surf zone (<30 m) is set to be 1.2 times the bulk wind stress value regardless of the sea states. In the second test, the wind stress is set to be 1.1 times the bulk value at all depths for wind speed larger than 30 m/s, which is roughly equivalent to raising the cap of Cd by 10%. Fig. 4.14 compares the change of surface elevation of these two test cases from the bulk case. When the wind stress in the surf zone is increased by 20% relative to the bulk value uniformly the surface elevation to the right of the storm track around R_{max} is increased by 0.1 m (∼10% increase) (Fig. 4.14

middle row). This is of similar magnitude generated by raising the Cd by 10% for high winds (>30 m/s) (Fig. 4.14 bottom row).

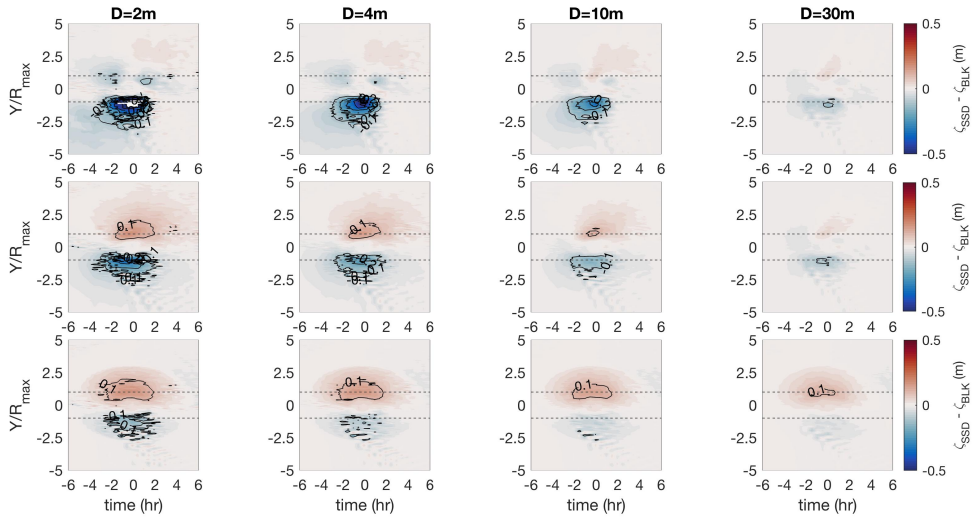

Figure 4.14: Surface elevation differences between three test wind stress cases and the bulk case under the base TC scenario (W_{max} =65 m/s, U_T =10m/s, $\gamma = 90°$, $B = 2.0$) at 4 water depths. Top row: unmodified SSD wind stress in the surf zone; middle row: SSD wind stress at water depth below 30 m is modified to 1.2 times the bulk wind stress; bottom row: the bulk wind stress is raised by 10% at all water depth for wind speed larger than 30m/s.

4.4 Discussion

The sea level simulations with idealized TCs consistently show that the shoaling-wave modified wind stress impacts storm surge on the left side of the storm track where winds blow offshore. This result is qualitatively consistent with *Xie et al.* (2008)'s study under Hurricane Hugo (1989), a Category 4 storm making landfall at about 10 m/s forward speed. They reported that the simulated storm surges using their wave-surge coupled model at sites to the left of the storm track are generally more accurate than those simulated by their stand-alone surge model. They further attributed the decrease of the sea level mainly to the enhanced offshore wind stress induced by waves. However, the enhanced offshore wind stress is generated by different mechanisms, decreased wave age

or slower wave phase speed in their study and wind opposing shoaling swell in this study.

Our results show no significant changes in the surge level on the right side. This contradicts the results from *Xie et al.* (2003, 2008), who find the SSD stress impacts on the peak surge are on the same order of magnitude as those in the negative surge. This difference may be due to the sensitivity of the storm surge at the shoreline to the wind stress in the surf zone. *Xie et al.* (2003, 2008) simply applied the wave-age dependent roughness parameterization of *Donelan et al.* (1993) in the surf zone and predicted the largest increase in wind stress at the minimum water depth (near the shoreline). However, the used wave-age dependent formulation is not derived for the surf zone application and is not expected to be valid where the wave age is very small. Our method of the SSD wind stress calculation, based on a linear superposition of the form drag due to spectral wave components, is also expected to be less accurate in the surf zone where waves are continuously breaking and very nonlinear. In fact, we have demonstrated in Section 4.3.2.c that different assumptions of the SSD stress in the surf zone can lead to large uncertainty of the storm surge at the shoreline. Clearly, further investigations focused on the wind stress in the surf zone is needed to improve our storm surge predictions at the shoreline.

Under the steady and spatially uniform onshore wind conditions, the impacts of the shoaling wave-modified wind stress on storm surge evaluated by the maximum storm surge ratio ($\frac{\zeta_{SSD}}{\zeta_{Bulk}}$) can reach as much as $\sim$15% on a 1:200 sloped bottom (Fig. 4.5a). Under TC conditions, however, the maximum surge ratio in the storm surge affected region to the right of a TC never exceeds 5%. This difference is likely caused by different forcing durations. We have assumed that the surge generated in the steady uniform wind cases reaches a steady-state. However, in the hurricane condition, the constant wind forcing duration experienced at a particular location is limited, and the surge may never reach such a state. The wind stress forcing duration can be evaluated by the characteristic storm duration ($t_* = R_{max}/U_T$) introduced in *Irish and Resio* (2010). The slower the TC, the longer the characteristic storm duration. However, the shoaling wave

impacts on the wind stress is reduced with the reduced TC forward speed. Therefore, the combination of these two conflicting factors limit the effect of the SSD wind stress on the storm surge under a moving tropical cyclone.

Extratropical cyclones, which are several times larger in size, can produce conditions that are more similar to the steady uniform onshore wind conditions. Therefore, the shoaling wave modification on the wind stress may be more important for the storm surge modeling under extratropical cyclones (nor'easters) rather than under tropical cyclones.

From a practical modeling perspective, our results here suggest that uncertainty in the wind stress parameterization due to shoaling waves nearshore introduces changes in water level prediction at the coastline by up to 15%∼20%. Other sources of errors (e.g., wind speed product and bottom shear stress) can have significant influence on the accuracy of storm surge prediction as well. *Torres et al.* (2019) report that an inaccurate wind product can lead to a 50% error in storm surge and wave predictions. In the surf zone, when near-bottom current flows offshore, the bottom shear stress acts in the same direction as the wind stress and increases the storm surge. But to our knowledge, the magnitude of bottom stress in the surf zone is not well constrained by observation. Hence, it is difficult to gauge the uncertainty in the bulk bottom stress parameterization and the associated errors in storm surge simulations. Nonetheless, it has been reported that the wave-dependent wind stress has a larger effect on storm surge than the wave-dependent bottom stress (*Xie et al.*, 2003, 2008). *Torres* (2017) found negligible impacts of wave-dependent bottom stress on storm surge simulations using the depth-averaged ADCIRC model. Therefore, it is likely that uncertainties in the atmospheric wind forcing (wind speed and drag coefficient) is the most significant source of error for storm surge modeling under tropical cyclones.

4.5 Conclusion

In this study, the impacts of the sea-state dependent (SSD) wind stress on storm surge are investigated. The SSD wind stress is calculated using the wave spectrum simulated

by the WW3 model. The impacts of the SSD wind stress in steady uniform onshore wind conditions are evaluated with a steady state surge model. Surges with several idealized TC and bathymetry scenarios are simulated using the ADCIRC model to examine the sensitivity of the SSD stress impact to different environmental and TC parameters.

The main results can be summarized as follows:

i. Under steady uniform onshore wind, the SSD wind stress can increase the water level just outside the surf zone by as much as 15% compared to the prediction using the bulk wind stress. However, the water level at the shoreline is sensitive to different assumptions of the wind stress in the surf zone.

ii. In the TC conditions, the SSD wind stress may significantly increases the magnitude of sea-level reduction ("negative surge") to the left of the storm track, especially at a distance around R_{max} from the TC center (by $\sim$100%).

iii. The SSD wind stress has minimal impacts ($<$5%) on the surge prediction to the right of a TC, where the TC wind blows onshore.

iv. The impact of SSD wind stress on storm surge is larger with a steeper bottom slope in both the steady uniform onshore wind and the tropical cyclone conditions.

Our analysis suggests that the SSD wind stress is more important in uniform onshore wind conditions (such as under large and slow moving extratropical cyclones) than in TC conditions. Our results also suggest that the water level prediction at the shoreline is sensitive to the wind stress in the surf zone, which is still poorly constrained and is not well predicted in our model.

Although we do not expect varying coastline geometry would significantly increase the effect of sea-state dependent wind stress on storm surge, future work can examine this aspect using various idealized coastline configurations (e.g., *Kouhi and Hashemi*, under revision) that better represent the real-world conditions. To validate the results and findings from this idealized study, hindcasts of storm surge generated by tropical

cyclones and extratropical cyclones will be conducted using sea-state dependent wind stress in a future study.

REFERENCES

Ardhuin, F., et al. (2010), Semiempirical dissipation source functions for ocean waves. Part I: Definition, calibration, and validation, *Journal of Physical Oceanography*, *40*(9), 1917–1941, doi:10.1175/2010JPO4324.1.

Arns, A., S. Dangendorf, J. Jensen, S. Talke, J. Bender, and C. Pattiaratchi (2017), Sea-level rise induced amplification of coastal protection design heights, *Scientific Reports*, *7*(1), 40,171, doi:10.1038/srep40171.

Chen, S. S., and M. Curcic (2016), Ocean surface waves in Hurricane Ike (2008) and Superstorm Sandy (2012): Coupled model predictions and observations, *Ocean Modelling*, *103*, 161–176, doi:10.1016/j.ocemod.2015.08.005.

Chen, X., I. Ginis, and T. Hara (2020a), Impact of shoaling ocean surface waves on wind stress and drag coefficient in coastal waters: Part ii tropical cyclones, *Journal of Geophysical Research: Oceans*, *n/a*(n/a), doi:10.1029/2020JC016223.

Chen, X., T. Hara, and I. Ginis (2020b), Impact of shoaling ocean surface waves on wind stress and drag coefficient in coastal waters: Part i uniform wind, *Journal of Geophysical Research: Oceans*, *n/a*(n/a), doi:10.1029/2020JC016222.

Dietrich, J. C., et al. (2011), Modeling hurricane waves and storm surge using integrally-coupled, scalable computations, *Coastal Engineering*, *58*(1), 45–65, doi:10.1016/j.coastaleng.2010.08.001.

Donelan, M. A., F. W. Dobson, S. D. Smith, and R. J. Anderson (1993), On the dependence of sea surface roughness on wave development, *Journal of Physical Oceanography*, *23*(9), 2143–2149, doi:10.1175/1520-0485(1993)023<2143:OTDOSS>2.0.CO;2.

Donelan, M. A., M. Curcic, S. S. Chen, and A. K. Magnusson (2012), Model-

ing waves and wind stress, *Journal of Geophysical Research: Oceans*, *117*(7), doi: 10.1029/2011JC007787.

Drennan, W. M., P. K. Taylor, and M. J. Yelland (2005), Parameterizing the sea surface roughness, *Journal of Physical Oceanography*, *35*(5), 835–848, doi:10.1175/JPO2704.1.

Garner, A. J., et al. (2017), Impact of climate change on New York City's coastal flood hazard: Increasing flood heights from the preindustrial to 2300 CE, *Proceedings of the National Academy of Sciences of the United States of America*, *114*(45), 11,861–11,866, doi:10.1073/pnas.1703568114.

Garratt, J. R. (1977), Review of Drag Coefficients over Oceans and Continents, *Monthly Weather Review*, *105*(7), 915–929, doi:10.1175/1520-0493(1977)105<0915:rodcoo>2.0.co;2.

Ginis, I., M. Bender, B. Thomas, M. Morin, V. Tallapragada, and A. Soloviev (2015), A new drag coefficient formulation and its impact on the gfdl and hwrf hurricane model predictions, 19th Conference on Air-Sea Interaction, Phoenix, AZ, January 4-8.

Grachev, A. A., C. W. Fairall, J. E. Hare, J. B. Edson, and S. D. Miller (2003), Wind stress vector over ocean waves, *Journal of Physical Oceanography*, *33*(11), 2408–2429, doi:10.1175/1520-0485(2003)033<2408:WSVOOW>2.0.CO;2.

Grant, W. D., and O. S. Madsen (1979), Combined wave and current interaction with a rough bottom, *Journal of Geophysical Research: Oceans*, *84*(C4), 1797–1808, doi: 10.1029/jc084ic04p01797.

Harris, D. L. (1963), Characteristics of the hurricane storm surge, *Tech. Rep. 48*, US Weather Bureau.

Holland, G. J. (1980), An analytic model of the wind and pressure profiles in hurricanes., *Monthly Weather Review*, *108*(8), 1212–1218, doi:10.1175/1520-0493(1980)108<1212:AAMOTW>2.0.CO;2.

Holland, G. J., J. I. Belanger, and A. Fritz (2010), A revised model for radial profiles of hurricane winds, *Monthly Weather Review*, *138*(12), 4393–4401, doi: 10.1175/2010MWR3317.1.

Irish, J. L., and D. T. Resio (2010), A hydrodynamics-based surge scale for hurricanes, *Ocean Engineering*, *37*(1), 69–81, doi:10.1016/j.oceaneng.2009.07.012.

Irish, J. L., D. T. Resio, and J. J. Ratcliff (2008), The influence of storm size on hurricane surge, *Journal of Physical Oceanography*, *38*(9), 2003–2013, doi: 10.1175/2008JPO3727.1.

Janssen, P. A. E. M. (1989), Wave-Induced Stress and the Drag of Air Flow over Sea Waves, *Journal of Physical Oceanography*, *19*(6), 745–754, doi:10.1175/1520-0485(1989)019<0745:wisatd>2.0.co;2.

Kennedy, A. B., et al. (2011), Origin of the Hurricane Ike forerunner surge, *Geophysical Research Letters*, *38*(8), n/a–n/a, doi:10.1029/2011GL047090.

Kouhi, S., and M. Hashemi (under revision), Modeling the impact of sea level rise on the maximum flood elevation using idealized and real case studies, *Journal of Climatic Change*.

Lin, N., K. Emanuel, M. Oppenheimer, and E. Vanmarcke (2012), Physically based assessment of hurricane surge threat under climate change, *Nature Climate Change*, *2*(6), 462–467, doi:10.1038/nclimate1389.

Luettich, R., and J. Westerink (2004), Formulation and numerical implementation of the 2d/3d adcirc finite element model version 44. xx.

Mao, M., and M. Xia (2017), Dynamics of wave–current–surge interactions in Lake Michigan: A model comparison, *Ocean Modelling*, *110*, 1–20, doi: 10.1016/j.ocemod.2016.12.007.

Ramos-Valle, A. N., E. N. Curchitser, and C. L. Bruyère (2020), Impact of Tropical Cyclone Landfall Angle on Storm Surge Along the Mid-Atlantic Bight, *Journal of Geophysical Research: Atmospheres*, *125*(4), doi:10.1029/2019JD031796.

Rego, J. L., and C. Li (2009), On the importance of the forward speed of hurricanes in storm surge forecasting: A numerical study, *Geophysical Research Letters*, *36*(7), n/a–n/a, doi:10.1029/2008GL036953.

Reichl, B. G., T. Hara, and I. Ginis (2014), Sea state dependence of the wind stress over the ocean under hurricane winds, *Journal of Geophysical Research: Oceans*, *119*(1), 30–51, doi:10.1002/2013JC009289.

Resio, D. T., and J. J. Westerink (2008), Modeling the physics of storm surges, *Physics Today*, *61*(9), 33–38, doi:10.1063/1.2982120.

Smith, S. D. (1980), Wind stress and heat flux over the ocean in gale force winds., *J. Phys. Oceanogr.*, *10*(5 , May 1980), 709–726, doi:10.1016/0198-0254(80)95947-6.

Soulsby, R. L., L. Hamm, G. Klopman, D. Myrhaug, R. R. Simons, and G. P. Thomas (1993), Wave-current interaction within and outside the bottom boundary layer, *Tech. Rep. 1-3*, doi:10.1016/0378-3839(93)90045-A.

Torres, M. J. (2017), A Coupled Wave-Surge Modeling Study in Rhode Island Coastal Waters, Master's thesis, University of Rhode Island.

Torres, M. J., M. R. Hashemi, S. Hayward, M. Spaulding, I. Ginis, and S. T. Grilli (2019), Role of hurricane wind models in accurate simulation of storm surge and waves, *Journal of Waterway, Port, Coastal, and Ocean Engineering*, *145*(1), 04018,039, doi:10.1061/(ASCE)WW.1943-5460.0000496.

Ullman, D. S., I. Ginis, W. Huang, C. Nowakowski, X. Chen, and P. Stempel (2019), Assessing the multiple impacts of extreme hurricanes in southern new england, usa, *Geosciences*, *9*(6), doi:10.3390/geosciences9060265.

Weisberg, R. H., and L. Zheng (2006), Hurricane storm surge simulations for Tampa Bay, *Tech. Rep. 6*, doi:10.1007/BF02798649.

Xie, L., L. J. Pietrafesa, and K. Wu (2003), A numerical study of wave-current interaction through surface and bottom stresses: Coastal ocean response to Hurricane Fran of 1996, *Journal of Geophysical Research C: Oceans*, *108*(2), 31–1, doi:10.1029/2001jc001078.

Xie, L., H. Liu, and M. Peng (2008), The effect of wave-current interactions on the storm surge and inundation in Charleston Harbor during Hurricane Hugo 1989, *Ocean Modelling*, *20*(3), 252–269, doi:10.1016/j.ocemod.2007.10.001.

Zheng, X., R. Mayerle, Y. Wang, and H. Zhang (2018), Study of the wind drag coefficient during the storm Xaver in the German Bight using data assimilation, *Dynamics of Atmospheres and Oceans*, *83*, 64–74, doi:10.1016/j.dynatmoce.2018.06.001.

APPENDIX A

To clarify further the effect of a smoothed wind field on the wave simulations, an additional sensitivity experiment was performed for the small and fast moving TC case using WW3. In this additional experiment, the wind field was generated at 1/3° spatial resolution but the wave model was run at 1/24° spatial resolution. Note this is exactly the same wind field as used to force the 1/3° WW3 experiments discussed above. In Fig. A.1, the result is compared to that of the original experiments where the prescribed winds are not smoothed. The smoothed input wind field in the 1/24° experiment (dashed line) lowers the wave energy in both front and rear region and retains the energy asymmetry. This additional test clearly demonstrates that smoothing of the wind field simply reduces the wave energy everywhere and does not change the energy distribution in the wave field, as shown in the low resolution experiments.

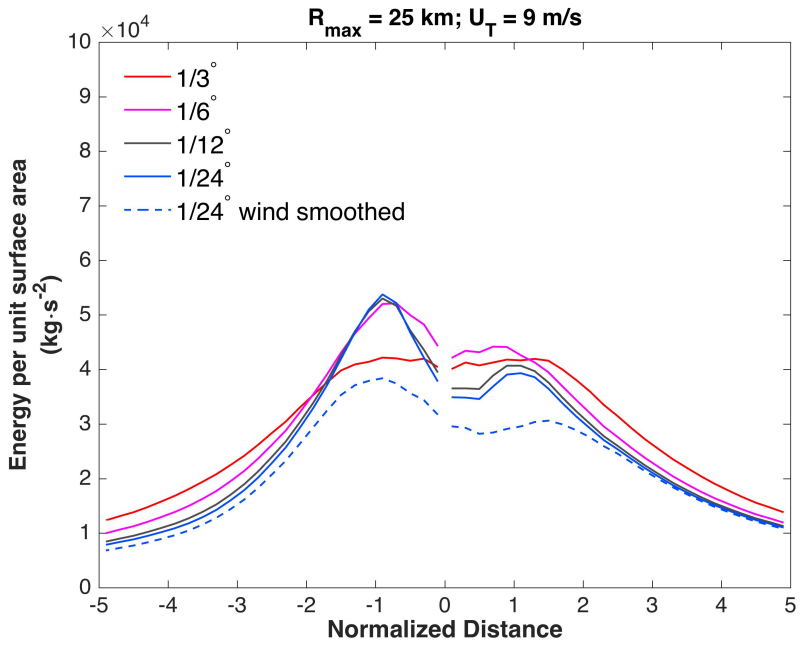

Figure A.1: Comparison of the half-annulus averaged wave energy in original experiments (solid lines) and in an additional experiment forced by a smoothed wind field of 1/3° spatial resolution (dashed line).

Maximum errors in local SWH in right front of the storm near R_{max} in 1/3°, 1/6°, and 1/12° resolution simulations are provided below for reference. The ranges are produced by the variation of TC translation direction.

Table A.1: Maximum underestimation of the local SWH at right front R_{max} with different resolutions relative to results with 1/24°

R_{max} (km)	U_T (m/s)	1/3°		1/6°		1/12°	
		WW3	**SWAN**	**WW3**	**SWAN**	**WW3**	**SWAN**
25	3	−10.5∼0%	−9.8∼ −2.8%	−6.0∼ −3.6%	−2.9∼ −1.5%	−3.8∼ −1.6%	−1.9∼ −1.4%
	6	−15.7∼ −6.9%	−19.0∼ −11.7%	−6.9∼ −4.9%	−7.3∼ −6.2%	−3.8∼ −2.0%	−3.8∼ −2.2%
	9	−17.4∼ −8.7%	−22.9∼ −16.6%	−5.4∼ −4.7%	−8.9∼ −7.9%	−2.8∼ −1.4%	−4.2∼ −2.8%
50	3	−6.3∼ −4.3%	−3.3∼ −2.5%	−4.4∼ −2.5%	−3.3∼ −2.6%	−1.3∼ −0.9%	−2.0∼ −1.4%
	6	−8.4∼ −5.9%	−8.3∼ −6.5%	−5.3∼ −3.3%	−5.4∼ −3.9%	−2.2∼ −1.8%	−2.4∼ −1.7%
	9	−6.9∼ −5.8%	−11.1∼ −9.4%	−3.9∼ −2.4%	−7.3∼ −5.3%	−1.2∼ −0.9%	−3.2∼ −1.9%

APPENDIX B

In this study the spectral tail level B_{sat} has been empirically derived as a function of 10-meter wind speed so that the mean of the drag coefficient (C_d) under TCs agrees with the GFDL bulk C_d parameterization as described in Part I. However, different operational TC and storm surge models use different bulk C_d parameterizations. Therefore, it is desirable to examine to what degree our results remain valid if a different C_d parameterization is used to derive the B_{sat} level.

Here, the C_d bulk parameterization used in the operational Advanced Circulation Model (ADCIRC) (*Ullman et al.*, 2019) for storm surge prediction (red line in Figure A1a) is chosen to derive the B_{sat} level instead of the GFDL C_d parameterization (black line in Fig. B.1a). The resulting B_{sat} values are compared in Figure A1b. Both the drag coefficient and the B_{sat} value are significantly higher at high wind speeds with the ADCIRC parameterization. Next, C_d is simulated using the ADCIRC-based empirical B_{sat} in the strong fast-moving TC (V_{max}=65 m/s, U_T=10 m/s) on the steeper 1:200 bottom slope. The spatial distributions of the ratio of C_d in shallow water to that in deep water are displayed in Fig. B.2 at three different depths. Both the magnitude and the pattern of the relative changes due to shoaling TC waves are almost identical to those simulated with the GFDL-based empirical B_{sat} shown in Fig. 3.7.

This example suggests that the shoaling wave impacts on C_d presented in this study are not very sensitive to the choice of the bulk C_d formula used for the empirical derivation of B_{sat}.

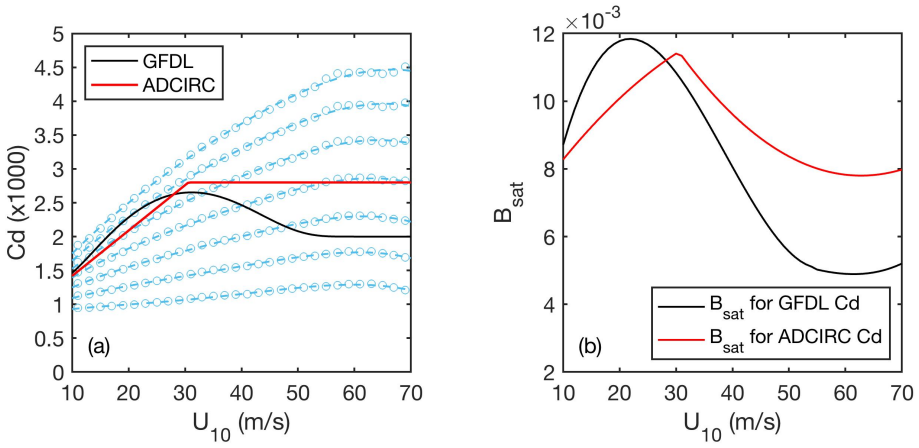

Figure B.1: (a): bulk C_d formula as a function of wind speed used in GFDL (black) and ADCIRC (red) models. Dashed lines and circles in light blue represent the mean C_d as a function of U_{10} under 27 idealized hurricanes (see Part I for details), calculated with 7 different values of B_{sat} (0.002 to 0.014 with 0.002 increment from bottom up). (b): Empirical B_{sat} value as a function of U_{10} so that the mean C_d is consistent with GFDL or ADCIRC bulk C_d parameterization.

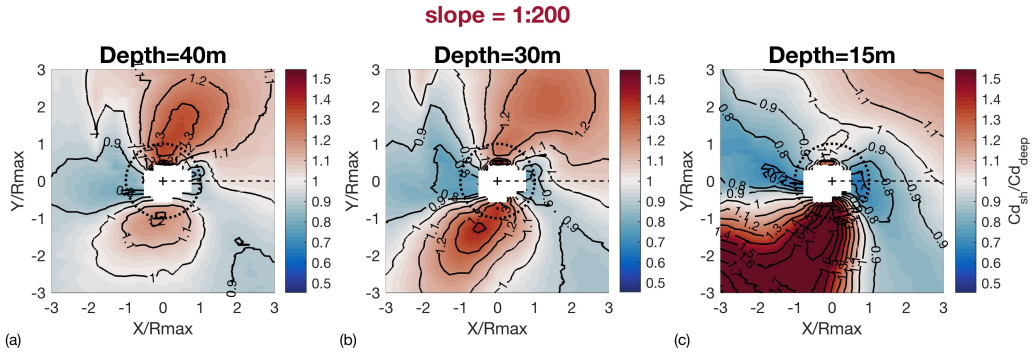

Figure B.2: Same as Fig. 3.7, but with B_{sat} derived from the ADCIRC bulk C_d instead of GFDL bulk C_d.

REFERENCES

Ullman, D. S., I. Ginis, W. Huang, C. Nowakowski, X. Chen, and P. Stempel (2019), Assessing the multiple impacts of extreme hurricanes in southern new england, usa, *Geosciences*, *9*(6), doi:10.3390/geosciences9060265.

BIBLIOGRAPHY

Akbar, M., S. Kanjanda, and A. Musinguzi (2017), Effect of Bottom Friction, Wind Drag Coefficient, and Meteorological Forcing in Hindcast of Hurricane Rita Storm Surge Using SWAN + ADCIRC Model, *Journal of Marine Science and Engineering*, *5*(4), 38, doi:10.3390/jmse5030038.

Anctil, F., and M. A. Donelan (1996), Air-water momentum flux observations over shoaling waves, *Journal of Physical Oceanography*, *26*(7), 1344–1353, doi:10.1175/1520-0485(1996)026<1344:AMFOOS>2.0.CO;2.

Ardhuin, F., et al. (2010), Semiempirical dissipation source functions for ocean waves. Part I: Definition, calibration, and validation, *Journal of Physical Oceanography*, *40*(9), 1917–1941, doi:10.1175/2010JPO4324.1.

Arns, A., S. Dangendorf, J. Jensen, S. Talke, J. Bender, and C. Pattiaratchi (2017), Sea-level rise induced amplification of coastal protection design heights, *Scientific Reports*, *7*(1), 40,171, doi:10.1038/srep40171.

Babanin, A. (2011), *Breaking and Dissipation of Ocean Surface Waves*, Cambridge University Press, doi:10.1017/CBO9780511736162.

Babanin, A. V., M. L. Banner, I. R. Young, and M. A. Donelan (2007), Wave-follower field measurements of the wind-input spectral function. Part III: Parameterization of the wind-input enhancement due to wave breaking, *Journal of Physical Oceanography*, *37*(11), 2764–2775, doi:10.1175/2007JPO3757.1.

Banner, M. L. (1990), The influence of wave breaking on the surface pressure distribution in wind-wave interactions, *Journal of Fluid Mechanics*, *211*(463), 463–495, doi:10.1017/S0022112090001653.

Banta, R. M., et al. (2018), Evaluating and improving nwp forecast models for the future:

How the needs of offshore wind energy can point the way, *Bulletin of the American Meteorological Society*, *99*(6), 1155–1176, doi:10.1175/BAMS-D-16-0310.1.

Barber, N., and F. Ursell (1948), The generation and propagation of ocean waves and swell. i. wave periods and velocities, *Philosophical Transactions of the Royal Society of London A: Mathematical, Physical and Engineering Sciences*, *240*(824), 527–560, doi:10.1098/rsta.1948.0005.

Battjes, J. A., and J. Janssen (1978), Energy loss and set-up due to breaking of random waves, in *Coastal Engineering 1978*, pp. 569–587.

Bell, M. M., M. T. Montgomery, and K. A. Emanuel (2012), Air-sea enthalpy and momentum exchange at major hurricane wind speeds observed during CBLAST, *Journal of the Atmospheric Sciences*, *69*(11), 3197–3222, doi:10.1175/JAS-D-11-0276.1.

Bi, X., Z. Gao, Y. Liu, F. Liu, Q. Song, J. Huang, H. Huang, W. Mao, and C. Liu (2015), Observed drag coefficients in high winds in the near offshore of the South China sea, *Journal of Geophysical Research*, *120*(13), 6444–6459, doi:10.1002/2015JD023172.

Biswas, M. K., et al. (2018), Hurricane Weather Research and Forecasting (HWRF) Model: 2018 Scientific Documentation, *Tech. Rep. November*.

Black, P. G., E. A. D'Asaro, W. M. Drennan, J. R. French, P. P. Niiler, T. B. Sanford, E. J. Terrill, E. J. Walsh, and J. A. Zhang (2007), Air-sea exchange in hurricanes: Synthesis of observations from the coupled boundary layer air-sea transfer experiment, *Bulletin of the American Meteorological Society*, *88*(3), 357–374, doi:10.1175/BAMS-88-3-357.

Blair, A., I. Ginis, T. Hara, and E. Ulhorn (2017), Impact of Langmuir Turbulence on Upper Ocean Response to Hurricane Edouard: Model and Observations, *Journal of Geophysical Research: Oceans*, *122*(12), 9712–9724, doi:10.1002/2017JC012956.

Booij, N., R. C. Ris, and L. H. Holthuijsen (1999), A third-generation wave model for

coastal regions: 1. Model description and validation, *Journal of Geophysical Research*, *104*(C4), 7649, doi:10.1029/98JC02622.

Bunya, S., et al. (2010), A High-Resolution Coupled Riverine Flow, Tide, Wind, Wind Wave, and Storm Surge Model for Southern Louisiana and Mississippi. Part I: Model Development and Validation, *Monthly Weather Review*, *138*(2), 345–377, doi:10.1175/2009MWR2906.1.

Cavaleri, L. (2009), Wave modeling–missing the peaks, *Journal of Physical Oceanography*, *39*(11), 2757–2778, doi:10.1175/2009JPO4067.1.

Chao, Y. Y., J.-H. G. M. Alves, H. L. Tolman, Y. Y. Chao, J.-H. G. M. Alves, and H. L. Tolman (2005), An Operational System for Predicting Hurricane-Generated Wind Waves in the North Atlantic Ocean*, *Weather and Forecasting*, *20*(4), 652–671, doi:10.1175/WAF851.1.

Chawla, A., H. L. Tolman, V. Gerald, D. Spindler, T. Spindler, J.-H. G. M. Alves, D. Cao, J. L. Hanson, and E.-M. Devaliere (2013), A multigrid wave forecasting model: A new paradigm in operational wave forecasting, *Weather and Forecasting*, *28*(4), 1057–1078, doi:10.1175/WAF-D-12-00007.1.

Chen, S. S., and M. Curcic (2016), Ocean surface waves in Hurricane Ike (2008) and Superstorm Sandy (2012): Coupled model predictions and observations, *Ocean Modelling*, *103*, 161–176, doi:10.1016/j.ocemod.2015.08.005.

Chen, X., I. Ginis, and T. Hara (2020a), Impact of shoaling ocean surface waves on wind stress and drag coefficient in coastal waters: Part ii tropical cyclones, *Journal of Geophysical Research: Oceans*, *n/a*(n/a), doi:10.1029/2020JC016223.

Chen, X., T. Hara, and I. Ginis (2020b), Impact of shoaling ocean surface waves on wind stress and drag coefficient in coastal waters: Part i uniform wind, *Journal of Geophysical Research: Oceans*, *n/a*(n/a), doi:10.1029/2020JC016222.

Cox, C., and W. Munk (1954), Measurement of the Roughness of the Sea Surface from Photographs of the Sun's Glitter, *Journal of the Optical Society of America*, *44*(11), 838, doi:10.1364/josa.44.000838.

Dietrich, J. C., et al. (2010), A high-resolution coupled riverine flow, tide, wind, wind wave, and storm surge model for southern louisiana and mississippi. part ii: Synoptic description and analysis of hurricanes katrina and rita, *Monthly Weather Review*, *138*(2), 378–404, doi:10.1175/2009MWR2907.1.

Dietrich, J. C., et al. (2011), Modeling hurricane waves and storm surge using integrally-coupled, scalable computations, *Coastal Engineering*, *58*(1), 45–65, doi:10.1016/j.coastaleng.2010.08.001.

Donelan, M. A. (2018), On the Decrease of the Oceanic Drag Coefficient in High Winds, *Journal of Geophysical Research: Oceans*, *123*(2), 1485–1501, doi:10.1002/2017JC013394.

Donelan, M. A., F. W. Dobson, S. D. Smith, and R. J. Anderson (1993), On the dependence of sea surface roughness on wave development, *Journal of Physical Oceanography*, *23*(9), 2143–2149, doi:10.1175/1520-0485(1993)023<2143:OTDOSS>2.0.CO;2.

Donelan, M. A., W. M. Drennan, and K. B. Katsaros (1997a), The air-sea momentum flux in conditions of wind sea and swell, *Tech. Rep. 10*, doi:10.1175/1520-0485(1997)027<2087:TASMFI>2.0.CO;2.

Donelan, M. A., W. M. Drennan, and K. B. Katsaros (1997b), The air-sea momentum flux in conditions of wind sea and swell, *Journal of Physical Oceanography*, *27*(10), 2087–2099, doi:10.1175/1520-0485(1997)027<2087:TASMFI>2.0.CO;2.

Donelan, M. A., B. K. Haus, N. Reul, W. J. Plant, M. Stiassnie, H. C. Graber, O. B. Brown, and E. S. Saltzman (2004), On the limiting aerodynamic roughness of the ocean in very strong winds, *Geophysical Research Letters*, *31*(18), L18,306, doi:10.1029/2004GL019460.

Donelan, M. A., A. V. Babanin, I. R. Young, and M. L. Banner (2006), Wave-follower field measurements of the wind-input spectral function. Part II: Parameterization of the wind input, *Journal of Physical Oceanography*, *36*(8), 1672–1689, doi: 10.1175/JPO2933.1.

Donelan, M. A., M. Curcic, S. S. Chen, and A. K. Magnusson (2012), Modeling waves and wind stress, *Journal of Geophysical Research: Oceans*, *117*(7), doi: 10.1029/2011JC007787.

Drennan, W. M., K. K. Kahma, and M. A. Donelan (1999), On momentum flux and velocity spectra over waves, *Boundary-Layer Meteorology*, *92*(3), 489–515, doi: 10.1023/A:1002054820455.

Drennan, W. M., P. K. Taylor, and M. J. Yelland (2005), Parameterizing the sea surface roughness, *Journal of Physical Oceanography*, *35*(5), 835–848, doi:10.1175/JPO2704.1.

Dresback, K. M., et al. (2013), Skill assessment of a real-time forecast system utilizing a coupled hydrologic and coastal hydrodynamic model during hurricane irene (2011), *Continental Shelf Research*, *71*(Supplement C), 78 – 94, doi: https://doi.org/10.1016/j.csr.2013.10.007.

Edson, J. B., et al. (2013), On the exchange of momentum over the open ocean, *Journal of Physical Oceanography*, *43*(8), 1589–1610, doi:10.1175/JPO-D-12-0173.1.

Eldeberky, Y. (1995), Parameterization of triad interaction in wave energy model, in *Proc. Coastal Dynamics Conf. Gdansk, Poland, 1995.*

Eldeberky, Y. (1996), Nonlinear transformations ofwave spectra in the nearshore zone, Ph.D. thesis, Fac. of Civil Engineering and Geosciences, Delft University of Technology, The Netherlands.

Emanuel, K. A. (1986), An air-sea interaction theory for tropical cyclones. part i: Steady-state maintenance, *Journal of the Atmospheric Sciences*, *43*(6), 585–605, doi: 10.1175/1520-0469(1986)043<0585:AASITF>2.0.CO;2.

Emanuel, K. A. (2003), A similarity hypothesis for air-sea exchange at extreme wind speeds, *Journal of the Atmospheric Sciences*, *60*(11), 1420–1428, doi:10.1175/1520-0469(2003)060<1420:ASHFAE>2.0.CO;2.

Fan, Y., I. Ginis, T. Hara, C. W. Wright, and E. J. Walsh (2009), Numerical Simulations and Observations of Surface Wave Fields under an Extreme Tropical Cyclone, *Journal of Physical Oceanography*, *39*(9), 2097–2116, doi:10.1175/2009JPO4224.1.

Feng, X., B. Yin, and D. Yang (2016), Development of an unstructured-grid wave-current coupled model and its application, *Ocean Modelling*, *104*, 213 – 225, doi: https://doi.org/10.1016/j.ocemod.2016.06.007.

Fleming, J. G., C. W. Fulcher, R. A. Luettich, B. D. Estrade, G. D. Allen, and H. S. Winer (2008), A real time storm surge forecasting system using adcirc, in *Estuarine and Coastal Modeling (2007)*, pp. 893–912, doi:10.1061/40990(324)48.

French, J. R., W. M. Drennan, J. A. Zhang, and P. G. Black (2007), Turbulent fluxes in the hurricane boundary layer. Part I: Momentum flux, *Journal of the Atmospheric Sciences*, *64*(4), 1089–1102, doi:10.1175/JAS3887.1.

Garner, A. J., et al. (2017), Impact of climate change on New York City's coastal flood hazard: Increasing flood heights from the preindustrial to 2300 CE, *Proceedings of the National Academy of Sciences of the United States of America*, *114*(45), 11,861–11,866, doi:10.1073/pnas.1703568114.

Garratt, J. R. (1977), Review of Drag Coefficients over Oceans and Continents, *Monthly Weather Review*, *105*(7), 915–929, doi:10.1175/1520-0493(1977)105<0915:rodcoo>2.0.co;2.

Geernaert, G. L. (1988), Measurements of the angle between the wind vector and wind stress vector in the surface layer over the North Sea, *Journal of Geophysical Research*, *93*(C7), 8215, doi:10.1029/jc093ic07p08215.

Geernaert, G. L., K. B. Katsaros, and K. Richter (1986), Variation of the drag coefficient and its dependence on sea state, *Journal of Geophysical Research*, *91*(C6), 7667, doi: 10.1029/jc091ic06p07667.

Gentry, M. S., G. M. Lackmann, M. S. Gentry, and G. M. Lackmann (2010), Sensitivity of Simulated Tropical Cyclone Structure and Intensity to Horizontal Resolution, *Monthly Weather Review*, *138*(3), 688–704, doi:10.1175/2009MWR2976.1.

Ginis, I. (2002), Tropical cyclone-ocean interactions, *Advances in Fluid Mechanics Series*, *33*, 83–114.

Ginis, I., M. Bender, B. Thomas, M. Morin, V. Tallapragada, and A. Soloviev (2015), A new drag coefficient formulation and its impact on the gfdl and hwrf hurricane model predictions, 19th Conference on Air-Sea Interaction, Phoenix, AZ, January 4-8.

Grachev, A. A., C. W. Fairall, J. E. Hare, J. B. Edson, and S. D. Miller (2003), Wind stress vector over ocean waves, *Journal of Physical Oceanography*, *33*(11), 2408–2429, doi:10.1175/1520-0485(2003)033<2408:WSVOOW>2.0.CO;2.

Grant, W. D., and O. S. Madsen (1979), Combined wave and current interaction with a rough bottom, *Journal of Geophysical Research: Oceans*, *84*(C4), 1797–1808, doi: 10.1029/jc084ic04p01797.

Haiden, T., M. Janousek, J. Bidlot, L. Ferranti, F. Prates, F. Vitart, P. Bauer, and D. Richardson (2016), *Evaluation of ECMWF forecasts, including the 2016 resolution upgrade*.

Hara, T., and S. E. Belcher (2004), Wind profile and drag coefficient over mature ocean surface wave spectra, *Journal of Physical Oceanography*, *34*(11), 2345–2358, doi:10.1175/JPO2633.1.

Harris, D. L. (1963), Characteristics of the hurricane storm surge, *Tech. Rep. 48*, US Weather Bureau.

Hashemi, M. R., M. L. Spaulding, A. Shaw, H. Farhadi, and M. Lewis (2016), An efficient artificial intelligence model for prediction of tropical storm surge, *Natural Hazards*, *82*(1), 471–491, doi:10.1007/s11069-016-2193-4.

Hasselmann, K. (1974), On the spectral dissipation of ocean waves due to white capping, *Boundary-Layer Meteorology*, *6*(1), 107–127, doi:10.1007/BF00232479.

Hasselmann, K., et al. (1973), Measurements of wind-wave growth and swell decay during the joint North Sea wave project (JONSWAP)., *Erganzungsheft zur Deutschen Hydrographischen Zeitschrift*, *12*(8).

Hasselmann, K., et al. (1988), The WAM model - a third generation ocean wave prediction model., *J. Phys. Oceanogr.*, *18*(12 , Dec. 1988), 1775–1810, doi:10.1175/1520-0485(1988)018<1775:twmtgo>2.0.co;2.

Holland, G. J. (1980), An analytic model of the wind and pressure profiles in hurricanes., *Monthly Weather Review*, *108*(8), 1212–1218, doi:10.1175/1520-0493(1980)108<1212:AAMOTW>2.0.CO;2.

Holland, G. J., J. I. Belanger, and A. Fritz (2010), A revised model for radial profiles of hurricane winds, *Monthly Weather Review*, *138*(12), 4393–4401, doi:10.1175/2010MWR3317.1.

Holthuijsen, L. H., M. D. Powell, and J. D. Pietrzak (2012), Wind and waves in extreme hurricanes, *Journal of Geophysical Research: Oceans*, *117*(9), doi:10.1029/2012JC007983.

Hristov, T. S., S. D. Miller, and C. A. Friehe (2003), Dynamical coupling of wind and ocean waves through wave-induced air flow, *Nature*, *422*(6927), 55–58, doi:10.1038/nature01382.

Hsu, J. Y., R. C. Lien, E. A. D'Asaro, and T. B. Sanford (2017), Estimates of surface wind stress and drag coefficients in Typhoon Megi, *Journal of Physical Oceanography*, *47*(3), 545–565, doi:10.1175/JPO-D-16-0069.1.

Hsu, J. Y., R. C. Lien, E. A. D'Asaro, and T. B. Sanford (2019), Scaling of Drag Coefficients Under Five Tropical Cyclones, *Geophysical Research Letters*, *46*(6), 3349–3358, doi:10.1029/2018GL081574.

Huang, Y., R. H. Weisberg, L. Zheng, and M. Zijlema (2013), Gulf of Mexico hurricane wave simulations using SWAN: Bulk formula-based drag coefficient sensitivity for Hurricane Ike, *Journal of Geophysical Research: Oceans*, *118*(8), 3916–3938, doi:10.1002/jgrc.20283.

Husain, N. T., T. Hara, M. P. Buckley, K. Yousefi, F. Veron, and P. P. Sullivan (2019), Boundary layer turbulence over surface waves in a strongly forced condition: LES and observation, *Journal of Physical Oceanography*, *49*(8), 1997–2015, doi:10.1175/JPO-D-19-0070.1.

Irish, J. L., and D. T. Resio (2010), A hydrodynamics-based surge scale for hurricanes, *Ocean Engineering*, *37*(1), 69–81, doi:10.1016/j.oceaneng.2009.07.012.

Irish, J. L., D. T. Resio, and J. J. Ratcliff (2008), The influence of storm size on hurricane surge, *Journal of Physical Oceanography*, *38*(9), 2003–2013, doi:10.1175/2008JPO3727.1.

Janssen, J. (1997), Does wind stress depend on sea-state or not? A statistical error analysis of HEXMAX data, *Tech. Rep. 3*, doi:10.1023/A:1000336814021.

Janssen, P. (2004), *The Interaction of Ocean Waves and Wind*, Cambridge University Press, doi:10.1017/CBO9780511525018.

Janssen, P. A. E. M. (1989), Wave-Induced Stress and the Drag of Air Flow over Sea Waves, *Journal of Physical Oceanography*, *19*(6), 745–754, doi:10.1175/1520-0485(1989)019<0745:wisatd>2.0.co;2.

Jarosz, E., D. A. Mitchell, D. W. Wang, and W. J. Teague (2007), Bottom-up determination of air-sea momentum exchange under a major tropical cyclone, *Science*, *315*(5819), 1707–1709, doi:10.1126/science.1136466.

Jiménez, P. A., and J. Dudhia (2018), On the need to modify the sea surface roughness formulation over shallow waters, *Journal of Applied Meteorology and Climatology*, *57*(5), 1101–1110, doi:10.1175/JAMC-D-17-0137.1.

Johnson, H. K., and H. Kofoed-Hansen (2000), Influence of bottom friction on sea surface roughness and its impact on shallow water wind wave modeling, *Journal of Physical Oceanography*, *30*(7), 1743–1756, doi:10.1175/1520-0485(2000)030<1743:IOBFOS>2.0.CO;2.

Jones, I., and Y. Toba (2001), *Wind Stress over the Ocean*, Cambridge University Press, doi:10.1017/CBO9780511552076.

Kennedy, A. B., et al. (2011), Origin of the Hurricane Ike forerunner surge, *Geophysical Research Letters*, *38*(8), n/a–n/a, doi:10.1029/2011GL047090.

Kerr, P. C., et al. (2013), U.S. IOOS coastal and ocean modeling testbed: Evaluation of tide, wave, and hurricane surge response sensitivities to mesh resolution and friction in the Gulf of Mexico, *Journal of Geophysical Research: Oceans*, *118*(9), 4633–4661, doi:10.1002/jgrc.20305.

Knaff, J. A., and R. M. Zehr (2007), Reexamination of tropical cyclone wind-pressure relationships, *Weather and Forecasting*, *22*(1), 71–88, doi:10.1175/WAF965.1.

Komen, G. J., S. Hasselmann, and K. Hasselmann (1984), On the existence of a fully developed wind-sea spectrum, *Journal of Physical Oceanography*, *14*(8), 1271–1285, doi:10.1175/1520-0485(1984)014<1271:OTEOAF>2.0.CO;2.

Kossin, J. P. (2018), A global slowdown of tropical-cyclone translation speed, *Nature*, *558*(7708), 104–107, doi:10.1038/s41586-018-0158-3.

Kouhi, S., and M. Hashemi (under revision), Modeling the impact of sea level rise on the maximum flood elevation using idealized and real case studies, *Journal of Climatic Change*.

Landsea, C. W., and J. L. Franklin (2013), Atlantic hurricane database uncertainty and presentation of a new database format, *Monthly Weather Review*, *141*(10), 3576–3592, doi:10.1175/MWR-D-12-00254.1.

Landsea, C. W., A. Hagen, W. Bredemeyer, C. Carrasco, D. A. Glenn, A. Santiago, D. Strahan-Sakoskie, and M. Dickinson (2014), A reanalysis of the 1931-43 atlantic hurricane database, *Journal of Climate*, *27*(16), 6093–6118, doi:10.1175/JCLI-D-13-00503.1.

Large, W. G., and S. Pond (1981), Open ocean momentum flux measurements in moderate to strong winds., *J. Phys. Oceanogr.*, *11*(3 , Mar. 1981), 324–336, doi:10.1175/1520-0485(1981)011<0324:oomfmi>2.0.co;2.

Laxague, N. J., C. J. Zappa, D. A. LeBel, and M. L. Banner (2018), Spectral Characteristics of Gravity-Capillary Waves, With Connections to Wave Growth and Microbreaking, *Journal of Geophysical Research: Oceans*, *123*(7), 4576–4592, doi:10.1029/2018JC013859.

Li, R., L. Xie, B. Liu, and C. Guan (2013), On the sensitivity of hurricane storm surge simulation to domain size, *Ocean Modelling*, *67*, 1–12, doi:10.1016/j.ocemod.2013.03.005.

Lin, N., K. Emanuel, M. Oppenheimer, and E. Vanmarcke (2012), Physically based assessment of hurricane surge threat under climate change, *Nature Climate Change*, *2*(6), 462–467, doi:10.1038/nclimate1389.

Liu, Q., A. Babanin, Y. Fan, S. Zieger, C. Guan, and I. J. Moon (2017), Numerical simulations of ocean surface waves under hurricane conditions: Assessment of existing model performance, *Ocean Modelling*, *118*, 73–93, doi:10.1016/j.ocemod.2017.08.005.

Longuet-Higgins, M., and R. Stewart (1964), Radiation stresses in water waves; a physical discussion, with applications, *Deep Sea Research and Oceanographic Abstracts*, *11*(4), 529 – 562, doi:https://doi.org/10.1016/0011-7471(64)90001-4.

Luettich, R., and J. Westerink (2004), Formulation and numerical implementation of the 2d/3d adcirc finite element model version 44. xx.

MacMahan, J. (2017), Increased aerodynamic roughness owing to surfzone foam, *Journal of Physical Oceanography*, *47*(8), 2115–2122, doi:10.1175/JPO-D-17-0054.1.

Mahrt, L., E. L. Andreas, J. B. Edson, D. Vickers, J. Sun, and E. G. Patton (2016), Coastal zone surface stress with stable stratification, *Journal of Physical Oceanography*, *46*(1), 95–105, doi:10.1175/JPO-D-15-0116.1.

Makin, V. K., and V. N. Kudryavtsev (1999), Coupled sea surface-atmosphere model: 1. Wind over waves coupling, *Journal of Geophysical Research: Oceans*, *104*(C4), 7613–7623, doi:10.1029/1999jc900006.

Makin, V. K., and V. N. Kudryavtsev (2002), Impact of dominant waves on sea drag, *Boundary-Layer Meteorology*, *103*(1), 83–99, doi:10.1023/A:1014591222717.

Mao, M., and M. Xia (2017), Dynamics of wave–current–surge interactions in Lake Michigan: A model comparison, *Ocean Modelling*, *110*, 1–20, doi:10.1016/j.ocemod.2016.12.007.

Moon, I.-J., I. Ginis, T. Hara, H. L. Tolman, C. W. Wright, and E. J. Walsh (2003), Numerical simulation of sea surface directional wave spectra under hurricane wind forcing, *Journal of Physical Oceanography*, *33*(8), 1680–1706, doi:10.1175/2410.1.

Moon, I. J., I. Ginis, and T. Hara (2004a), Effect of surface waves on air-sea momentum exchange. Part II: Behavior of drag coefficient under tropical cyclones, *Journal of the Atmospheric Sciences*, *61*(19), 2334–2348, doi:10.1175/1520-0469(2004)061<2334:EOSWOA>2.0.CO;2.

Moon, I. J., T. Hara, I. Ginis, S. E. Belcher, and H. L. Tolman (2004b), Effect of surface waves on air-sea momentum exchange: Part I: Effect of mature and growing seas, *Journal of the Atmospheric Sciences*, *61*(19), 2321–2333, doi:10.1175/1520-0469(2004)061<2321:EOSWOA>2.0.CO;2.

Oost, W. A. (1994), Flow distortion calculations and their application in HEXMAX, *Journal of Atmospheric & Oceanic Technology*, *11*(2 Part 1), 366–386, doi:10.1175/1520-0426(1994)011<0366:fdcata>2.0.co;2.

Oost, W. A. (1998), The KNMI HEXMAX stress data - a reanalysis, *Tech. Rep. 3*, doi:10.1023/A:1000824918910.

Oost, W. A., G. J. Komen, C. M. Jacobs, and C. Van Oort (2002), New evidence for a relation between wind stress and wave age from measurements during ASGAMAGE, *Boundary-Layer Meteorology*, *103*(3), 409–438, doi:10.1023/A:1014913624535.

Ortiz-Suslow, D. G., B. K. Haus, N. J. Williams, N. J. Laxague, A. J. Reniers, and H. C. Graber (2015), The spatial-temporal variability of air-sea momentum fluxes observed at a tidal inlet, *Journal of Geophysical Research: Oceans*, *120*(2), 660–676, doi:10.1002/2014JC010412.

Peirson, W. I., and A. W. Garcia (2008), On the wind-induced growth of slow water waves of finite steepness, *Journal of Fluid Mechanics*, *608*, 243–274, doi:10.1017/S002211200800205X.

Peng, S., and Y. Li (2015), A parabolic model of drag coefficient for storm surge simulation in the South China Sea, *Scientific Reports*, *5*(1), 15,496, doi:10.1038/srep15496.

Pierce, C. H. (1939), The meterological history of the new england hurricane of sept. 21, 1938, *Monthly Weather Review*, *67*(8), 237–285, doi:10.1175/1520-0493(1939)67<237:TMHOTN>2.0.CO;2.

Potter, H., C. O. Collins, W. M. Drennan, and H. C. Graber (2015a), Observations of wind stress direction during Typhoon Chaba (2010), *Geophysical Research Letters*, *42*(22), 9898–9905, doi:10.1002/2015GL065173.

Potter, H., H. C. Graber, N. J. Williams, C. O. Collins, R. J. Ramos, and W. M. Drennan (2015b), In situ measurements of momentum fluxes in typhoons, *Journal of the Atmospheric Sciences*, *72*(1), 104–118, doi:10.1175/JAS-D-14-0025.1.

Powell, M. D., P. J. Vickery, and T. A. Reinhold (2003), Reduced drag coefficient for high wind speeds in tropical cyclones, *Nature*, *422*(6929), 279–283, doi:10.1038/nature01481.

Price, J. F. (1981), Upper ocean response to a hurricane., *J. Phys. Oceanogr.*, *11*(2 , Feb. 1981), 153–175, doi:10.1175/1520-0485(1981)011<0153:uortah>2.0.co;2.

Ramos-Valle, A. N., E. N. Curchitser, and C. L. Bruyère (2020), Impact of Tropical Cyclone Landfall Angle on Storm Surge Along the Mid-Atlantic Bight, *Journal of Geophysical Research: Atmospheres*, *125*(4), doi:10.1029/2019JD031796.

Rego, J. L., and C. Li (2009), On the importance of the forward speed of hurricanes in storm surge forecasting: A numerical study, *Geophysical Research Letters*, *36*(7), n/a–n/a, doi:10.1029/2008GL036953.

Reichl, B. G., T. Hara, and I. Ginis (2014), Sea state dependence of the wind stress over the ocean under hurricane winds, *Journal of Geophysical Research: Oceans*, *119*(1), 30–51, doi:10.1002/2013JC009289.

Resio, D. T., and J. L. Irish (2015), Tropical Cyclone Storm Surge Risk, *Current Climate Change Reports*, *1*(2), 74–84, doi:10.1007/s40641-015-0011-9.

Resio, D. T., and J. J. Westerink (2008), Modeling the physics of storm surges, *Physics Today*, *61*(9), 33–38, doi:10.1063/1.2982120.

Ris, R. C., L. H. Holthuijsen, and N. Booij (1999), A third-generation wave model for coastal regions: 2. Verification, *Journal of Geophysical Research: Oceans*, *104*(C4), 7667–7681, doi:10.1029/1998JC900123.

Rogers, W. E., P. A. Hwang, and D. W. Wang (2003), Investigation of wave growth and decay in the swan model: Three regional-scale applications, *Journal of Physical Oceanography*, *33*(2), 366–389, doi:10.1175/1520-0485(2003)033<0366:IOWGAD>2.0.CO;2.

Romero, L., and W. K. Melville (2010), Airborne observations of fetch-limited waves in the gulf of tehuantepec, *Journal of Physical Oceanography*, *40*(3), 441–465, doi: 10.1175/2009JPO4127.1.

Sanford, T. B., J. F. Price, and J. B. Girton (2011), Upper-ocean response to hurricane frances (2004) observed by profiling EM-APEX floats, *Journal of Physical Oceanography*, *41*(6), 1041–1056, doi:10.1175/2010JPO4313.1.

Shabani, B., P. Nielsen, and T. Baldock (2014), Direct measurements of wind stress over the surf zone, *Journal of Geophysical Research: Oceans*, *119*(5), 2949–2973, doi: 10.1002/2013JC009585.

Shimura, T., N. Mori, and M. A. Hemer (2017), Projection of tropical cyclone-generated extreme wave climate based on CMIP5 multi-model ensemble in the Western North Pacific, *Climate Dynamics*, *49*(4), 1449–1462, doi:10.1007/s00382-016-3390-2.

Smith, S. D. (1980), Wind stress and heat flux over the ocean in gale force winds., *J. Phys. Oceanogr.*, *10*(5 , May 1980), 709–726, doi:10.1016/0198-0254(80)95947-6.

Smith, S. D., et al. (1992), Sea surface wind stress and drag coefficients: The hexos results, *Boundary-Layer Meteorology*, *60*(1-2), 109–142, doi:10.1007/BF00122064.

Soloviev, A. V., R. Lukas, M. A. Donelan, B. K. Haus, and I. Ginis (2014), The air-sea interface and surface stress under tropical cyclones, *Scientific Reports*, *4*(1), 5306, doi:10.1038/srep05306.

Soulsby, R. L., L. Hamm, G. Klopman, D. Myrhaug, R. R. Simons, and G. P. Thomas (1993), Wave-current interaction within and outside the bottom boundary layer, *Tech. Rep. 1-3*, doi:10.1016/0378-3839(93)90045-A.

Sullivan, P. P., M. L. Banner, R. P. Morison, and W. L. Peirson (2018), Turbulent flow over steep steady and unsteady waves under strong wind forcing, *Journal of Physical Oceanography*, *48*(1), 3–27, doi:10.1175/JPO-D-17-0118.1.

Sun, Y., C. Chen, R. C. Beardsley, Q. Xu, J. Qi, and H. Lin (2013), Impact of current-wave interaction on storm surge simulation: A case study for hurricane bob, *Journal of Geophysical Research: Oceans*, *118*(5), 2685–2701.

Tang, C. L., Q. Gui, and B. M. Detracey (1998), Barotropic response of the Labrador/Newfoundland shelf to a moving Storm, *Tech. Rep. 6*, doi:10.1175/1520-0485(1998)028<1152:BROTLN>2.0.CO;2.

The SWAN team (ver41.10), SWAN Scientific and Technical Documentation (Cycle III version 41.10A), *Tech. note*, Delft University of Technology, 140 pp.

The WAVEWATCH III ® Development Group (2016), User manual and system documentation of WAVEWATCH III ® version 5.16, *Tech. Note 329*, NOAA/NWS/NCEP/MMAB, College Park, MD, USA, 326 pp. + Appendices.

The WISE Group (2007), Wave modelling - The state of the art, *Progress in Oceanography*, *75*(4), 603–674, doi:10.1016/J.POCEAN.2007.05.005.

Toffoli, A., L. Loffredo, P. Le Roy, J. M. Lefèvre, and A. V. Babanin (2012), On the variability of sea drag in finite water depth, *Journal of Geophysical Research: Oceans*, *117*(7), n/a–n/a, doi:10.1029/2011JC007857.

Tolman, H. L., and J.-H. G. Alves (2005), Numerical modeling of wind waves generated by tropical cyclones using moving grids, *Ocean Modelling*, *9*(4), 305–323, doi:10.1016/j.ocemod.2004.09.003.

Tolman, H. L., and D. Chalikov (1996), Source terms in a third-generation wind wave model, *Journal of Physical Oceanography*, *26*(11), 2497–2518, doi:10.1175/1520-0485(1996)026<2497:STIATG>2.0.CO;2.

Torres, M. J. (2017), A Coupled Wave-Surge Modeling Study in Rhode Island Coastal Waters, Master's thesis, University of Rhode Island.

Torres, M. J., M. R. Hashemi, S. Hayward, M. Spaulding, I. Ginis, and S. T. Grilli (2019), Role of hurricane wind models in accurate simulation of storm surge and waves, *Journal of Waterway, Port, Coastal, and Ocean Engineering*, *145*(1), 04018,039, doi: 10.1061/(ASCE)WW.1943-5460.0000496.

Ullman, D. S., I. Ginis, W. Huang, C. Nowakowski, X. Chen, and P. Stempel (2019), Assessing the multiple impacts of extreme hurricanes in southern new england, usa, *Geosciences*, *9*(6), doi:10.3390/geosciences9060265.

Vickers, D., and L. Mahrt (1997), Fetch limited drag coefficients, *Tech. Rep. 1*, doi: 10.1023/A:1000472623187.

Vickers, D., and L. Mahrt (1999), Observations of non-dimensional wind shear in the coastal zone, *Quarterly Journal of the Royal Meteorological Society*, *125*(559), 2685–2702, doi:10.1002/qj.49712555917.

Vickery, P. J., P. F. Skerlj, and L. A. Twisdale (2000), Simulation of Hurricane Risk in the U.S. Using Empirical Track Model, *Journal of Structural Engineering*, *126*(10), 1222–1237, doi:10.1061/(ASCE)0733-9445(2000)126:10(1222).

Walsh, E. J., et al. (2002), Hurricane directional wave spectrum spatial variation at landfall, *Journal of Physical Oceanography*, *32*(6), 1667–1684, doi:10.1175/1520-0485(2002)032<1667:HDWSSV>2.0.CO;2.

Wang, D. W., D. A. Mitchell, W. J. Teague, E. Jarosz, and M. S. Hulbert (2005), Ocean science: Extreme waves under Hurricane Ivan, *Science*, *309*(5736), 896, doi: 10.1126/science.1112509.

Weisberg, R. H., and L. Zheng (2006), Hurricane storm surge simulations for Tampa Bay, *Tech. Rep. 6*, doi:10.1007/BF02798649.

Wright, C. W., E. J. Walsh, D. Vandemark, W. B. Krabill, A. W. Garcia, S. H. Houston, M. D. Powell, P. G. Black, and F. D. Marks (2001), Hurricane directional wave

spectrum spatial variation in the open ocean, *Journal of Physical Oceanography*, *31*(8 PART 2), 2472–2488, doi:10.1175/1520-0485(2001)031<2472:hdwssv>2.0.co;2.

Wu, J. (1982), Wind-stress coefficients over sea surface from breeze to hurricane, *Journal of Geophysical Research: Oceans*, *87*(C12), 9704–9706, doi:10.1029/JC087iC12p09704.

Xie, L., L. J. Pietrafesa, and K. Wu (2003), A numerical study of wave-current interaction through surface and bottom stresses: Coastal ocean response to Hurricane Fran of 1996, *Journal of Geophysical Research C: Oceans*, *108*(2), 31–1, doi:10.1029/2001jc001078.

Xie, L., H. Liu, and M. Peng (2008), The effect of wave-current interactions on the storm surge and inundation in Charleston Harbor during Hurricane Hugo 1989, *Ocean Modelling*, *20*(3), 252–269, doi:10.1016/j.ocemod.2007.10.001.

Xu, Y., et al. (2017), Observations and Modeling of Typhoon Waves in the South China Sea, *Journal of Physical Oceanography*, *47*(6), 1307–1324, doi:10.1175/JPO-D-16-0174.1.

Yamaguchi, M., J. C. Chan, I. J. Moon, K. Yoshida, and R. Mizuta (2020), Global warming changes tropical cyclone translation speed, *Nature Communications*, *11*(1), doi:10.1038/s41467-019-13902-y.

Zachry, B. C., J. L. Schroeder, A. B. Kennedy, J. J. Westerink, C. W. Letchford, and M. E. Hope (2013), A case study of nearshore drag coefficient behavior during hurricane ike (2008), *Journal of Applied Meteorology and Climatology*, *52*(9), 2139–2146, doi:10.1175/JAMC-D-12-0321.1.

Zhang, F. W., W. M. Drennan, B. K. Haus, and H. C. Graber (2009), On wind-wave-current interactions during the Shoaling Waves Experiment, *Journal of Geophysical Research: Oceans*, *114*(1), C01,018, doi:10.1029/2008JC004998.

Zhao, Z. K., C. X. Liu, Q. Li, G. F. Dai, Q. T. Song, and W. H. Lv (2015), Typhoon air-sea drag coefficient in coastal regions, *Journal of Geophysical Research: Oceans*, *120*(2), 716–727, doi:10.1002/2014JC010283.

Zheng, X., R. Mayerle, Y. Wang, and H. Zhang (2018), Study of the wind drag coefficient during the storm Xaver in the German Bight using data assimilation, *Dynamics of Atmospheres and Oceans*, *83*, 64–74, doi:10.1016/j.dynatmoce.2018.06.001.